Title
Identification, Development, and Evaluation of Small-Molecule Modulators of Nucleotide Metabolism

Author
Rosser, Ethan

Publication Date
2020

Peer reviewed|Thesis/dissertation

UNIVERSITY OF CALIFORNIA

Los Angeles

Identification, Development, and Evaluation of Small-Molecule Modulators of Nucleotide Metabolism

A dissertation submitted in partial satisfaction of the

requirements for the degree Doctor of Philosophy

in Chemistry

by

Ethan Wan Rosser

2020

ABSTRACT OF THE DISSERTATION

Identification, Development, and Evaluation of Small-Molecule Modulators of Nucleotide Metabolism

by

Ethan Wan Rosser

Doctor of Philosophy in Chemistry

University of California, Los Angeles, 2020

Professor Caius Gabriel Radu, Co-Chair

Professor Michael E. Jung, Co-Chair

This dissertation describes the identification, development, and evaluation of small-molecule modulators of nucleotide metabolism. Nucleotides, well-known for their role as the "backbone" of DNA, are essential for a variety of cell processes including energy transfer, formation of lipid membranes, and DNA and RNA synthesis. Small molecule-mediated inhibition of enzymes involved in nucleotide metabolism has shown promise in various therapeutic settings, and our group has demonstrated that inhibition of deoxycytidine kinase combined with perturbations to other nucleotide-producing enzymes can effectively treat acute lymphoblastic leukemia in mouse models.

Chapter One details the development and evaluation of inhibitors of deoxycytidine kinase. Expanding upon a scaffold previously identified by our group, structure-activity-

relationship studies were undertaken in pursuit of a clinically-viable inhibitor. With the goal of eliminating the presence of a stereocenter within our lead compound while maintaining low-nanomolar affinity for deoxycytidine kinase, a series of analogs containing a *gem*-dimethyl moiety was produced. In addition, the preclinical pharmacology of the lead compound, DI-87, was evaluated with the aid of PET imaging.

Chapter Two describes the development and application of a cell-based metabolic modifier screening platform that leverages the redundancy in pyrimidine metabolism for the discovery of selective uridine monophosphate biosynthesis modulators. In evaluating a library of protein kinase inhibitors, multiple compounds which possess nucleotide metabolism modifying activity were identified. The JNK inhibitor JNK-IN-8 was found to potently inhibit nucleoside transport and engage ENT1. Additionally, the PDK1 inhibitor OSU-03012 and the RAF inhibitor TAK-632 were shown to inhibit the therapeutically relevant enzyme DHODH, and their affinities were unambiguously confirmed through *in vitro* assays and co-crystallization with human DHODH.

The dissertation of Ethan Wan Rosser is approved.

Ellen May Sletten

Neil Kamal Garg

Caius Gabriel Radu, Committee Co-Chair

Michael E. Jung, Committee Co-Chair

University of California, Los Angeles

2020

To those who came before me

Who made my life possible

TABLE OF CONTENTS

LIST OF FIGURES

CHAPTER ONE

CHAPTER TWO

LIST OF SCHEMES

Chapter One

LIST OF TABLES

CHAPTER TWO

ACKNOWLEDGEMENTS

There have been so many people, both during and prior to my graduate research career, who have played important roles in my life and helped me to get to this point. I will not be able to thank them all, but I want to extend a heartfelt thank you to those who have supported me, mentored me, pushed me, and helped mold me into the person I am today – I would not be here without you.

I first would like to thank my wife and partner, Yvette. It really doesn't seem like that long ago that we hopped off the plane at LAX, fresh from our honeymoon, and embarked upon our parallel UCLA journeys of graduate school and a pediatrics residency. She has been in my corner for many fights and been there for me through many turbulent times. Graduate school was difficult, and I placed a lot of pressure on myself. She helped to ease that pressure, ground me, pull me out of bad mindsets and remind me that it was okay to relax and enjoy life outside of the lab. She has been my biggest advocate and supporter, celebrating my successes and encouraging me through my failures. She continues to expand my world, and I am eternally grateful for her love, her support, and her patience.

I would also like to thank the members of my Dissertation Committee – Prof. Neil Garg, Prof. Ellen Sletten, Prof. Michael Jung, and Prof. Caius Radu. I have learned from each of them, and they have always been available and very willing to help with a variety of matters. Their guidance has been instrumental to my graduate education, and I see each of them as leaders for the department as well as for generations of scientists. I particularly thank my two Principal Investigators – Professors Caius Radu and Mike Jung. When I first started graduate school, I was a bit unsure of what I wanted to achieve and where. An opportunity arose for me to work

between two labs in two departments, doing organic synthesis as well as cell/molecular/cancer biology. Caius and Mike each sat down with me individually, and ultimately they gave me a chance to become part of their respective teams. Throughout the course of my graduate career they gave me freedom, responsibility, trust, and mentorship. Each are brilliant and dedicated scientists who are truly incredible to work with and observe. Caius never ceases to impress me with his ability to draw connections between seemingly unrelated findings. He is a voracious reader of the scientific literature and maintains a level of discipline and commitment to his craft that is unparalleled. I always appreciated and will miss the wisdom which he would often dole out during research meetings. One of my favorite quotes was "we don't want to just be observers; we want to be explainers, too." This is such a fundamental tenet of science, yet it can be easily lost in the pages of experiments and piles of data. The ability to observe, process, understand, and ultimately explain is the ultimate demonstration of scientific and intellectual prowess, and this was something Caius pushed us all to achieve. I am grateful for his mentorship, and thankful that I was able to work with such a dedicated scientist. These same observations and sentiments are just as applicable to Mike (AKA The Boss). Again, I am endlessly amazed at his recall for details and findings, scientific or otherwise. His complete mastery of the field of chemistry is astounding and inspiring, and I truly believe there are exceedingly few academics and scientists like him. He is very patient, which is quite amazing given the sheer number of projects and commitments he has. Though he has been in the game for a few years, he remains an ardent student of the field, and maintains the energy of a junior professor. Beyond his merits as a mentor and scholar, he has also changed the lives of countless people and families through his work developing two FDA-approved drugs for the treatment of prostate cancer. His academic

and business successes combine with his charisma to create a truly unique learning and research environment. I am thankful to have trained with and learned from him.

While I am truly lucky to have been mentored by Caius and Mike, I would have never had the opportunity were it not for my family. My parents raised me to believe that I could accomplish whatever I wanted to, and while they never pushed me towards a certain career, they did always push me upwards. Only one time did my father dissuade me from pursuing a career, and that was when I declared that I wanted to become a furniture mover when I grew up. My dad has always been supportive, trusting my choices and observing rather than directing. I think that's what came naturally to him, but maybe he subconsciously realized that I had learned so much from him that I would be just fine on my own. He is a very dedicated individual, as evidenced by his six decades of near-daily piano playing, but he does not boast or brag about it – he does it because he loves it. I know that his dedication to reading to myself and my siblings every night when we were young led to my passion for reading and, ultimately, my curiosity and desire to discover. These played fundamental roles in my desire to pursue a PhD. He is compassionate, eager to learn, and usually has a smile of some sort on his face; I hope to continue growing to become like him. My mother, mama, is similarly quick to smile. She has always ferociously loved me and wanted me to succeed, though when I was young this could lead to arguments and tears. Her standards were high because she wanted me to have every opportunity; she herself had emigrated from Taiwan, making me a first-generation American on her side, and she knew the doors that could be unlocked through hard work and dedication. My mom is incredibly kind, thoughtful, and generous. She is a helper and a carer. She always thinks of others before herself and supports fully – I will always remember the sound of her voice cutting through the rest of the crowd during my basketball games. I had my stumbles but I tried

my best to embody the qualities which she has demonstrated day in and day out. Her love and dedication to our family have truly made me a “mama’s boy”.

I am incredibly lucky to have such supporting, loving, and caring parents. However, it wasn’t just me being raised by them – my younger sister Micaela and younger brother Aaron have been along for the ride as well. My siblings never cease to amaze me, and they serve as a source of constant pride. My sister’s academic achievements are overshadowed only by how great of a person she is; generous, cultured, kind, and adventurous. She is a force to be reckoned with, and is a strong female voice in a discipline typically dominated by men (surgery). I have loved how our relationship has developed as we’ve grown up together. Aaron, ten years my junior, has made me so proud by becoming his own person instead of ascribing to what others thought he should be or do based upon his brother/siblings. “Others” includes me – I thought he would grow up to be similar to me, and pressured him to do as much. But as he learned what he did and didn’t like and made his own decisions, I learned to let him be and provide guidance from a couple steps back. We grew together this way, and it has been amazing to watch him during this process. His academic prowess seems effortless – this kid is smart – and his sense of self, motivation, and direction demonstrates maturity far beyond his years. I am excited to see what he puts his mind to next, and can’t wait to continue to grow with him.

Beyond my incredible nuclear family, I was blessed with great grandparents. My maternal grandfather grew up in a different kind of world. As an orphan in China, he appears to have lied about his age in order to fight as an American Ally in World War II. He would later go on to fight against the Chinese Communist Party before relocating to Taiwan. He and my maternal grandmother sacrificed much to raise five children, and would go on to watch all five make it to the United States and become United States citizens. Both would follow suit, moving

to the US and gaining citizenship when I was young. They were such steady rocks and sources of motivation and support for my mom and her siblings, and by extension to me and their other grandchildren and great-grandchildren. I love my grandmother's big smile, the way she always tells me to eat more, and her strong will and decisive nature. She has always had a vision for her family and has ensured that it came to fruition. I am thankful that she is able to share this moment with me, and hope to honor my grandfather's legacy with this achievement. I also hope to honor the legacies of my paternal grandparents. My dad's father was a veteran and an academic, receiving his PhD in Political Science and holding both teaching and administrative positions in a long and successful career. He passed away due to complications from prostate cancer when I was in high school, and while I wish he were here today, he has remained influential upon my life. He was an outdoorsman, a supporter of the arts, and a great father. He was also a serious man, but was quick to teach and had a wry smile that always seemed mischievous to me. His seriousness was balanced by my grandma's soft and caring nature, which belied her incredible intelligence and talent. She was a lifelong artist, with watercolor being her medium of choice, and was offered a Fulbright Scholarship to study art in Europe after graduating from Ohio Wesleyan University. She declined the offer in favor of marrying my grandfather and starting a family, paving the way for me to be in the position I am in today. She was gentle and kind, and supported me in my education both emotionally and financially. I will always cherish the letters she wrote me when I was an undergraduate. At the end of her life, when it was just the two of us in her room, I thanked her for her support and promised her that I would pursue and complete a PhD. She passed away a few moments later. I have thought of her often during my graduate career, in good times and in difficult times – her memory has helped me keep my promise.

While I have lost some family members over the years, I have also gained others. My in-laws, Robert and Melvie Strampe, have welcomed me into their family since the day I met them. Their love, support, and encouragement through the years, particularly during graduate school, has been so appreciated and comforting. They have joined forces with my parents to form the ultimate supportive unit, and I am so thankful to have them in my life. My brother-in-law Miles and his wife Kyhra have been similarly generous and accepting. Their welcoming natures, willingness to share insight, and their support means so much to me, as does their daughter Murray, whom I cannot wait to watch grow from a closer vantage point.

Beyond the bonds of blood and paper, I have been lucky to have an incredible group of mentors and friends surrounding me for as long as I can remember.

One of the most influential people in my life has been Eric Davis, my high school basketball coach. He instilled within me the confidence and knowledge that I could do whatever it was that I put my mind to. He taught me how to endure and how to persevere. He developed my sense of dedication and drive, demanded accountability both on and off the court, and fostered lifelong bonds between myself, him, and my teammates. He taught me about life through the medium of basketball, and I am forever grateful to him.

As an undergraduate, I started out majoring in biology and was in the pre-med track. I took the dreaded Introduction to Organic Chemistry course at the beginning of my second year and got destroyed by it – I had to drop the class and try again. The following semester's class was taught by Prof. Ming Xian, and the way he taught helped make something click in my head. I began to understand the material, and eventually I fell in love with the course. I changed my major to chemistry at the end of that semester and Prof. Xian let me join his research group as an undergraduate researcher. In his group I was mentored by two great postdoctoral scholars –

Nelmi O. Devarie and Wei Chen. Nelmi was very patient with me, taught me the ropes and demonstrated the importance of spending time both in the lab as well as reading the literature. He was the first person to put the idea of pursuing a PhD in my head. After Nelmi left, Wei stepped in and took me under his wing. He supported me so much, further refined my lab techniques and generously shared his time and projects with me. Prof Xian, Nelmi and Wei each paved the way for me to have success in the lab and beyond, helping me earn my place as an author in published research articles and encouraging me to apply for awards and grants. I would not have made it to UCLA, would not have been awarded an NSF fellowship, may not have earned a PhD if it weren't for them. I am very thankful for their support and mentorship.

My friends and their families have always been a source of stability, laughter, support, camaraderie, and love in my life. I cannot remember a time when Kevin Hinckle, my first brother, was not in my life. We grew up playing basketball together, and he along with his parents Kirk and Wendy are like another family to me. I am fortunate enough to have kept a tight-knit group of friends for the vast majority of my life. My pre-school classmates Michael Lasik, Gannon Maggard and Jeremy Rossow are still three of my closest friends. Included in that circle are Kyle Norton, Matt Pfeifer, Matt Gray, Mike Gray, Kevin Thompson, and Taylor Roberts. Some of my best memories and formative moments have been with these guys – they have always had my back and supported me – and I am looking forward to building upon those memories for the rest of our lives. While these men have been with me since childhood, I have also been lucky to grow my circle. Nadia Weiner has always been such a great confidante and caring person; I hope she moves back to the US soon! I am thankful to have grown closer with Derek Campbell, whose sincerity and intellect is great to be around. I have treasured my friendship with Ryan and Tiara Thomas – two incredible people with such good hearts. I am

looking forward to spending more time with them as well as with their daughters (my god-daughters) Emberly and Harper. Jacob Casey has been an incredible source of laughter, support, and friendship throughout the years, and as have Jared Meyer and Reyna Swift – they are each incredibly appreciated.

In Los Angeles I was fortunate to be surrounded by many wonderful friends and labmates. There were so many great times and travels with Taryn Kilmer – I hope those continue for years to come. Rob Gross and Lisa Jacobs have been such great and steady friends; I love how comfortable we all are together, and I look forward to watching their daughter Reagan grow. My brother Dalton Steele has been a great friend, supporting and encouraging me while we both have gone through our ups and downs. I am lucky to count him as a lifelong friend and look forward to what the future holds for him and for our friendship. Mike Corsello was my guide when I came to UCLA for my recruiting visit, and we instantly got along. I miss our in-depth talks about life and happiness, and hope to have more of them soon. Gary Duckwiler and Karen Hirsch have quickly become great friends – I appreciate so much their open and earnest talks about anything and everything. They have befriended, supported, and mentored me, and I look forward to returning the favor as much as I can. I have also really enjoyed getting to know Paul and Lindsay Graves, and am excited to join them for future Derby Parties.

My office and lab-space in MSB 3211 has been filled with great friends and labmates. Youngsug Kim is missed now that he is back home in South Korea, but I am thankful to have had such an encouraging and kind person next to me. Johnny Pham was the first post-doc I worked by in Mike's lab, and I loved our easy conversations on whole hosts of topics. Gaoyuan Ma and the husband and wife team of Xiaoguang Liu and Xiaohong Chen have been great officemates and friends – they have been incredibly kind and supportive of me, and they have

contributed to making our room a great environment to research in. I have worked with many post-docs in the Jung Group and have gotten along well with them all – they are a special group with more promising projects and drug candidates than typical groups have in a career. I'm also thankful for the friendship and mentorship of Daniel Sun – he always has time to help no matter what the problem is, and has helped me through a great deal of synthetic and methodological problems in the past four years. My labmate Roy Pan has been a great friend, supportive and always there to help and talk.

On the A-Level I have been fortunate to work with a great group of scientists who were generous with their time and scientific prowess. Evan Abt, Soumya Poddar, Woosuk Kim, Joe Capri and Thuc Le all helped teach me so much, and were instrumental in all aspects of my research – I am thankful to have worked with such great scientists and kind people who helped make our research translational and impactful. I am also thankful to have been able to work with and learn from Christine Mona, a balancing presence who was always there to talk, provide guidance, and motivate. Her humor, wit, thoughtfulness and talent are very appreciated. Nagichettiar "Saty" Satyamurthy has been such a helpful and generous A-level member and mentor as well – his knowledge and recall is vast, and his practical experience has helped me out of many synthetic jams over the years. I am very thankful to have had him as part of my research and mentorship team.

My 2015 cohort was, I believe, particularly special. We had a great mix of personalities and everyone got along well, making the hellish first year much more bearable. The cohort has had a lot of academic and scientific success, and I am looking forward to tracking everyone's careers as they go forward. I am particularly thankful to have gotten to know Priera Panescu, with whom I worked closely with while we served as board members of the Organization for

Cultural Diversity in Science. She is a highly driven, smart, and passionate woman who strives and pushes for real change.

Finally, I would like to thank my educational institutions – Washington State University and the University of California, Los Angeles. WSU gave me every opportunity I could have asked for, gave me time to grow and come into my own, and set me up for success in both graduate school as well as in life. Without my time in Pullman, I would not have found my way to LA. Go Cougs! UCLA and the Department of Chemistry and Biochemistry have given me a lot of support and tutelage, and have provided many opportunities for growth outside of the lab, which I really appreciate. Having the opportunity to be a member of the Organization for Cultural Diversity in Science was a highlight of my graduate career, and it has been very affirming to have the support of the Division of Physical Sciences. Working closely with the Dean, Miguel Garcia-Garibay, towards providing more abundant and equitable opportunities for historically marginalized communities has been rewarding and motivating. I believe there is real opportunity for decisive change in this moment, and am grateful to have had the opportunity to play a part.

Pursuing a PhD in Organic Chemistry is a life-changing endeavor. I am still processing this journey that I have been on, but in the end I am thankful to have had the opportunity, the chance, to make a difference. I would not have made it without the support of those named in the above text, and without the support of so many more who I have not been able to include. Thank you all.

VITA

Education

University of California, Los Angeles, Los Angeles, CA
Master of Science in Chemistry — June 2017

Washington State University, Pullman, WA
Bachelor of Science in Chemistry, *cum laude* — May 2014

Research and Teaching Experience

Graduate Research Assistant — September 2015 – June 2020
University of California, Los Angeles, CA
Advisor: Prof. Caius G. Radu (Department of Molecular and Medical Pharmacology)
Co-Advisor: Prof. Michael E. Jung (Department of Chemistry and Biochemistry)
- Identified and synthesized small molecule modulators of nucleotide metabolism while profiling their effects upon cancer cells and elucidating novel anticancer therapeutic strategies

Graduate Teaching Assistant — September 2015 – June 2017
University of California, Los Angeles, CA
- Instructed undergraduate students in both lecture and laboratory settings, teaching fundamental principles of general chemistry, organic chemistry, and laboratory techniques

Undergraduate Research Assistant — January 2011 – May 2014
Washington State University, Pullman, WA
Advisor: Prof. Ming Xian (Department of Chemistry)
- Synthesized and developed small molecule fluorescent probes for the detection of hydrogen sulfide and hydrogen polysulfides in biological systems

Leadership and Service

Organization for Cultural Diversity in Science (OCDS) at UCLA
Co-President — February 2019 – March 2020
Outreach Coordinator — October 2016 – January 2019

Fellowships and Awards

NSF Graduate Research Fellowship — 2017 – 2020
NASA Space Grant Scholarship — 2012, 2014
Undergraduate Award in Organic Chemistry – American Chemical Society — 2014
J. Culbertson Chemistry Scholarship — 2013, 2014
Edwin J. Hart Chemistry Scholarship — 2013
Art and Helen Brunstad Chemistry Scholarship — 2012, 2013
Washington State University Undergraduate Research Mini-Grant — 2011

Publications

1. *Isoquinoline thiosemicarbazone displays potent anticancer activity with in vivo efficacy against aggressive leukemias*
   Daniel L. Sun*, Soumya Poddar*, Roy D. Pan, Ethan W. Rosser, Evan R. Abt, Juno Van Valkenburgh, Thuc M. Le, Vincent Lok, Selena P. Hernandez, Janet Song, Joanna Li, Aneta Turlik, Xiaohong Chen, Chi-An Cheng, Wei Chen, Christine E. Mona, Andreea D. Stuparu, Laurent Vergnes, Karen Reue, Robert Damoiseaux, Jeffrey I. Zink, Johannes Czernin, Timothy R. Donahue, Kendall N. Houk, Michael E. Jung, Caius G. Radu. *RSC Medicinal Chemistry*. **2020**, In Press. (*These authors contributed equally).

2. *Development and preclinical pharmacology of a novel dCK inhibitor, DI-87*
   Soumya Poddar, Edmund Capparelli, Ethan W. Rosser, Liu Wei, Thuc Le, Michael E. Jung, Caius G. Radu, Mina Nikanjam. *Biochem. Pharmacol*. **2019**, 172, Article No. 113742.

3. *Metabolic modifier screen reveals secondary targets of protein kinase inhibitors within nucleotide metabolism*
   Evan R. Abt*, Ethan W. Rosser*, Matthew A. Durst*, Soumya Poddar, Vincent Lok, Liu Wei, Woosuk Kim, Janet Song, Joseph R. Capri, Thuc M. Le, Roger Slavik, Michael E. Jung, Robert Damoiseaux, Johannes Czernin, Timothy R. Donahue, Arnon Lavie, Caius G. Radu. *Cell Chem Biol*. **2019**, 27(2), 197-205. (*These authors contributed equally).

4. *The Development of Fluorescent Probes for Visualizing Intracellular Hydrogen Polysulfides*
   Chen, W.; Rosser, E. W.; Matsunaga, T.; Pacheco, A.; Akaike, T.; Xian, M. *Angew. Chem. Int. Ed*., **2015**, 54, 13961-13965.

5. *A Specific Nucelophilic Ring-Opening Reaction of Aziridines as a Unique Platform for the Construction of Hydrogen Polysulfides Sensors*
   Chen, W.; Rosser, E. W.; Zhang, D.; Shi, W.; Li, Y.; Dong, J.; Ma, H.; Hu, D.; Xian, M. *Org. Lett*., **2015**, 17(11), 2776-2779.

6. *Fluorescent Probes Based on Nucleophilic Substitution Cyclization for Hydrogen Sulfide Detection and Bioimaging*
   Peng, B.; Chen, W.; Liu, C.; Rosser, E. W.; Pacheco, A.; Zhao, Y.; Aguilar, H. C.; Xian, M. *Chem. Eur. J*., **2013**, 20(4), 1010-1016.

Patents

1. *Modulators of pyrimidine nucleotide biosynthetic pathways*
   Evan R. Abt, Ethan W. Rosser, Matthew A. Durst, Soumya Poddar, Arnon Lavie, Caius G. Radu. U.S. Provisional Patent Ser. No. 62848728, **2019**.

CHAPTER ONE

Preclinical Pharmacological Evaluation and Further Development of Small Molecule Inhibitors of Deoxycytidine Kinase

1.1 Introduction

With critical roles in fundamental biological processes ranging from DNA and RNA synthesis to energy transfer to lipid synthesis, the importance of nucleotides cannot be overstated.[1,2] Given their essential character, levels of purine and pyrimidine nucleotides are highly regulated within mammalian systems, and their production is achieved through parallel and convergent biosynthetic pathways.[3,4] The *de novo* pathway (DNP) produces nucleotides starting from glucose and simple amino acid precursors, while the nucleoside salvage pathway (NSP) recovers preformed nucleosides from the extracellular environment and phosphorylates them to generate their monophosphate nucleotide forms.[4,5] The action of the key enzyme ribonucleotide reductase (RNR) converts ribonucleotides (rNs), necessary for essential processes such as RNA synthesis and energy transfer, to their deoxyribonucleotide (dN) forms through reduction of the ribose 2'-hydroxyl group, thus generating the dN building blocks required for DNA synthesis and repair.[6] The salvage pathway for dN synthesis relies upon the action of two cytosolic kinases, thymidine kinase 1 (TK1) and deoxycytidine kinase (dCK), to phosphorylate deoxyribonucleosides recovered from the extracellular space to their monophosphate forms, which are subsequently phosphorylated by other kinases to produce deoxyribonucleotide triphosphates (dNTPs).[7] Each kinase possesses unique substrate specificities; TK1 phosphorylates thymidine (dT) and deoxyuridine (dU), while dCK phosphorylates deoxycytidine

(dC), deoxyadenosine (dA), and deoxyguanosine (dG).[8] Though dCK has specificity for three out of the four dN precursors of nucleic acids, it is able to indirectly produce the fourth (deoxythymidine triphosphate, dTTP) by the action of dCMP aminase and thymidylate synthase upon the dCK product dCMP, thus generating dTMP.

dCK is a homodimer with monomeric units composed of ten α-helices surrounding a five-stranded parallel β-sheet.[9] The protein is able to adopt several distinct conformations to accommodate varied nucleoside phosphoryl acceptors (dC, dA, dG) as well as both ATP and UTP phosphoryl donors.[10,11] dCK is constitutively expressed, though expression levels are dependent upon tissue type – lymphocytic tissues have high expression, whereas proliferating cells such as those of the colon mucosa have intermediate expression, and differentiated tissues such as muscle have low expression.[7] It has been demonstrated that dCK activity is modulated by reversible phosphorylation of Ser74, a residue in a flexible linker region between two of the ten α-helices of the monomeric unit.[9]

The clinical utility of dCK activity is well-established, as it is the key activator of multiple nucleoside analog prodrugs used in antiviral and anticancer therapies.[12] Prodrugs such as gemcitabine are activated through dCK-mediated phosphorylation to yield their monophosphate forms, which are subsequently phosphorylated to their triphosphate forms by downstream kinases before incorporation into viral or cancer cell DNA. This incorporation leads to DNA damage, stalled replication forks, S-phase arrest, and can eventually lead to apoptosis.[13] Cancer, viral, and other rapidly-proliferating cells are disproportionately affected by this therapeutic modality, as their increased rates of replication lead them to greater levels of

nucleotide-analog incorporation. The role of dCK in promoting apoptosis in cancerous cells, albeit indirect, serves as a preview for potential therapeutic applications of dCK inhibition – when confronted with high levels of DNA damage and replication stress, cancer cells undergo apoptosis. DNA damage can result from loss of genomic integrity through incorporation of nucleotide analogs into newly synthesized DNA (i.e., gemcitabine therapy), or can result from an imbalance in cellular dNTP pools.[13,14] The latter has been explored as a potential anticancer therapy through inhibition of the key NSP enzyme RNR, which as been an important target in anticancer therapy for decades. However, the use of RNR-inhibiting agents, such as hydroxyurea and triapine (3-AP), has so far proven unsuccessful in clinical trials, potentially due to the existence of the NSP which becomes upregulated upon DNP-inhibition and thus allows cells to maintain control over dNTP levels.[13,15–17] An appealing response to this compensatory mechanism is to destabilize pool levels through simultaneous inhibition of both the NSP and DNP, therefore inducing replication stress response and apoptosis.

dCK is an intriguing target in anticancer therapy as it is a rate limiting enzyme within the salvage pathway of dNTP biosynthesis, and multiple cell lines and tumor samples in the Cancer Cell Line Encyclopedia and The Cancer Genome Atlas, respectively, express this enzyme at higher levels when compared to normal tissue.[18] Among the cancers listed in these resources as having high expression levels of dCK, leukemias and lymphomas are most prominently featured. However, despite its ability to provide all four dNs necessary for DNA synthesis and repair, the potential clinical implications of inhibiting dCK activity have only recently become clear. In previous studies, dCK has been shown to play important roles in hematopoiesis through regulation of dNTP biosynthesis in lymphoid and erythroid progenitors – hematopoiesis was

impaired in dCK$^{-/-}$ mice due to lack of dCTP, which resulted in replication stress, S-phase arrest, and DNA damage in these progenitors.[8,19] dCK has also been demonstrated to activate the G2/M checkpoint in cells responding to DNA damage.[20] Given its roles in hematopoiesis and in regulation of cell division, as well as the potential for disruption in dNTP pool levels following its inhibition, our group became interested in developing small molecule inhibitors of dCK for use in novel anticancer therapies.

Following a high-throughput screening campaign in our lab, two hit compounds were identified as low-μM inhibitors of dCK (**Figure 1.1A**), and their activity was validated through inhibition of uptake of tritiated deoxycytidine (^{3}H-dC).[21] Subsequent structure-activity relationship (SAR) studies, aided by crystallographic data of early inhibitors complexed with dCK, revealed that alkyl substitution of the thiazole 5-position led to increased dCK affinity. This knowledge eventually yielded the initial lead compounds DI-38 and DI-39, which had low-nM IC_{50} values in CEM cells (**Figure 1.1B**). The translational potential of this class of compounds was demonstrated by Nathanson et al., who showed that inhibition of the DNP through dT-mediated allosteric regulation of RNR led to upregulation of the NSP in order to avoid lethal replication stress.[17] Inhibiting the NSP-mediated production of dNs using DI-39 while simultaneously blocking the DNP with dT proved to be an efficacious therapy against acute lymphoblastic leukemia (ALL) models in mice, and no host toxicity was detected. The proposed mechanism involves the activation of cellular replication stress response upon insufficient levels of dCTP/dNs for proper DNA synthesis. This lack of dNs leads to S-phase arrest (stalled DNA-replication), DNA damage, and apoptosis.

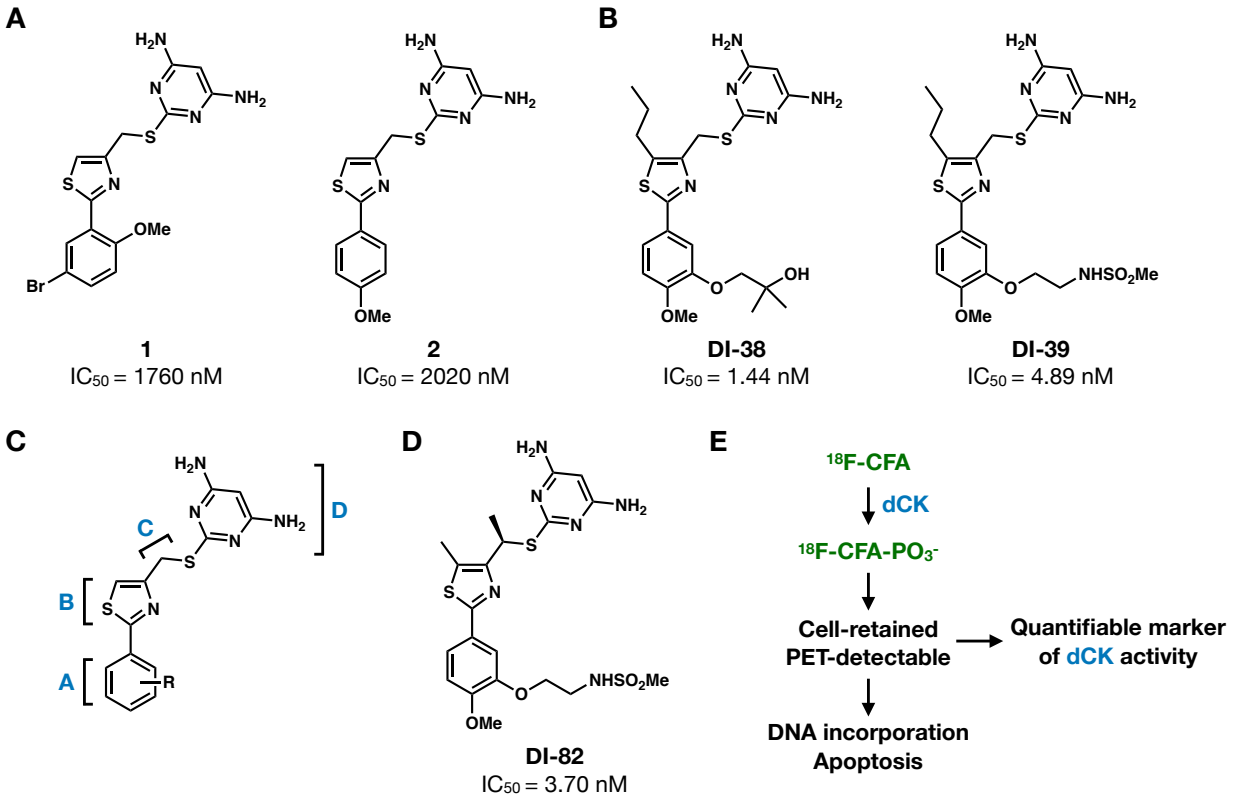

Figure 1.1 | Discovery and development of small molecule inhibitors of deoxycytidine kinase. (A) Structures for initial hit compounds identified by high throughput screen and IC_{50} values determined using a ^{3}H-dC uptake assay in L1210 cells. (B) Former lead compound dCK inhibitors and IC_{50} values determined using ^{3}H-dC uptake assay in CCRF-CEM human cells. (C) Distinct regions of dCK inhibitor molecular scaffold. (D) Former lead compound dCK inhibitor and IC_{50} value determined using ^{3}H-dC uptake assay in CCRF-CEM human cells. (E) Schematic of dCK role in activation of ^{18}F-CFA PET probe.

Despite the *in vivo* efficacy of DI-39 against models of ALL, it remained a sub-par clinical candidate as it suffered from metabolic instability and was highly insoluble. In assessing the structure and potential areas suitable for modification, the scaffold can be divided into four

distinct sections: a substituted phenyl ring represents Part A, which is connected to the 2-position of the Part B thiazole ring, which in turn is bound at the 4-position to a Part C linker region which connects the thiazole to a Part D pyrimidine ring (**Figure 1.1C**). The 2-mercapto-4,6-diaminopyrimidine Part D of the initial lead compounds was found to be optimal for interaction with dCK by Nomme et al., while the 5-propyl moiety of the Part B thiazole was discovered to present a metabolic liability.[22] It was previously shown that increasing the alkyl chain length at the 5-position of the thiazole led to increased dCK affinity,[21] but with metabolic considerations in mind, a 5-methyl substituent was adopted as the appropriate substitution, despite its lower dCK affinity. To compensate for this loss of activity, modification of the Part C linker region was explored, ultimately leading to the discovery that a methyl substituent, specifically the *R*-enantiomer, led to increased *in vitro* activity and metabolic stability. Subsequent exploration of substitutions of the Part A phenyl ring led to identification of a new lead compound, DI-82, which had low-nM affinity for dCK and promising metabolic stability (**Figure 1.1D**).

While potent activity against the desired target is an important characteristic for small molecule therapeutics, it can mean nothing if the pharmacokinetic (PK) and pharmacodynamic (PD) properties of the lead compound are poor. Positron emission tomography (PET) is a widely-used non-invasive imaging technique which has applications within diagnosis, staging, and therapeutic monitoring in cancer.[23,24] Recently, PET imaging has emerged as a promising tool for use in drug discovery and development, specifically for PK/PD evaluation.[25] In PET imaging, a positron-emitting isotope is incorporated into a molecule, and this so-called PET probe is then injected into the test subject. As the isotope within the PET probe decays, the emitted positrons collide with electrons, thus initiating an annihilation event and releasing two gamma rays.[23]

Using a PET scanner, clinicians and researchers are able to detect the gamma rays and track the distribution and concentration of the PET probe throughout the body. The first PET probe was [^{18}F]-fluoro-2-deoxy-D-glucose (^{18}F-FDG; FDG), a powerful imaging molecule by virtue of the Warburg effect in which cancer cells preferentially utilize aerobic glycolysis to meet their energy demands.[26] FDG is recognized by the glucose transporters GLUT1 and GLUT3, which transport the glucose analog into the cell where it is phosphorylated to FDG-6-phosphate by hexokinase.[24] No longer a substrate for glycolysis and unable to escape the cell, the FDG PET probe accumulates in all tissues but especially in cancer cells due to their increased levels of glycolysis, allowing for cancer imaging through PET scanning.[23]

In the context of drug discovery, PET imaging may be used to evaluate the PK and PD of lead compounds through incorporation of a positron-emitting isotope into the lead compound, so long as isotope addition does not significantly alter the biological properties of the molecule. Following injection, PET imaging allows for visualization and quantification of target engagement, and when viewed as a function of time, provides invaluable information regarding clearance, metabolism, and kinetics.[23] Early use of PET imaging in evaluating lead compounds can inform decision-making, accelerate the advancement of promising candidates, and reduce failure rates.[25,27] PET tracers have been developed for many biological targets and processes, including for dCK activity.[28–30] The recently reported dCK PET probe [^{18}F]Clofarabine ([^{18}F]CFA; CFA) is a purine analog which is phosphorylated by dCK to form cell-retained CFA monophosphate, thereby generating a PET-detectable signal in dCK-expressing tissues (**Figure 1.1E**). Such tracers can help determine dose-response relationships by directly interrogating the

target pathway being altered by the drug. Because of the importance of dCK to the nucleoside salvage pathway of healthy tissues, it is necessary to characterize dose-response relationships for dCK inhibition to determine the optimal inhibition necessary for maximal tumor growth suppression without leading to excess toxicity.

In Section One of Chapter One, the development of lead dCK inhibitor DI-87 is described, along with its subsequent preclinical pharmacological evaluation. These studies utilize PET imaging to measure dCK inhibition, and PK-PD modeling to quantify dose-response relationship between drug levels and tumor growth inhibition. In Section Two, the further development of small molecule inhibitors of dCK is detailed, with attempts at producing achiral low-nM dCK inhibitors detailed. In Section Three, the evaluation of dCKi as nucleoside-mimetics, or "nucleomimetics", is detailed.

Section One: Development and Preclinical Pharmacological Evaluation DI-87, a Novel Inhibitor of Deoxycytidine Kinase

Adapted from: Soumya Poddar, Edmund Capparelli, Ethan W. Rosser, Liu Wei, Thuc Le, Michael E. Jung, Caius G. Radu, Mina Nikanjam. *Biochem. Pharmacol.* **2019**, 172, Article No. 113742.

1.1.1 Development, Synthesis, and *In* Vitro Activity of DI-87 – a Potent Inhibitor of Deoxycytidine Kinase

We previously reported the development of DI-39[17] and DI-82[22], which were potent inhibitors of dCK but possessed poor solubility and sub-optimal drug-like properties. In an effort to address the shortcomings of these compounds, we analyzed the crystal structures of human dCK complexed with our lead compounds which revealed that the sulfonamide moiety of DI-82 formed hydrogen bonds within the substrate binding pocket. In order to maintain these interactions while potentially improving solubility, we sought to replace the sulfonamide moiety of DI-82 with a morpholine ring. Morpholines are a privileged scaffold in medicinal chemistry, with documented benefits such as improved pharmacokinetic and metabolic profiles for molecules bearing this heterocycle.[31] Additionally, previous SAR studies upon the dCK inhibitor (dCKi) scaffold indicated that modifications within this region were well tolerated.[21,22] DI-87 was synthesized as follows: an S_N2 reaction between 4-methoxy-3-hydroxybenzonitrile and 4-(2-chloroethyl)morpholine furnished **3** (**Scheme 1.1**). Heating with an aqueous solution of ammonium sulfide gave thioamide **4**, which was subjected to Hantzsch thioazole formation conditions to yield thiazole **5**. Asymmetric Corey-Bakshi-Shibata (CBS) reduction of the ketone

resulted in the *S*-alcohol **6**, which was converted into the trifluoroacetate **7** and directly displaced *via* S_N2 reaction by 4,6-diamino-2-mercaptopyrimidine to furnish (*R*)-DI-87 (DI-87) (**8**). The trifluoroacetate **7** was not isolated due to instability of this intermediate.

Scheme 1.1 | Synthesis of DI-87[a]

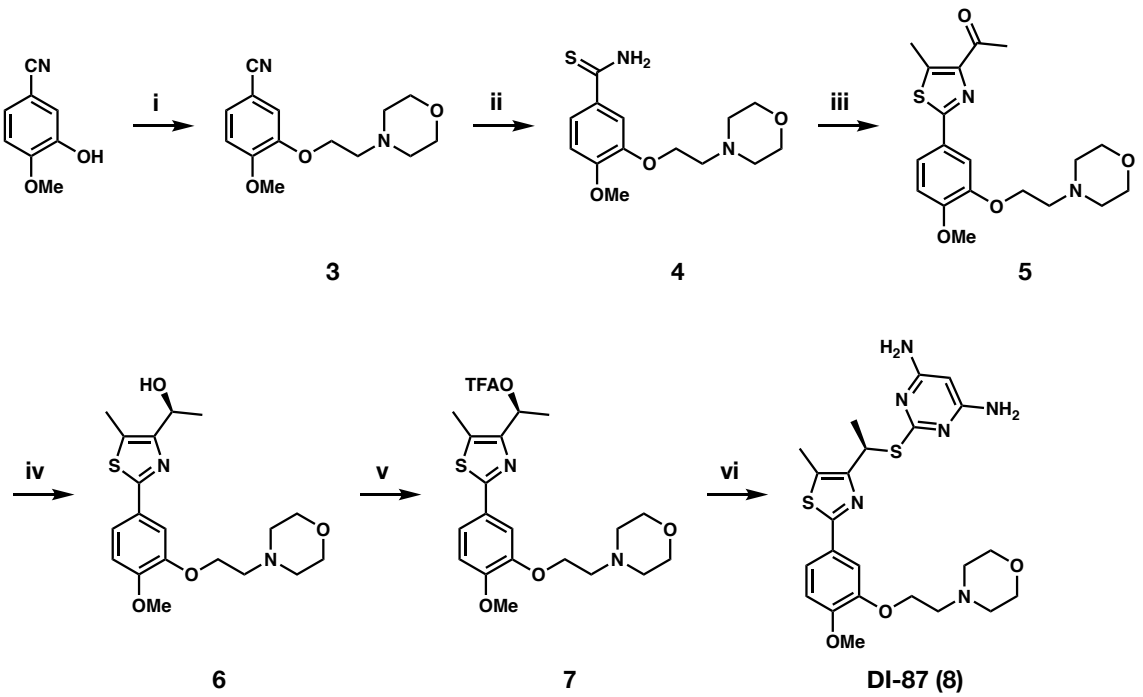

[a]Reagents and conditions: (i) 4-(2-chloroethyl)morpholine hydrochloride, Cs_2CO_3, Acetone:DMF 1:1, 70 °C, 12 hr, 91%; (ii) $(NH_4)_2S$ (20% aqueous solution), pyridine, Et_3N, 60 °C, 12 hr, 79%; (iii) 4-bromo-2,3-pentanedione, ethanol, reflux, 4 hr, 54%; (iv) (*R*)-(+)-2-methyl-CBS-oxazaborolidine, Borane-THF complex, THF, -78 °C, 6 hr, 40%; (v) Trifluoroacetic anhydride, DCM, 0 °C, 0.5 hr; (vi) 4,6-diamino-2-mercaptopyrimidine, Cs_2CO_3, DMF, 80 °C, 3 hr, 27% (2 steps).

The IC_{50} values for each enantiomer of DI-87 were determined using a dC uptake assay in CEM cells. (*S*)-DI-87 exhibited a much higher IC_{50} value (468 ± 2.1 nM) relative to (*R*)-DI-87

(3.15 ± 1.2 nM), consistent with previous studies which showed that the *R*-enantiomer was the active species (**Figure 1.2A**). (*R*)-DI-87 treatment rescued CEM cells from the anti-proliferative effects of gemcitabine, a dCK-dependent nucleoside analog prodrug used in anticancer therapy, with an EC_{50} of 10.2 nM **(Figure 1.2B**). Additionally, we observed that protein binding of (*R*)-DI-87 (DI-87) is comparatively lower than its predecessor, (*R*)-DI-82 (DI-82), as measured by IC_{50} of the respective dCK inhibitor in presence of bovine serum albumin (BSA) (**Figure 1.2C**).

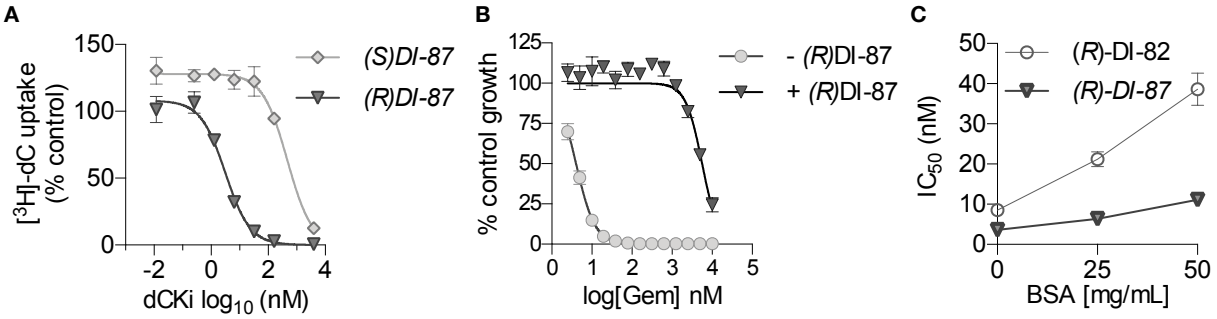

Figure 1.2 | DI-87 exhibits potent inhibition of deoxycytidine kinase. (A) Ability of enantiomeric dCK inhibitors (dCKi) (*S*)-DI-87 and (*R*)-DI-87 to inhibit uptake of [^{3}H]-dC in CEM T-ALL cells. (B) Dose response of (*R*)-DI-87 in CEM T-ALL cells treated with 10 nM gemcitabine (Gem). (C) Protein binding of (*R*)-DI-87 and (*R*)-DI-82 assessed by comparing IC_{50} values of the compounds in presence of 25 and 50 mg/ml bovine serum albumin (BSA).

1.1.2 Pharmacokinetics of DI-87

DI-87 concentrations in plasma and tumor were determined for three dose levels: 10, 25, and 50 mg/kg, and were obtained at a single time point from each mouse. Plasma DI-87 concentrations peaked between 1 and 3 hr (**Figure 1.3A**). Tumor concentrations were lower than plasma by more than 3.5 fold and had a later, more sustained peak at 3–9 hr (**Figure 1.3B**).

A

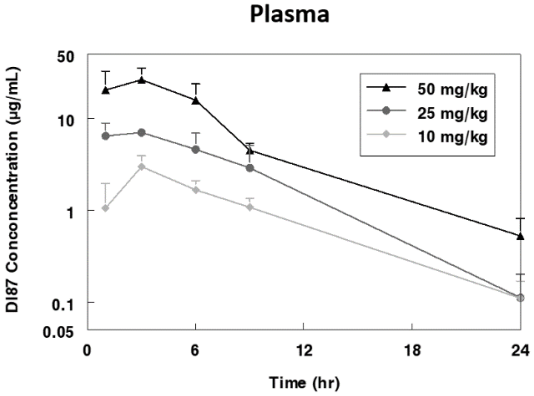

B

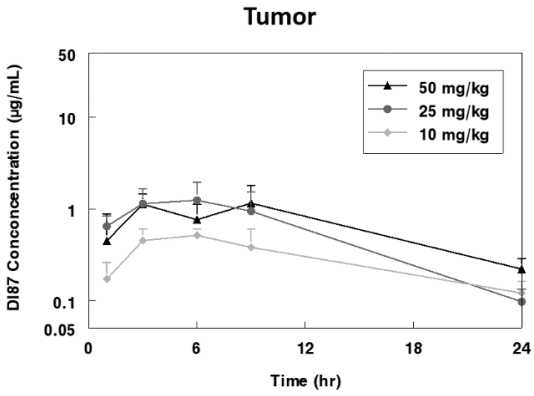

C

Plasma-Tumor PK model parameters	Parameter Estimate	Standard Error
CL (L/hr/kg)	0.46	0.03
V (L/kg)	2.78	0.22
KA (hr)	0.66 (FIXED)	.
Q (L/hr/kg)	0.0045	0.0013
Scalar	3.69	0.40
Half-life (hr)*	4.2	–
Eta1 (Scalar)	34.6%	0.08
Proportional Error	49.9%	0.04
DCK inhibition PK-PD model		
K_{out}	0.12	0.00011
E_{max}	1.20	0.00200
EC_{50}	0.31	0.00009
Gamma (Hill coefficient)	58.60	0.18500
K_{in}	0.76	0.00078
Additive Error	0.88	0.00025
Growth Inhibition PK-PD Model		
K_{out}	0.372	0.0973
E_{max}	1.06	0.2030
Growth Function Exp 1	0.00498	0.0011
Growth Function Exp 2	1.47	0.0399
EC_{50}	3.63	1.19
Intersubject Variability (E_{max})	14.1%	2.65%
Additive Error	0.20	0.02

*Half-life: 0.693/(CL/V).

Figure 1.3 | Plasma and tumor concentrations of DI-87 inform PK model. Plasma (A) and tumor (B) concentrations of DI-87. Each data point represents the plasma and tumor concentrations from a single mouse (n = 5 per time point). (C) PK-PD modeling parameter estimates.

Plasma and tumor pharmacokinetics (PK) was also evaluated in male mice following a 10 mg/kg dose, with essentially identical results to those seen in female mice. A population PK model was initially developed for plasma concentrations, with a one-compartment structural model fitting the data well. An additional compartment was added to model tumor concentrations. The parameter estimates for the combined tumor and plasma population PK model are shown in **Figure 1.3C**, with actual tumor volumes used in the model. KA was fixed to the parameter estimate obtained from the plasma PK model. The typical clearance value was 0.46 L/hr/kg and the plasma volume of distribution was 2.78 L/kg. Tumor sizes varied between experiments and it was thus difficult to determine whether tumor concentrations were linear.

1.1.3 dCK Inhibition Studies

DI-87 was administered to mice at three separate doses (5, 10, and 25 mg/kg) to establish a dose response curve. The [^{18}F]CFA PET probe was administered three hr prior to imaging. Representative mice at each time point and concentration are shown in **Figure 1.4A**, and data from all mice is represented graphically in **Figure 1.4B**. The 25 mg/kg dose exhibited full dCK inhibition for 27 hr, with protein activity fully recovering by 36 hr. The 10 mg/kg dose resulted in full inhibition with recovery initiating at the 12 hr time point. The 5 mg/kg dose resulted in minimal dCK inhibition with rapid recovery.

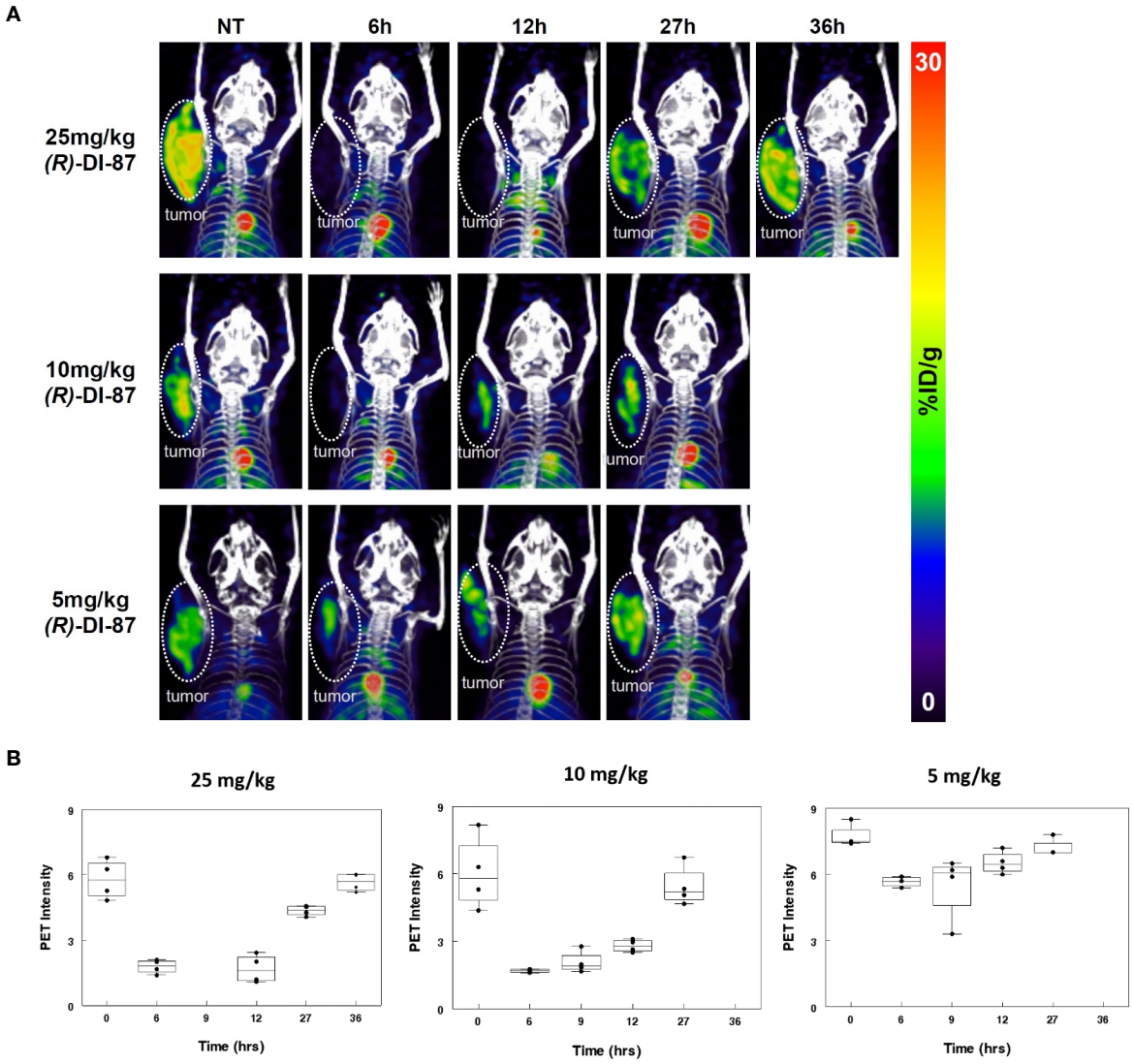

Figure 1.4 | PET imaging reveals *in vivo* efficacy of DI-87. (A) dCK activity in CEM xenograft tumors, as visualized *via* PET imaging using [^{18}F]CFA, from representative mice at DI-87 doses of 5 mg/kg, 10 mg/kg, and 25 mg/kg. (B) dCK activity as measured by PET quantified for all mice. NT; no treatment.

The quantitative data generated from PET signal intensity was used in a combined population PK-PD model. PK parameters from the final combined plasma-tumor model were

fixed and PD parameters were estimated in NONMEM. A sigmoid E_{max} indirect response PD model[32] was found to fit the dCK inhibition data the best:

$$\frac{dA}{dT} = k_{in} * (1 - Sigmoid\ E_{max}) - k_{out} * A$$

Final parameter estimates from the model are shown in **Figure 1.3C**. E_{max} was 1.20 and EC_{50} was 0.31 μg/mL. The Hill coefficient of 58.6 was consistent with the full dCK inhibition seen at the six hr time point for the 25 and 10 mg/kg doses, demonstrating that dCK inhibition is essentially a step function at higher concentrations with the transition from no inhibition to full inhibition being achieved over a relatively narrow range of concentrations.

1.1.4 Growth Inhibition Studies

Based on the results from the dCK inhibition experiments, we predicted close to full dCK inhibition following 25 mg/kg DI-87 dosing. Tumor growth inhibition studies were performed in CEM xenograft tumors using 25 mg/kg daily of DI-87 in combination with a fixed dose of i.p. thymidine, since DI-87 alone exhibits minimal growth inhibition (**Figure 1.5A**). Oral DI-87 at 10 mg/kg was given in combination with i.p. thymidine to demonstrate a dose–response relationship with reduced dCK inhibition. Control mice received either intraperitoneal saline injections alone, oral DI-87 with i.p saline injections, or thymidine alone; mice administered DI-87 or thymidine alone had tumor growth curves similar to control (data not shown). Tumor size was measured eery three days after the initiation of drug treatment. Increasing DI-87 doses resulted in significantly reduced tumor growth over the course of the experiment, consistent with the dCK inhibition observed in the PET scans. These results were validated in a repeat study where we explored the effect of full dCK inhibition throughout the dosing interval, with 25 mg/kg of DI-87

administered twice daily (BID) in combination with a fixed dose of thymidine as the highest dose (**Figure 1.5B**). BID administration of 25 mg/kg DI-87 with thymidine resulted in near complete arrest of tumor growth.

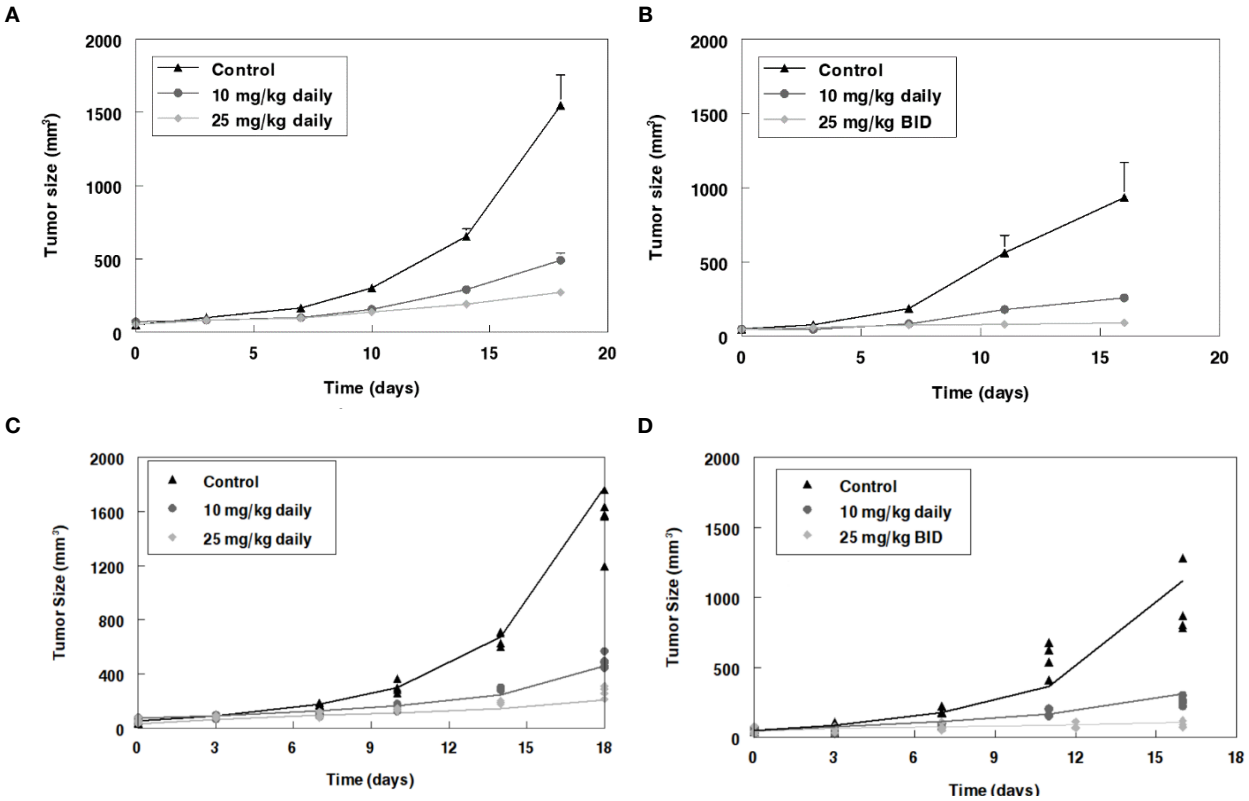

Figure 1.5 | DI-87 co-administered with thymidine inhibits tumor growth *in vivo*, with PK model accurately predicting tumor growth outcomes. (A) Growth of CEM xenograft tumors during DI-87 and thymidine treatment. DI-87 administered at 10 mg/kg or 25 mg/kg daily in combination with thymidine (n = 5 per dose). (B) Tumor growth inhibition following 25 mg/kg BID DI-87 with thymidine (n = 5 per dose). (C, D) Growth inhibition simulation of daily (C) or BID (D) 25 mg/kg DI-87 administration using final PK-PD model.

The tumor sizes from the two studies were used in a combined PK-PD model. PK parameters from the final combined plasma-tumor model were fixed and PD parameters were estimated in NONMEM. A super-exponential function was found to describe the growth of the

control data the best: Growth(t) = $e^{k1*t^{k2}}$. An E_{max} indirect response PD model[32] was found fit the growth inhibition data the best:

$$\frac{dA}{dT} = k_{in} - k_{out} * (1 + E_{max}) - (56 * k_1 * k_2 * (TIME^{k2-1})) * A$$

The final model was used for simulations of two concentrations – 10 mg/kg daily, and 25 mg/kg BID – which demonstrated that the final model fit the experimental data well (**Figures 1.5C** and **1.5D**). Thus, maximal dCK inhibition over the 24 hr dosing period results in greater growth inhibition, consistent with the 25 mg/kg BID dose.

1.1.5 Discussion

Following its synthesis, inhibition of [^{3}H]-dC uptake confirmed that DI-87 was a potent inhibitor of dCK, with an IC_{50} of 4.3 nM. The affinity of DI-87 for dCK was further confirmed through a rescue assay in which the growth of CEM cells treated with gemcitabine with and without DI-87 supplementation was monitored. Gemcitabine requires dCK for its cytotoxic effects, and administration of DI-87 fully prevented cytotoxicity following gemcitabine treatment, thereby demonstrating the dCK inhibition of DI-87. Previous generations of reversible dCK inhibitors developed by our group had comparable potency, but did not have optimal biochemical properties. DI-87 improves upon these properties while maintaining low-nM affinity for dCK. In particular, DI-82 was an effective dCK inhibitor but was heavily protein-bound. By comparison, DI-87 retained its potency in the presence of albumin.

The preclinical pharmacology of DI-87 was also evaluated. Plasma concentrations peaked 3 hr after oral administration, while tumor concentrations maintained a peak between hours 3 and 9. Thus, the tumor-to-plasma concentration ratio was dependent upon sampling time.

Tumor concentrations were significantly lower than plasma concentrations for all doses tested. The PET probe [^{18}F]CFA was used to quantify dCK activity, and thus effects of DI-87 upon the target pathway, in tumors. Given the differential peaks in plasma and tumor concentrations, linking DI-87 tumor concentrations to dCK inhibition provided a more physiologic and mechanistic approach. Our population PK-PD modeling allowed us to describe limited tumor data and link these concentrations to dCK inhibition. Full dCK inhibition occurred at the 10 mg/kg dose and increasing doses led to a longer maintenance of full inhibition. At the highest dose tested (25 mg/kg), full recovery of enzyme activity occurred by 36 h, with full inhibition being maintained at the 12 hr time point. Our PK-PD model suggested a threshold or rapid switching on-off effect. When evaluated as a single agent, DI-87 was well tolerated at higher doses, but had essentially no ability to inhibit growth in CEM xenograft tumors (data not shown). When DI-87 was administered as repeated doses in combination with thymidine, full dCK inhibition was maintained at 12 hr (25 mg/kg twice daily dose) and led to maximal tumor growth inhibition. Lower doses led to diminished dCK inhibition with predictable decreases in growth inhibition. Thus, DI-87 appears to have potential as a cancer therapeutic when used in combination with thymidine.

The PET probe used in the current study is a tool to help provide mechanistically-driven rational dosing of DI-87 and similar compounds prior to clinical trials. The use of non-invasive PET probes and scans can greatly aid in drug development. Imaging studies in early phase development can confirm that molecules reach the target tissue and do not accumulate in target sites, can determine dose-target occupancy, and can be used to help critically evaluate similar drug candidates based on responses.[33] Our group developed [^{18}F]FAC (1-(2′-deoxy- 2′-

[^{18}F]fluoro-β-D-arabinofuranosyl)cytosine) as the first dCK-specific PET probe, and the compound has subsequently been used in the preclinical drug development of small molecule dCK inhibitors.[21,30] A more specific probe, [^{18}F]CFA, was later developed by our group and was used in the current study to evaluate dCK activity in tumors when treated with a small molecule dCK inhibitor. This probe was also scheduled for study in a clinical trial at UCLA to evaluate changes in dCK activity following cancer immunotherapy, though the trial was terminated due to slow accrual.[34] PET probes in preclinical and clinical studies can additionally aid in understanding how drug distribution in target tissues and response of the target pathway is modified in the presence of multiple drugs, as compared to single agent therapy. They can also help evaluate the degree of synergy, appropriate timing of therapies, and dosing amount.

Our growth inhibition studies utilized a fixed dose of thymidine with varying doses of DI-87, and dual inhibition of salvage and *de novo* pathways led to effective tumor growth inhibition when full dCK inhibition was achieved throughout the dosing interval. PET imaging provided valuable information, namely the quantification of dCK inhibition, which enabled a more efficient methodology for dose optimization as it allowed us to determine optimal dosing and schedules without testing a multitude of doses in growth inhibition studies. The DI-87 plasma half-life of 4 hr suggests the need for more frequent dosing to maintain dCK and growth inhibition, however our mechanistic approach which included evaluation of tumor PK and PET imaging allowed us to determine that the 25 mg/kg dose twice daily would be appropriate to maintain dCK inhibition.

Section Two:

Further Development of Novel Deoxycytidine Inhibitors

1.2.1 Basis for Further Structure-Activity Relationship Studies of dCKi Scaffold

Despite the promising *in vitro* and *in vivo* data of DI-87, it remained apparent that this clinical candidate had further room for improvement. Though the addition of the morpholine ring in Part A of the scaffold had improved its solubility when compared with previous lead compound DI-82, DI-87 remained relatively insoluble. Furthermore, previous dCKi analogs produced by our group had never strayed from a substituted phenyl ring in Part A of the scaffold. Additionally, the methyl stereocenter within the Part C linker posed a synthetic challenge – while the stereoselective Corey-Bakshi-Shibata reduction of the ketone intermediate led to the desired S-enantiomer of the alcohol intermediate in >99% ee, the subsequent S_N2 reaction to install the pyrimidine ring resulted in degradation of enantiopurity, most likely due to a competing S_N1 reaction pathway. This necessitated the use of chiral HPLC chromatography for purification to obtain a suitably enantiopure product. Attempts at achieving an asymmetric synthesis that did not require the use of chiral purification methods were unsuccessful, and previous work had established that the Part C methyl substituent was necessary for maintaining low-nM activity against dCK.[22,35] However, based upon co-crystal structures of previous lead compound DI-82 complexed with dCK, it was known that the chiral methyl substituent occupied a hydrophobic pocket within the substrate binding site of dCK. Taken together, these considerations revealed further opportunities for structure-activity relationship studies, specifically within Part A and Part C of the dCKi scaffold.

1.2.2 Synthesis and Evaluation of Novel dCKi – Modifications to Parts A, B and C

Based upon the hit compounds that emerged from the initial high-throughput screen conducted against dCK, as well as the subsequent SAR guided by both *in vitro* activity as well as co-crystallization studies, all dCKi synthesized by our group bore a substituted phenyl moiety in Part A. Upon examining the previous SAR, it was clear that Part A of the scaffold was able to accommodate a variety of modifications, in contrast to Parts B, C and D, which had much less flexibility in terms of retaining dCK affinity upon introducing diverse chemical moieties. Previous decisions regarding the nature of phenyl ring substitutions revolved around promoting additional favorable non-covalent interactions within the dCK binding site, as well as adding moieties which may have improved the overall solubility of the molecule, or incorporation of fluorine to enable the synthesis of dCK-specific PET probes.[21,36] However, co-crystal structures provided evidence that the pocket within which our dCKi were binding was able to tolerate groups other than substituted phenyl rings. As such, we set out to determine whether we could improve the activity and/or solubility of our dCKi, while also improving Lipinski's "rule of five" metrics,[37,38] through diversifying Part A of the scaffold. Our general synthetic scheme began with an appropriate nitrile-bearing thioamide precursor (**A**) or starting directly from the thioamide (**B**), followed by a Hantzsch thiazole synthesis reaction with an appropriate α-bromo ketone (commonly 4-bromo-2,3-pentanedione) which yielded the ketone-substituted thiazole intermediate (**C**) (**Scheme 1.2**). The ketone was was then reduced to the secondary alcohol (**D**) *via* DIBAL-H-mediated reduction. Activation of the alcohol *via* reaction with trifluoroacetic anhydride yielded a trifluoroactate intermediate (**E**), which was displaced by 2-mercapto-4,6-diaminopyrimidine under thermal conditions in the presence of base to produce the desired dCKi

compound (**F**). All compounds were synthesized in their racemic form for initial evaluation purposes.

Scheme 1.2 | General synthetic strategy for synthesis of dCK inhibitors[a]

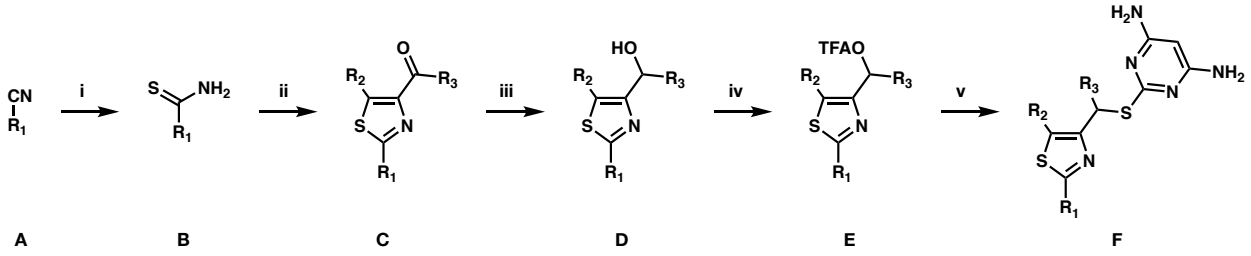

[a]Reagents and conditions: (i) $(NH_4)_2S$ (20% aqueous), Et_3N, Pyridine, 60 °C, 12 hr; (ii) Appropriate α-bromo ketone, ethanol, reflux, 3 hr; (iii) DIBAL-H, THF, 0 °C, 1 hr; (iv) Trifluoroacetic anhydride, THF, 0° C, 0.5 hr; 4,6-diamino-2-mercaptopyrimidine, Cs_2CO_3, DMF, 70°.

Former lead compounds DI-39, DI-82, and DI-87 each had substituted phenyl rings meant to improve drug-like properties such as solubility, and crystallographic studies showed that the sulfonamide extending from the meta position of DI-82 made key hydrogen-bonding interactions within the dCK protein binding site (**Figure 1.6**).[21,22,39] Thus, the first compound synthesized in this study, **NMc-1**, stood in stark contrast to our group's previously synthesized dCKi as it possessed an unsubstituted phenyl ring (**Figure 1.7**). Compounds **NMc 2–5**, bearing alkyl and heterocyclic moieties in Part A, continued the trend of straying from previously synthesized analogs. dCK inhibitory activity of all compounds was assessed *in vitro* as previously reported.[21,22]

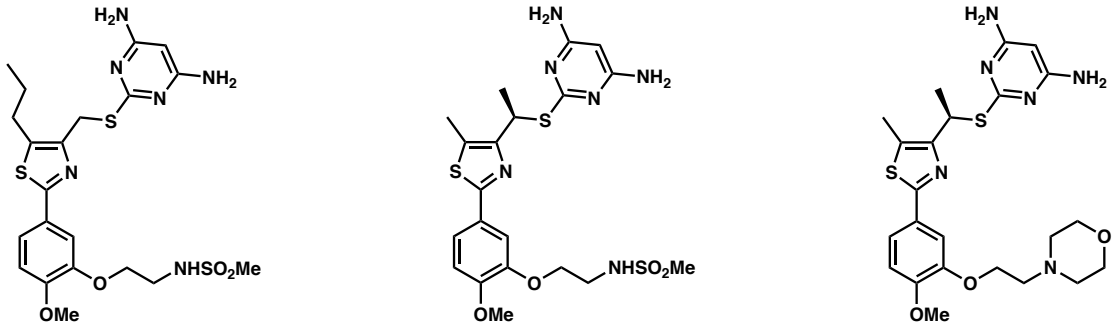

Figure 1.6 | Former lead dCK inhibitor compounds DI-39 and DI-82, and current lead compound DI-87. IC_{50} values measured through inhibition of [^{3}H]-dC uptake in CEM T-ALL cells.

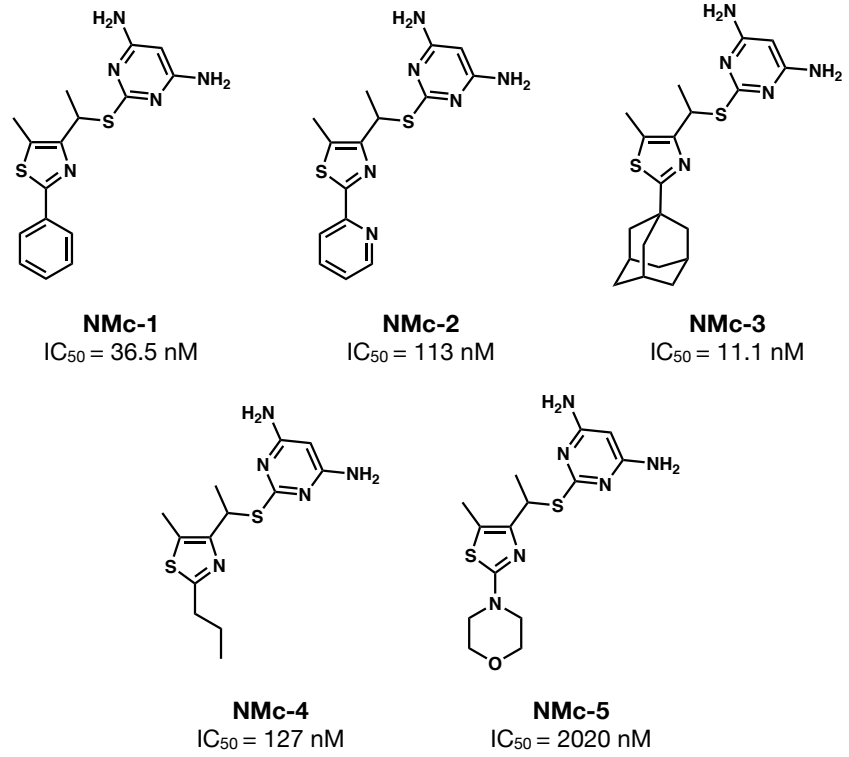

Figure 1.7 | Structures and IC_{50} values of dCK inhibitors possessing varied Part A moieties.

IC_{50} values measured through inhibition of [^{3}H]-dC uptake in CEM T-ALL cells.

Encouragingly, compound **NMc-1** showed high affinity for dCK, with an IC_{50} of 36.5 nM. The low-nM activity buttressed the hypothesis that Part A of the dCKi scaffold was able to accommodate a variety of functional groups, and that groups adorning the phenyl ring may play only modest roles in promoting affinity for dCK. Further modifications to Part A had varied results in terms of dCK binding ability. The pyridine-containing **NMc-2** had an IC_{50} of 113 nM, indicating that aromatic heterocycles may not be as well-tolerated as phenyl rings. Non-aromatic compounds **NMc 3–5** had surprising activities – the adamantyl-containing **NMc-3** had very strong affinity for dCK, with an IC_{50} of 11.1 nM, which was essentially identical to the racemic sample of previously identified lead compound DI-87. The propyl-substituted **NMc-4** saw a ten-fold decrease in activity, relative to **NMc-3**, while the morpholino **NMc-5** was more than 180-fold less active. The surprising affinity of **NMc-3** was hypothesized to stem from its overall decrease in polarity, which would allow for greater cell permeability and greater opportunity for inhibition of dCK. The decrease in dCK affinity displayed by **NMc-4** may stem from a non-polar character which was insufficient to enable the same level of cell permeation, and therefore dCK inhibition, as **NMc-3**. While **NMc-3** was more straightforward in its synthesis when compared with DI-87 and just as active, it was less soluble. The morpholino **NMc-5**, which was synthesized with the hope that the morpholine ring would improve solubility while maintaining low-nM activity, accomplished neither – the compound displayed the lowest IC_{50} of any of the five compounds synthesized, and did not possess noticeably improved solubility when compared with DI-87.

While Part A of our dCKi scaffold had proven itself amenable to modification, Parts B and C had shown a lower degree of flexibility in our previous studies. The 5-position of the

thiazole ring could accommodate short alkyl chains and maintain strong affinity for dCK, with propyl chains leading to the highest affinity. However, this affinity came at the cost of metabolic stability – propyl and ethyl substitutions correlated with rapid metabolism, while a smaller methyl substituent at the 5-position was more stable, albeit less active. The low-nM affinity for dCK was not recovered until a methyl group was incorporated into Part C of the scaffold, with the *R*-enantiomer being the more active species. Crystallography studies revealed that the methyl group occupied a hydrophobic pocket of the dCK substrate binding site. However, enantioselective synthesis of dCKi compounds proved to be elusive,[35] and enrichment of the desired enantiomer could only be realized through chiral chromatography. In an effort to address this issue, we sought to incorporate an achiral alkyl moiety within Part C of the dCKi scaffold, specifically a *gem*-dimethyl. We envisioned that the *gem*-dimethyl would be able to optimally fill the hydrophobic pocket while simultaneously eliminating the chirality of our dCKi. Extensive efforts were undertaken in order to identify methodology which would enable construction of the desired *gem*-dimethyl-mercaptopyrimidine connection. However, installation of this moiety proved to be non-trivial, as attempts commonly afforded the alkene elimination product. Eventually, a procedure was adapted in which the ketone-substituted thiazole intermediate **9** was converted to the tertiary alcohol **10** by reaction with methyl Grignard reagent (**Scheme 1.3A**). Subsequent stirring of **10** in diethyl ether in the presence of thionyl chloride and sodium carbonate at 0 °C yielded the tertiary chloride **11**,[40] which after filtration and concentration using low temperature roto-evaporation was not isolated due to instability and instead directly displaced by 4,6-diaminopyrimidine thiolate. This yielded **12**, which bore the desired *gem*-dimethyl-mercaptopyrimidine connection.[41]

Scheme 1.3 | Synthesis of dCK inhibitors bearing *gem*-dimethyl Part C moiety[a]

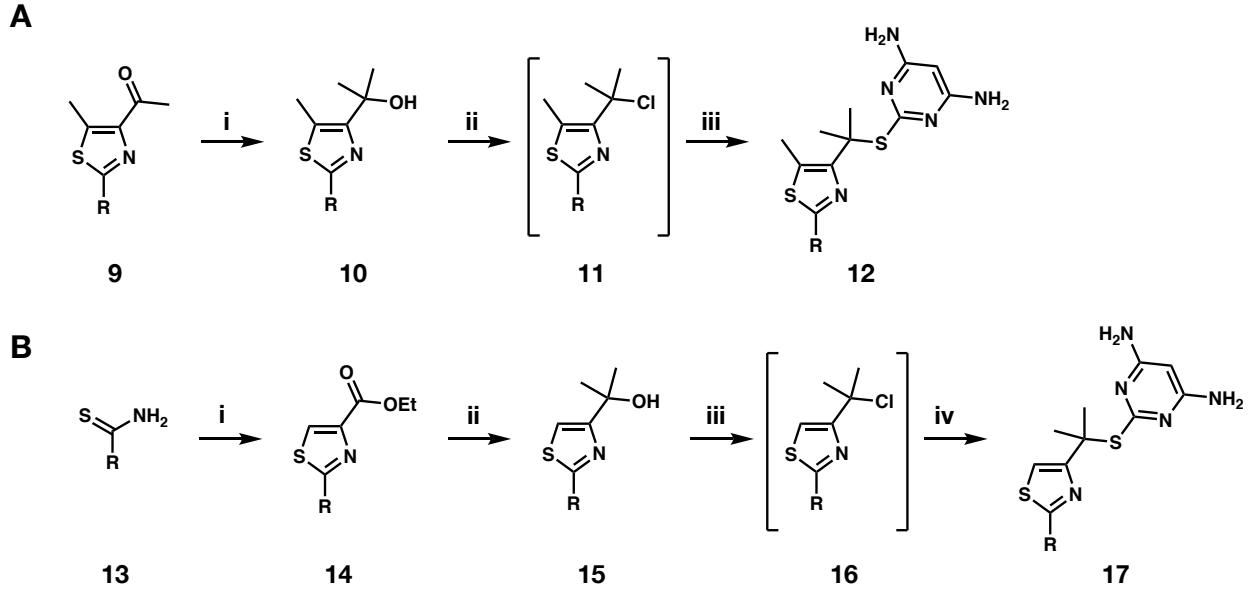

[a]Reagents and conditions: **A**; (i) methyl magnesium bromide, THF, 0 °C, 1 hr; (ii) $SOCl_2$, Na_2CO_3, ether, 0 °C, 0.25 hr; (iii) sodium 4,6-diaminopyrimidine-2-thiolate, Cs_2CO_3, DMF, 65 °C, 4 hr. **B**; (i) ethyl bromopyruvate, ethanol, reflux, 3 hr; (ii) methyl magnesium bromide, THF, 0 °C, 1 hr; (iii) $SOCl_2$, Na_2CO_3, ether, 0 °C, 0.25 h; (iv) sodium 4,6-diaminopyrimidine-2-thiolate, Cs_2CO_3, DMF, 65 °C, 4 hr.

With a dCK IC_{50} of 924.5 nM, the initial *gem*-dimethyl dCKi analog synthesized using this methodology, **NMc-6**, proved to be significantly less potent against dCK than its mono-methylated analog **NMc-1** (**Figure 1.8A**). It was hypothesized that this loss of activity was the result of steric interactions between the *gem*-dimethyl moiety and the 5-methyl substituted thiazole which prevented the dCKi from adopting an optimal conformation for binding to dCK within the substrate binding site. To nullify this interaction, ethyl bromopyruvate was utilized in the Hantzsch thiazole synthesis reaction step of our synthetic scheme instead of 4-bromo-2,3-

pentanedione, which resulted in a 5-hydrido thiazole (**14**) rather than the 5-methyl analog (**Scheme 1.3B**). By utilizing this substrate for construction of the thiazole, **NMc-7** was generated, which demonstrated three-fold higher dCK affinity than the 5-methylthiazole **NMc-6**. Based upon this improvement in dCK affinity, compounds bearing the *gem*-dimethyl and 5-hydrido thiazole moieties but retaining Part A groups from previous analogs were synthesized (**Figure 1.8A**). Unfortunately, these compounds were not able to recapitulate the low-nM activity of our lead compound DI-87. The *gem*-dimethyl and adamantyl-containing **NMc-8** was roughly 15-fold less active than its potent mono-methyl analog and constitutional isomer **NMc-3**. Likewise, the *gem*-dimethyl analog and constitutional isomer of DI-87, **NMc-9**, demonstrated a similar decrease in activity.

Using the previously outlined methodology, dCKi analogs were synthesized in which Parts A, B and C were simultaneously altered in order to differ from the structure of DI-87 (**Figure 1.8B**). G*em*-dimethyl compounds explored included those bearing fluorinated phenyl rings (**NMc-12**, **NMc-13**), compounds bearing alkyl groups at the 2-position of the thiazole ring (**NMc-14**, **NMc-15**), and a compound possessing an oxadiazole ring extending from the thiazole 2-position (**NMc-16**). The most potent compound, **NMc-10**, had an IC_{50} of 37.2 nM, and may have benefited from favorable hydrogen bonding interactions within the substrate binding site of of dCK due to the phenolic alcohol moiety. However, no other analogs generated in this portion of our synthetic campaign showed sub-100 nM activity against dCK.

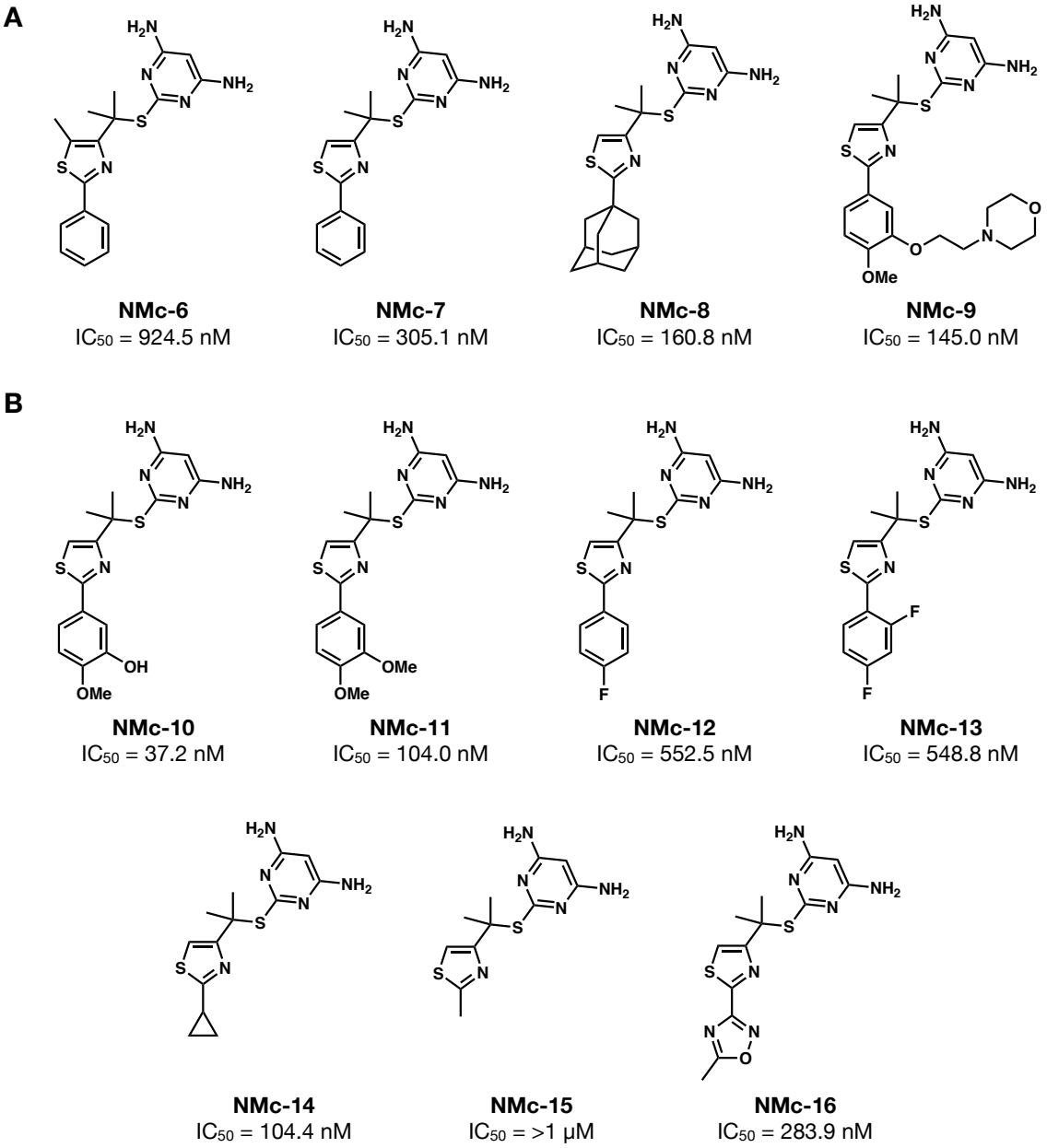

Figure 1.8 | dCK inhibitors bearing *gem*-dimethyl moiety in Part C. (A) dCK inhibiting compounds bearing *gem*-dimethyl moieties in Part C while maintaining Part A substituents of previously-synthesized compounds. (B) dCK inhibiting compounds bearing *gem*-dimethyl moieties in Part C and previously unexplored Part A moieties. IC_{50} values determined through inhibition of [^{3}H]-dC uptake in CEM T-ALL cells.

1.2.3 *gem*-Dimethyl dCKi Analogs Adopt Unfavorable Gauche Conformation While Binding dCK

While the decreased dCK affinity of our *gem*-dimethyl analogs was disappointing, it was not entirely unpredictable. The chiral methyl substituting in Part C of lead compound DI-87 occupied a small hydrophobic pocket within the substrate binding site of dCK, and it was hypothesized that the *gem*-dimethyl group was too large to similarly occupy this space. Additionally, the difference in affinity between **NMc-1**, **NMc-6**, and **NMc-7** indicated that conformational differences engendered by the *gem*-dimethyl moiety were affecting the affinity of our newly synthesized analogs. In order to better understand the origins of the decreased affinity our *gem*-dimethyl analogs had for dCK, we utilized molecular dynamics (MD) simulations to examine the binding modes of selected dCK inhibitors within the substrate binding pocket of the protein. Lead compound DI-87 served as the positive control, while the *gem*-dimethyl compounds **NMc-7**, **NMc-9**, and **NMc-10** were evaluated (**Figure 1.9A**). The initial binding conformations chosen for the MD simulations emulated those which were reported for previous lead compound DI-82.[36] In our simulations, the achiral *gem*-dimethyl compounds underwent large conformational changes. In the initial binding conformation, the dihedral [C-S-C-C] angle between the pyrimidine and thiazole rings is near 150°, with the pyrimidine ring oriented far away from the thiazole (**Figure 1.9B**). As the simulation progressed, the binding conformations of the *gem*-dimethyl compounds change from an anti to a gauche conformation, with a dihedral angle of 50° (**Figure 1.9C**). Conversely, DI-87 maintains the anti conformation, with the dihedral angle remaining near 150° throughout the duration of the MD simulation.

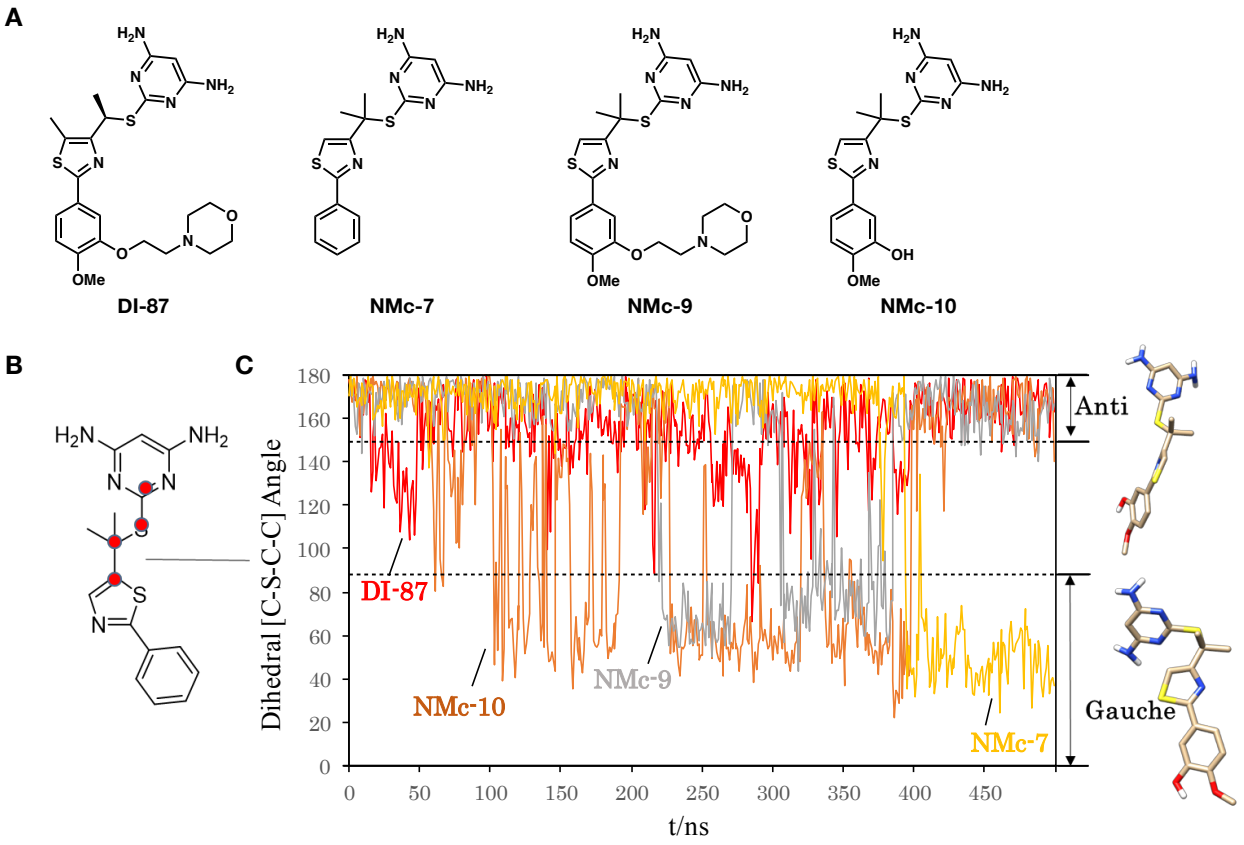

Figure 1.9 | Molecular dynamics (MD) simulation of dCK inhibitor conformations in dCK binding pocket. (A) Structures of examined dCK inhibitors. (B) Representation of investigated dihedral C-S-C-C bond angle. (C) MD simulation of dCK inhibitor conformation within dCK binding pocket, with representational anti and gauche conformer structure snapshots for NMc-10.

We further computed the energies of the dCKi conformations and scanned the energy surface along the dihedral angle using the density functional theory (DFT) method. For lead compound DI-87, the most stable conformer is the anti with a dihedral angle of 150°–210° (**Figure 1.10A**). The energy increases monotonically as the dihedral angle decreases beyond 150°. For **NMc-7**, the energy surface has two minima at 180° and 60°, which correspond to the anti and gauche conformations, respectively, which were observed in the MD simulations. The

gauche conformation of DI-87 is 1.6 kcal/mol higher in energy than the anti, which is a result of the steric effects between an amine group of the pyrimidine ring and the 5-position methyl of the thiazole (**Figure 1.10B**). In **NMc-7**, which lacks a methyl group at the 5-position, the gauche conformation is 0.7 kcal/mol lower in energy than the anti (**Figure 1.10C**). Due to the absence of the thiazole methyl, this conformation lacks the steric effects observed in DI-87, leading to the lower energy of the gauche versus anti conformation.

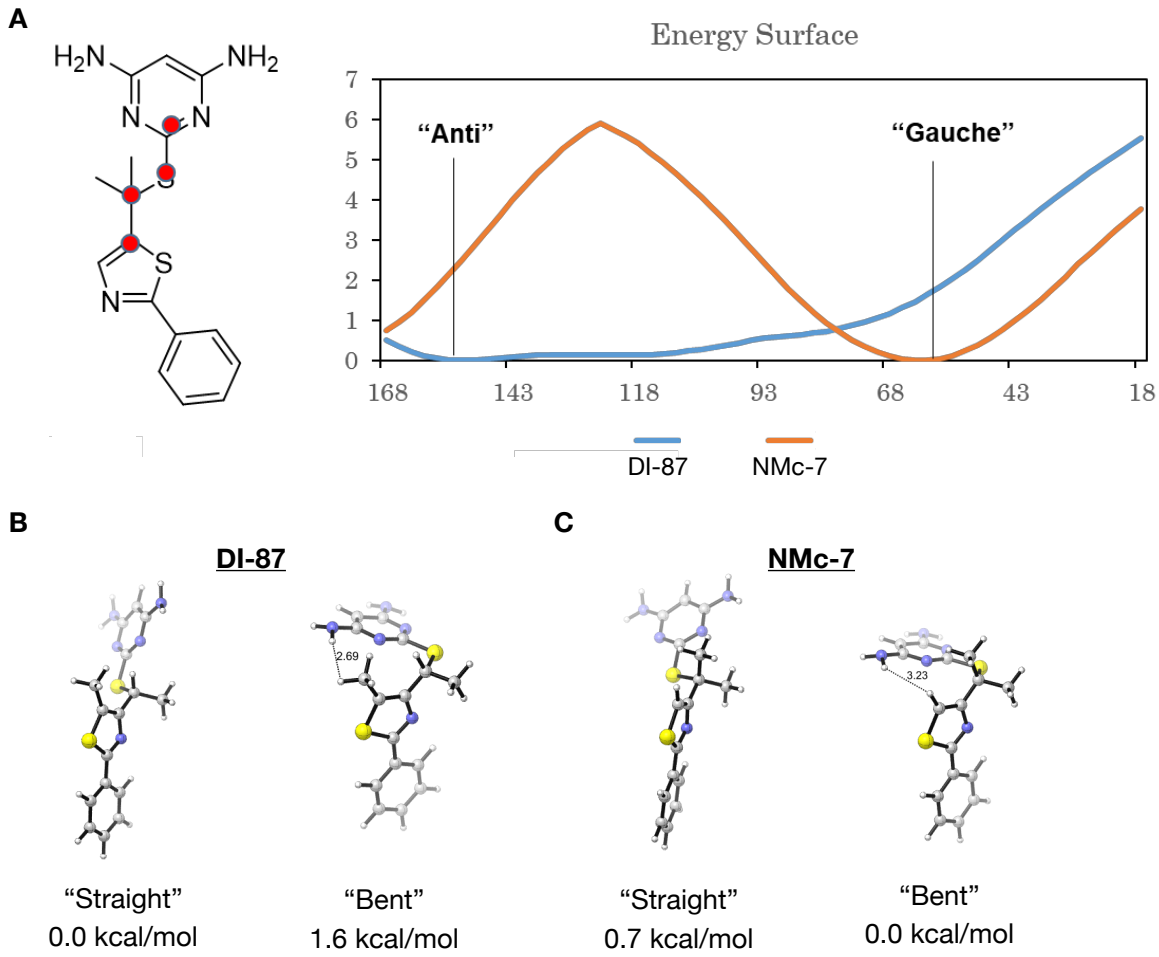

Figure 1.10 | Energy scan reveals conformational preferences of dCK inhibitors. (A) The conformation energies of DI-87 and NMc-7 were computed and the energy surface along the dihedral [C-S-C-C] angle scanned with density functional theory (DFT) method. (B, C) Conformational energies of DI-87 (B) and NMc-7 (C).

The gauche and anti conformations of the *gem*-dimethyl compounds bind differently within the substrate binding site of dCK. In the anti conformation of **NMc-10**, three key hydrogen bonds are formed between the amino groups of the pyrimidine ring and Q97, D133, and E53 of the dCK substrate binding pocket. However, only one hydrogen bond with Q97 is maintained in the gauche conformation (**Figure 1.11**). These hydrogen bonding interactions between the pyrimidine and amino acid residues within the binding site were demonstrated to be key to our scaffold's ability to inhibit dCK in our previous SAR studies.[22] Removal of one or both amino groups from the pyrimidine ring led to substantial or near-complete loss of activity, respectively. Because the MD simulations demonstrated that **NMc-10** and other *gem*-dimethyl compounds evaluated transition between the two conformations, we concluded that the *gem*-dimethyl dCKi compounds displayed lower affinity for dCK due to fewer key hydrogen bonding interactions within the binding site, which was the result of a more energetically favorable gauche conformation enabled by the absence of a 5-methyl substituted thiazole ring.

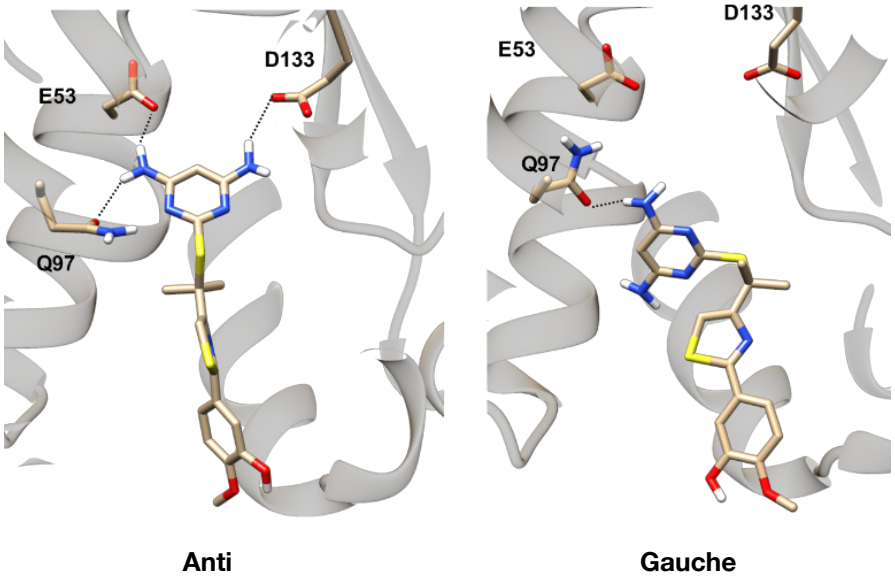

Figure 1.11 | Hydrogen bonding interactions of anti and gauche conformations of NMc-10 within dCK binding site.

Section Three:

Evaluation of dCK Inhibitors as Nucleoside Mimetics

1.3.1 dCKi Scaffold as a Nucleoside Mimetic

The first kinase inhibitor, reported in 1984, engaged its target through binding at the phosphoryl donor (ATP) binding site of Cyclic Nucleotide Dependent Protein Kinase and Protein Kinase C.[42] Since this discovery, the majority of kinase inhibitors utilized across all indications have adopted this same targeting strategy, namely binding to the ATP binding site of a kinase by mimicking the hydrogen bonding interactions between the kinase and the adenosine ring of ATP.[43,44] This common targeting modality is enabled by a highly conserved ATP binding region located in a cleft formed between two lobes of the kinase secondary structure.[45,46] Due to the conserved nature of this ATP binding region, small molecule ATP-competitive inhibitors are commonly discovered through high throughput screening and synthetic campaigns. The obvious obstacle posed by the conserved nature of this binding region is the similarity between kinases, which can lead to significant off-target effects for a given kinase inhibitor. It is therefore advantageous to develop inhibitors which bind at sites other than the ATP-binding site, thereby imbuing a potential for greater kinase-specificity upon the molecule. For this reason, our group was encouraged by the serendipitous discovery of inhibitors of dCK which bound not at the phosphoryl donor site, but at the substrate binding site.[21,36] dCK phosphorylates dC, dA, and dG nucleosides into their monophosphate nucleotide forms, and the dCKi scaffold identified through our high-throughput screen prevents these nucleosides from binding through competitive inhibition. For this reason, our dCKi can be classified not simply as kinase inhibitors, but as

nucleoside mimetics (nucleomimetics). Through this frameshift, we came to envision our dCKi as having the potential for broader effects within nucleotide metabolism.

1.3.2 Evaluation of Nucleomimetic dCK Inhibitors as Modulators of Pyrimidine Nucleotide Metabolism

In order to assess the potential of our nucleomimetic dCK inhibitors as having broader effects, we designed a phenotypic screening platform for the identification of novel modulators of pyrimidine nucleotide metabolism.[47] The design and technical details of this screening platform are expounded upon in Chapter Two of this dissertation, though an overview is provided here. While dCK is able to phosphorylate multiple nucleosides, it has the highest affinity for the pyrimidine nucleoside dC. All pyrimidine nucleotides arise from a common precursor; uridine monophosphate (UMP). UMP is produced by separate but convergent biosynthetic pathways – the *de novo* pathway (DNP), which assembles UMP from amino acids and glucose in a six-step process, and the nucleoside salvage pathway (NSP), which salvages preformed uridine from the extracellular space and phosphorylates it to UMP. The general design of our screen involved forcing cells to rely upon only one of these pathways for UMP production, and then incubating the cells with our dCKi and identifying which compound(s) caused a decrease in UMP production in the studied pathway (**Figure 1.12A**). In order to promote conditions in which UMP could only be produced *via* the DNP – a condition termed DNP-only – cells were incubated in media without uridine (rU) supplementation. With no rU present, the NSP lacks its substrate and cells must rely upon the DNP for UMP production. To force cells to rely upon the NSP – termed NSP-only – they were incubated with rU and NITD-982, a potent and specific inhibitor of dihydroorotate dehydrogenase (DHODH), a key

enzyme of the DNP pathway. Baseline conditions were those in which both the DNP and NSP were active – achieved by incubating cells in the presence of rU and absence of NITD-982.

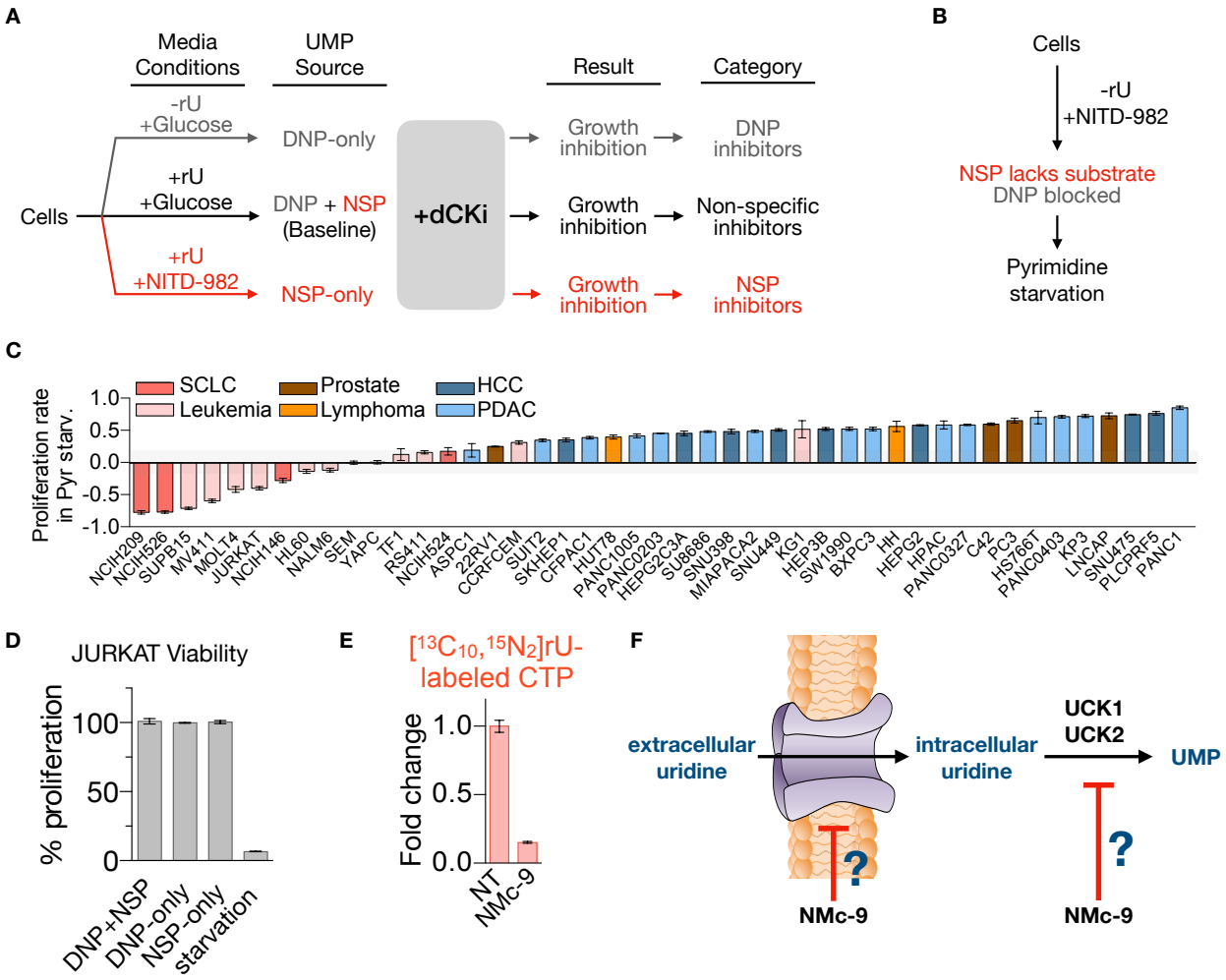

Figure 1.12 | Design of a phenotypic metabolic modifier screen to evaluate ability dCK inhibitor compounds to disrupt pyrimidine nucleotide metabolism. (A) Schematic of screen design. (B) Schematic of media conditions which lead to pyrimidine starvation. (C) Proliferation rates while incubated in pyrimidine starvation conditions for a panel of cancer cell lines. % proliferation values were calculated using Cell Titer Glo (CTG) following 72 hr treatment (7-point dose response; n=2). (D) Proliferation of JURKAT cells in baseline (DNP + NSP), DNP-only, NSP-only, and pyrimidine starvation media conditions, normalized to baseline. (E) LC-MS/

MS analysis of [$^{13}C_9$; $^{15}N_2$] rU (10 μM) utilization for DNA-C replication shows NMc-9 inhibits the incorporation of [$^{13}C_{10}$, $^{15}N_2$]rU-labeled CTP into newly-synthesized DNA. (F) Schematic of potential cellular targets of NMc-9. NT; no treatment.

A panel of cancer cell lines was screened in order to identify those which displayed a decrease in proliferation when unable to produce pyrimidine nucleotides through either the DNP or NSP, conditions termed "pyrimidine starvation" (**Figure 1.12B**, **1.12C**). Identifying such cell lines enabled our screen to have a phenotypic readout – namely a quantifiable decrease in proliferation upon concurrent inhibition of the DNP and NSP. Cell Titer Glo was utilized to evaluate proliferation impairment. Following this initial survey of cancer cell lines, the T lymphocyte cell line JURKAT was chosen for the screening platform as it showed a large decrease in proliferation under pyrimidine starvation conditions, but was able to recapitulate baseline (DNP and NSP both active) proliferation levels when reliant upon either the DNP or NSP alone (**Figure 1.12D**).

To carry out the screen, JURKAT cells were incubated in three conditions – DNP-only, NSP-only, and baseline. dCKi which inhibited growth in DNP-only conditions were categorized as DNP inhibitors, while dCKi which inhibited growth in NSP-only conditions were categorized as NSP inhibitors and those which inhibited growth in baseline conditions were categorized as non-specific inhibitors. 65 nucleomimetic dCK inhibitor compounds synthesized by our group were screened for activity and subsequently ranked by pathway-specific index scores, calculated as the ratio of compound IC_{50} values against baseline conditions versus pathway-specific. Higher index scores correlated with higher pathway specificity. Following the screen, the two top scoring compounds against the DNP were resynthesized and tested again, only to reveal that the

initial hits were a false-positives. The top-scoring compound against the NSP, **NMc-9**, demonstrated an IC_{50} of 11.4 μM which correlated with an index score of 8.77. LC-MS/MS analysis of incorporation of radiolabeled nucleotides into newly synthesized DNA showed that **NMc-9** significantly limited the amount of rU-derived CTP compared to baseline (**Figure 1.12E**).

It was reasoned that in order to exert its NSP-inhibitory action, **NMc-9** was acting at one of two levels of the NSP – either the nucleoside transport level or the kinase level (**Figure 1.12F**). In the NSP of UMP biosynthesis, uridine nucleosides are salvaged from the extracellular space and transported into the cell *via* specialized nucleoside transporters (JURKAT cells express the equilibrative nucleoside transporter 1 (ENT1) gene SLC29A1).[48] Once inside the cell, they are phosphorylated to UMP by uridine-cytidine kinase (UCK), a pyrimidine ribonucleoside kinase which exists in two primary isoforms – UCK1 and UCK2. UCK2 has been shown to possess a significantly higher catalytic efficiency when compared with UCK1.[49] In addition to catalyzing the first step of the pyrimidine NSP, UCK also phosphorylates several nucleoside analog prodrugs which have found investigational interest as chemotherapeutic agents.[12,49,50]

To determine at which level **NMc-9** was acting, we first profiled its ability to prevent the uptake of [^{3}H]Uridine in intact cells. The FDA-approved nucleoside transport inhibitor dipyridamole was included as a positive control, and **NMc-1**, which had no effect upon the NSP in our screen, was included as a negative control. Both **NMc-9** and dipyridamole treatment led to a significant decrease in [^{3}H]Uridine uptake, while **NMc-1** did not impact uptake at all. Next, we assayed the ability of **NMc-9** to inhibit the phosphorylation of [^{3}H]Uridine to UMP in lysed

cells. Cytidine triphosphate (CTP), a negative allosteric regulator of UCK, was included as a positive control for UCK inhibition. Treatment with **NMc-9** or CTP showed a significant decrease in [^{3}H]Uridine phosphorylation, relative to no treatment or treatment with negative control. Together, these results indicate that **NMc-9** is disrupting the NSP through inhibition of UCK.

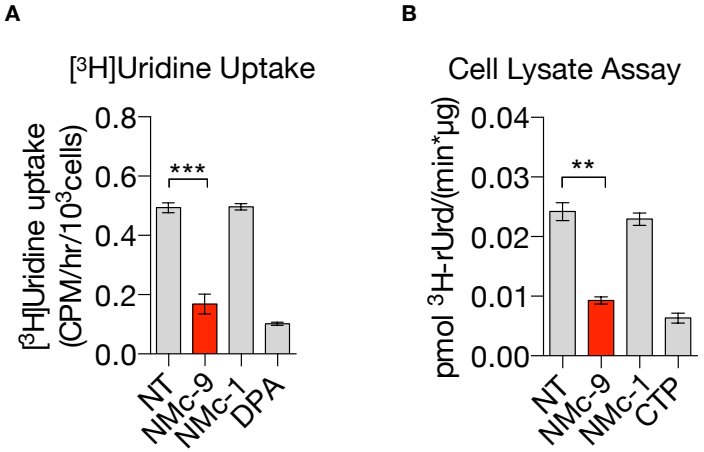

Figure 1.13 | NMc-9 is a putative UCK inhibitor. (A) Inhibition of [^{3}H]Uridine uptake in JURKAT cells following 2 hr incubation ± 1 μM NMc-9, NMc-1, or dipyridamole (DPA). (B) Inhibition of [^{3}H]Uridine phosphorylation to [^{3}H]Uridine-monophosphate by NMc-9, NMc-1, and cytidine triphosphate (CTP). NT; no treatment. Mean±SD; n=3; one-way ANOVA corrected for multiple comparisons by Bonferroni adjustment; ** P<0.01; *** P<0.001.

1.4 Discussion

The importance of dCK in anticancer therapy has been recognized for decades, as this enzyme is the key activator of chemotherapeutic nucleoside analog drugs such as gemcitabine. However, despite our group having demonstrated the efficacy of inhibiting dCK function for the treatment of leukemia in mouse models, as well as defining its roles in hematopoiesis and cell

division, the potential clinical utility of dCK inhibition remains incompletely defined. As a constitutively expressed protein and key enzyme of the nucleoside salvage pathway, dCK and inhibition of its function have the potential to be leveraged in a number of therapeutic settings. For instance, our proposed mechanism of action against leukemic cells in which inhibition of both the *de novo* and salvage nucleotide biosynthetic pathways leads to unsustainable levels of replication stress in cancerous cells may be extended to other cancers such as pancreatic ductal adenocarcinoma (PDAC). Patients suffering from PDAC are in desperate need of new therapeutic options, as five year survival rates are <9%.[51] In part due to a dense and fibrous stroma, the PDAC tumor microenvironment is particularly unforgiving, and PDAC tumors undergo extensive metabolic reprogramming.[52] Part of this reprogramming involves the upregulation of cellular processes such as autophagy, which recycles and provides tumor cells with the nutrients and biomolecules necessary for proliferation.[53] Given the role of dCK in salvaging extracellular nucleosides, and the role of autophagy in providing tumor cells with deoxynucleosides for DNA replication, there may be opportunities for dCK inhibition to be utilized in therapy against PDAC.[54] This application is under active study within our research group.

dCK also plays a vital role in the nucleotide metabolism of macrophages and monocytes, which play roles in immune response and activation of pro-inflammatory signaling. These white blood cells can contribute to exuberant immune responses at late stages of infectious disease and lead to cytokine storms, a potentially deadly condition marked by excessive production of inflammatory cytokines which can lead to multi-organ failure and death. Cytokine storms are associated with increased mortality in patients suffering from viral illnesses such as influenza,

and has been documented as a contributing factor to mortality in the ongoing COVID-19 pandemic caused by SARS-CoV-2. Interestingly, macrophages and monocytes lack the capacity to synthesize nucleotides *de novo*, meaning they rely upon dCK and the salvage pathway for biosynthesis of the nucleotides necessary for DNA replication and repair.[55] This reliance upon dCK is heightened upon monocyte and monocyte-derived macrophage activation, as this process leads to production of reactive oxygen species (ROS) which necessitate the function of dCK to repair ROS-mediated DNA damage. Accordingly, dCK inhibition is associated with defects in monocyte/macrophage effector functions, strongly suggesting that dCK inhibitors could be exploited therapeutically to attenuate excessive inflammation causing/caused by cytokine storm.

With demonstrated efficacy against leukemia and potential applications in PDAC therapy and in reducing the impact of cytokine storms, the development, pharmacological characterization, and evaluation of dCK inhibitors is an important area of research. Our lead compound DI-87 possesses low-nM affinity for dCK and is well-tolerated in mice with no observed adverse effects. Thus, preclinical evaluation studies were warranted. Due to technical and kinetic considerations, there were multiple limitations within our preclinical pharmacological profiling studies of DI-87. Because the half-life of the [^{18}F]CFA PET probe did not allow for multiple images within the same animal across a time course experiment, each time point represented a reading from a separate mouse. Additionally, the PET probe required time for optimal diffusion within the tumor; thus we were unable to quantify dCK inhibition at very early time points. PK in the tumor was evaluated in separate mice rather than using a probe to follow drug levels over time. However, this likely does not represent a major limitation, as similar results were obtained between replicate experiments and results between mice were similar at each time point. Given small sample sizes in the PK studies and differing tumor studies between

experiments, it was difficult to determine whether the PK was linear; however, the plasma and tumor PK models fit the data well without evidence of non-linear PK. While a fixed dose of i.p. thymidine was used for growth inhibition in the current study, either an IV or oral RNR inhibitor will be necessary for combination therapy in further clinical development.

Our PET-aided pharmacological profiling of the novel DI-87 provides further evidence of the value of PET probes in assisting with preclinical drug development. By using a probe specific for dCK activity, we were able to accurately and efficiently predict appropriate dosing for growth inhibition studies by determining a DI-87 dose that resulted in maximal dCK inhibition throughout the dosing interval. This also aided in the development of PK-PD models for both dCK inhibition and growth inhibition which can be used to optimize dosing schedules for further preclinical studies. The optimal dosing schedule of 25 mg/kg BID, predicted to completely inhibit dCK, led to near total arrest of tumor growth. Taken together, DI-87 is a potent dCK inhibitor with *in vivo* efficacy that demonstrates promise as a new compound for combination therapy against tumors expressing dCK, with additional potential applications as a single-agent therapy. This promise is further evidenced by its recent Investigational New Drug (IND) approval by the Federal Drug Administration.

While the potency and favorable PK/PD profile of DI-87 remains encouraging, we still sought to make improvements through rational structure-activity relationship studies. Two areas of the molecular scaffold emerged as targets for modification – the substituted phenyl ring of Part A and the methyl stereocenter of Part C. Part A, composed of a substituted phenyl ring in previous dCKi analogs, was identified as being able to accommodate a wide range of substituents while maintaining steady dCK inhibitory ability. By removing substitutions at phenyl positions 2–6 in **NMc-1**, we generated a novel dCK analog which maintained nanomolar affinity for dCK,

providing credence to our hypothesis that this portion of the inhibitor scaffold was amenable to modification. We were encouraged by the potency of racemic and adamantyl-containing **NMc-3**, as its IC_{50} was equal to that of racemic DI-87 against dCK. Previous dCKi analogs had incorporated various phenyl ring substitutions in order to encourage and take advantage of non-covalent interactions within the dCK substrate binding site, to incorporate fluorine atoms for potential PET probe development, and to improve solubility. While the adamantyl group of **NMc-3** does not address concerns regarding solubility or enable PET probe development, it does demonstrate that hydrophobicity and its potential impacts upon cell penetration can promote high dCK affinity and make up for lost non-covalent hydrogen bonding interactions. The 10-fold decrease in activity demonstrated by **NMc-4** when compared with **NMc-3** provided evidence that substantial hydrophobicity may be required to sustain any benefit over loss of hydrogen bonding interactions promoted by substituted phenyl rings. The severe loss of activity seen in **NMc-5** versus other analogs remains puzzling, as the Part A morpholine was incorporated by virtue of the privileged status of morpholine rings within medicinal chemistry and our data indicating that such a substituent may maintain dCK affinity.

With progress towards improved dCK inhibitors through modifications to Part A appearing incremental at best, we sought to explore the incorporation of a *gem*-dimethyl moiety within Part C of the molecular scaffold. We hypothesized that this moiety would optimally fill the small hydrophobic pocket within the dCK substrate binding site which was previously occupied by the chiral methyl group of DI-87. While the initial construction of the key mercapto-tertiary carbon bond proved difficult, conditions were identified in which the tertiary alcohol intermediate **10** (**Scheme 1.3**) could be converted to the desired *gem*-dimethyl containing final product in a telescoped reaction procedure. However, the *gem*-dimethyl **NMc-6** was nearly 30-

fold less potent than its mono-methyl containing analog **NMc-1**, leading us to hypothesize that steric interactions between the *gem*-dimethyl and 5-methyl substituted thiazole were preventing the compound from properly orienting within the substrate binding site of dCK. Compounds **NMc-7–16**, which lacked the 5-position methyl were synthesized, though none were able to recapitulate single-digit nanomolar affinity for dCK. We assessed the origins of this decrease in potency through MD simulations and discovered that the *gem*-dimethyl compounds lacking a methyl in the 5-position of the thiazole preferentially adopted a "gauche" orientation. This orientation resulted in two fewer hydrogen bonding interactions, when compared with the "anti" orientation of DI-87. This loss of key hydrogen bonding contacts between the diaminopyrimidine and amino acids within the dCK substrate binding pocket was determined to be the predominate contributing factor to loss of activity observed in **NMc-7–16**.

While the synthetic campaign failed to substantially improve upon lead compound DI-87, evaluation of our compounds against nucleotide metabolism proteins other than dCK led to the development of a phenotypic screening platform for the identification of novel modulators of pyrimidine nucleotide metabolism. Screening of a small library of dCK-inhibiting compounds developed by our group led to the discovery of **NMc-9** as a putative UCK inhibitor. Such inhibitors have been studied for decades, as UCK plays a critical role in the salvage of extracellular ribonucleosides and its upregulation in certain cancers is associated with poor prognosis and increased disease aggressiveness.[56] As the key kinase of the salvage pathway, which functions alongside the *de novo* pathway, the development of UCK inhibitors has implications for the function of other small molecule drugs and drug candidates such as inhibitors of the key *de novo* pathway enzyme dihydroorotate dehydrogenase (DHODH).[57,58] Such compounds have found varied applications in multiple sclerosis, rheumatoid arthritis,

anticancer, antiviral, and antibacterial indications, but their efficacy can be limited by a functioning salvage pathway mediated by UCK.[59–61] Despite its clinical relevancy, development of viable UCK inhibitors has remained elusive and there are no such compounds used clinically. Taken together, the ability of **NMc-9** to diminish uridine uptake in intact cells and prevent uridine phosphorylation in lysed cell provides evidence that it is directly inhibiting UCK, rather than preventing the transport of uridine into cells.

In summary, we have developed a potent dCK inhibitor with favorable pre-clinical pharmacology data, and have developed models which will inform proper dosing regimens in future clinical studies. We expanded upon this molecular scaffold to address shortcomings in solubility, as well as to generate achiral inhibitors while maintaining low-nanomolar affinity for dCK. While the last two goals were not met, it led to the development of a phenotypic metabolic modifier screening platform which was utilized to identify a novel putative UCK inhibitor, and whose utility is further expounded upon in Chapter 2 of this dissertation.

1.5.1 Methods and Materials

dCK Uptake Assay Performed in Cell Culture

The human cell line CCRF-CEM (C) was purchased from American Type Culture Collection (ATCC) with passage number 2–20 used for all experiments. Cells were seeded at a density of 50,000 cells/ well in Millipore MultiScreen GV 96 well plates. 0.25 μCi of ^{3}H-dC (Moravek Biochemicals) were added to the cells simultaneously with varying concentrations of the dCK inhibitor at a final volume of 100 μL/ well. After 1 hr at 37 °C, cells were washed four times with ice cold phosphate-buffered saline (PBS) using the Millipore Vacuum Manifold. The amount of incorporated probe was measured by scintillation counting with the PerkinElmer Microbeta.

Drugs

Drug stocks were prepared in DMSO or H_2O and diluted fresh in cell culture media for treatments so as to ensure no *in situ* drug degradation occurred between treatments and/or assays.

Cell Proliferation Assay

CEM cells were plated at 1 × 10 cells/well in at 50 μL/well in white opaque 384-well plates and treated as described. Following incubation with increasing concentrations (2 nm-10 μM) of gemcitabine ± 1 μM DI-87 for 72 hr, 50 μL of CellTiter-Glo reagent (Diluted 1:5 in deionized H_2O) was added to each well, plates incubated at room temperature for 5 min and luminescence was measured using a BioTek microplate luminescence reader.

Animals

Animal studies were conducted under the approval of the UCLA Animal Research Committee and were performed in accordance with the guidelines from the Division of Laboratory Animal

Medicine at UCLA. All NOD scid gamma (NSG) mice were purchased from the UCLA Radiation Oncology breeding colony.

Mouse Xenograft Tumor Models and Treatments

Mice had three separate evaluation protocols which included pharmacokinetics, dCK activity, and growth inhibition studies. CEM cells were maintained in 10% FBS in RPMI-1640 and were grown at 37 °C, 20% O_2, and 5% CO_2. CEM tumor xenografts were developed in 8–12 week-old male or female NSG mice by implanting 2×10^6 CEM cells in 100 μL of a 50/50 (vol/vol) mixture of PBS and matrigel (BD Biosciences) for subcutaneous injections in left shoulders (for imaging, PK, and growth inhibition studies). DI-87 (dCKi, in-house production and Sundia Pharmaceuticals) was administered by oral gavage to recipient animals. For oral administration of DI-87, the drug was solubilized in the formulation containing PEG-200: Transcutol: Labrasol: Tween-80 mixed in 5:3:1:1 ratio. For imaging studies, the mice were treated with indicated doses of DI-87 after the tumor size reached 250 mm^3. For growth inhibition and pharmacokinetic studies, treatments were started after the tumors reached 50 mm^3.

Phenotypic screen of dCK inhibitors against pyrimidine nucleotide metabolism

A library of 65 dCK inhibitors developed by our group was arrayed in polypropylene 384-well plates at 200x concentrations covering a 7-point concentration range (corresponding to 1x concentrations: 5 μM, 1.65 μM, 550 nM, 185 nM, 61.5 nM, 20.6 nM, 6.85 nM). 25 μl per well of condition-specific growth media (DNP + NSP (baseline): media +10 μM rU; DNP: media alone; NSP: media +10 μM rU + 1 μM NITD-982) was plated in opaque-white 384-well plates using a BioTek multidrop liquid handler. dCK inhibitors were added by 250 nL pin-tool transfer

(BioMek FX, Beckman-Coulter) and inhibitor/media mixtures were incubated at room temperature for 30 m. 25 μL of a 40,000 cells/mL JURKAT suspension (for 1000 cells / well) was subsequently added to each well. After 72 h, 50 μL of Cell Titer Glo reagent diluted 1:4 in deionized H_2O was added to each well and luminescence was measured using a Wallac plate reader (Perkin Elmer). Each condition was assayed in duplicate (n=2) and % proliferation values were calculated by normalizing experimental wells to plate negative controls and averaging replicate values. Composite pathway selectivity synergy scores for each test compound were defined as the sum of the excess over additivity (% proliferation inhibition observed - % proliferation inhibition expected) between individual protein kinase inhibitor concentrations across the 7-point concentration range. Z factor scores for individual assay plates were calculated using eight positive and eight negative control wells on each plate. All plates gave a Z factor > 0.5.

Cell Titer Glo viability analysis

Cells were plated at $1x10^3$ cells / well at 50 μ1 / well in white opaque 384-well plates and treated as described. Following incubation 50 μ1 of Cell Titer. Glo reagent (Diluted 1:5 in deionized H_2O) was added to each well, plates incubated at room temperature for 5 min and luminescence was measured using a BioTek microplate luminescence reader. Proliferation rate normalized growth inhibition was calculated using the GR metric.

Mass spectrometry

For analysis of stable isotope-labeled metabolite incorporation into newly replicated DNA, JURKAT cells were cultured in glucose-free RPMI media supplemented with 10% dialyzed FBS, 4 mM glutamine, 1 g/L [$^{13}C_6$]glucose, 10 μM [$^{13}C_9$; $^{15}N_2$]rU and treated as indicated.

Genomic DNA was extracted using the Quick-gDNA MiniPrep kit and hydrolyzed to nucleosides using the DNA Degradase Plus kit, following manufacturer-supplied instructions. In the final step of DNA extraction, 50 μL of water was used to elute the DNA into 1.5 mL microcentrifuge tubes. A nuclease solution (5 μL; 10X buffer/DNA Degradase PlusTM/water, 2.5/1/1.5, v/v/v) was added to 20 μL of the eluted genomic DNA in an HPLC injector vial. The samples were incubated overnight at 37 ºC.

Hydrolyzed DNA was diluted 1/1 with solvent A (water/acetonitrile/formic acid, 95/5/0.1, v/v) and analyzed using a modified version of a previously reported method[2,45] in which aliquots of the solution (15 μL) were injected onto a porous graphitic carbon column (Thermo Hypercarb, 100 x 2.1 mm, 5 micron particle size) equilibrated in solvent A and eluted (300 μL/min) with an increasing concentration of solvent B (acetonitrile/water/formic acid, 90/10/0.1). The HPLC timetable, in terms of min/%B, is the following: 0/0, 5/0, 12/20, 15/30, 17/50, 19/50, 20/0, 24/0. The effluent from the column was directed to Agilent Jet Stream connected Agilent 6460 QQQ operating in the positive ion MRM mode. After verification of retention times using authentic standards, the peak areas of the protonated nucleoside/protonated base fragment ion transitions for each of the nucleosides were recorded with instrument manufacturer-supplied software.

Pharmacokinetic Studies of DI-87 in Mice

DI-87 plasma and tumor concentrations were assessed at 1, 3, 6, 9 and 24 hr following oral administration of 10, 25, or 50 mg/kg of DI-87 to female NSG mice with CEM tumors (N = 5 mice per time point). At each time point, a cohort of mice was sacrificed by cervical dislocation; thus, a single plasma and tumor concentration were obtained from each mouse. Blood samples were collected in heparin-EDTA tubes by the retro-orbital technique and spun at 6000×*g* for 15

min prior to collecting the plasma supernatants. All plasma samples were frozen at –20 °C before sample processing. The stock solutions of DI-87 and DI- 82 (internal standard) were prepared by dissolving the appropriate amount of each drug in a known volume of dimethyl sulfoxide (DMSO) to a 10 mM concentration and were stored at –20 °C before use. DI-82 (internal standard) was diluted to 200 nM in methanol to make the internal solution. The calibration standards were prepared by spiking working stock solutions of DI-87 in plasma from untreated mice to give 0.01–10 pmol/μL range. Each 20 μL calibration standard sample was mixed with 60 μL of internal solution (methanol with 200 nM internal standard) and vortexed for 30 s. Following centrifugation at 15,000 × g for 10 min, approximately 60 μL of sample was carefully transferred into HPLC injector vials for LC-MS/MS-MRM analysis. Plasma samples were processed the same way as the calibration standard samples. 20 μL samples were injected onto a reverse phase column, (Thermo Scientific Hypersil GOLD column 3.0 μm; 2.1 × 100 mm) equilibrated in 0.1% water/formic acid, and eluted (200 μL/min) with an increasing concentration of solvent B (acetonitrile/formic acid, 100/0.1, v/v: min/% acetonitrile; 0/0, 5/0, 15/60, 16/100, 19/100, 20/0, and 25/0). The effluent from the column was directed to the Agilent Jet Stream ion source connected to the triple quadrupole mass spectrometer (Agilent 6460) operating in the multiple reaction monitoring (MRM) mode using previously optimized settings. The following drug precursor → fragment ion transitions were used: DI-82 (511 → 369), DI-87(503 → 361). The peak areas for each drug (precursor → fragment ion transitions) at predetermined retention times were recorded using the software supplied by the instrument manufacturer (Agilent MassHunter).[62] The intraday precision based on the coefficient of variation of replicates of the lower limit of quantification (LLOQ) and for quality control (QC) samples are within 15% and the accuracy of LLOQ and QC samples are within 10%.

Tumors were harvested after dissection of mice, weighed, and snap-frozen in liquid nitrogen. PBS containing internal standard (200 μL for 50 mg tumor) was added to the excised tumor and homogenized using a bead beater (BioSpec). The samples were spun down to collect supernatants. The supernatant was further diluted 5 times in PBS (with internal standard), and four parts of methanol (with internal standard) was added and incubated −80 °C overnight to precipitate proteins. The samples were spun at maximum speed (16000 g) at 4 °C, and supernatant collected. Twenty μL samples were injected onto a reverse phase column equilibrated in water 0.1% formic acid for LC-MS/ MS-MRM analysis in positive ion mode as above and compared to calibration standards.

dCK Activity with MicroPET/CT

dCK activity was evaluated following oral administration of 5, 10, or 25 mg/kg of DI-87 to male NSG mice implanted with CEM tumors (N = 4 mice per time point). The NSG mice were anesthetized 3 hr prior to imaging and intravenously administered 740 kBq of [^{18}F]CFA PET probe.[28] Thus, each mouse was representative of a single time point and concentration. MicroPET/CT experiments were conducted using G8 microPET/CT system.[30,63] The mice were then positioned in an imaging chamber and data was acquired with the G8 microPET/CT system (Sofie Biosciences). MicroPET data was acquired for 10 min and reconstructed with a statistical maximum *a posteriori* probability algorithm (MAP) into multiple frames. The spatial resolution of PET is ~1.5 mm with 0.4 mm voxel size. CT images are a low-dose 400 μm resolution acquisition with 200 μm voxel size. MicroPET and CT images were co-registered and then quantified by manually drawing three-dimensional regions of interest using Osirix software. The

color scale was proportional to tissue concentration, with red being the highest and yellow, green and blue corresponding to the lower values.

Growth Inhibition Studies

Male NSG mice implanted with CEM tumors as above were used for growth inhibition studies. Combination therapy of DI-87 with thymidine was used. Treatments of DI-87 and/or thymidine were started after tumor volume reached 50 mm^3. DI-87 was administered at varying doses orally once a day (QD) or twice a day (BID) for 16–18 days while thymidine (2 g/kg) solubilized in saline was administered intraperitoneally BID after start of treatment.[17] Three cohorts of control mice were administered either: (i) intraperitoneal (i.p.) thymidine alone, (ii) Oral DI-87 with i.p saline injections, or (iii) vehicle for oral DI-87 and saline i.p. Tumor growth, as measured by CT, was compared amongst different treatment groups (n = 5 mice, 5 tumors/ group). Tumor growth was monitored daily by caliper measurements ([(length × width2)/2]) and bi-weekly by CT measurements.

Pharmacokinetic and Pharmacodynamic Modeling

Using the computer program NONMEM (version 7.3) with a GNU Fortran G77 Compiler, DI-87 concentration-time data were modeled using first-order conditional estimation (FOCE) method with interaction. Plasma concentrations were assessed with standard PK models which included a depot compartment representing the gut. Tumor concentrations were evaluated with the addition of a separate tumor compartment once plasma concentrations had been characterized (ADVAN6, TRANS1 subroutine). An exponential-normal distribution error model was used for inter-subject variability.

A combined pharmacokinetic-pharmacodynamic (PK-PD) model was developed using the final DI-87 plasma-tumor PK parameter estimates. The effect compartment (dCK inhibition or growth inhibition) was linked to the tumor concentrations. Linear (slope), Emax, and sigmoid Emax models were tested to determine which were the best fits to the data (see equations below).[64] The final model was used to simulate dCK inhibition and growth inhibition from a representative mouse for each of the tested DI-87 concentrations.

PD models:

$$A.\ \ Linear\ (slope):\ \ Slope * Conc.$$

$$B.\ \ E_{max}\text{: } E_{max} * \frac{Conc.}{EC_{50} + Conc}$$

$$C.\ \ Sigmoid\ E_{max}:\ \ E_{max} * \frac{Conc^{Exp}}{EC_{50}^{Exp} + Conc^{Exp}}$$

Docking and Molecular Dynamics:

The inhibitor compounds are docked into the binding pocket of dCK crystal structure manually. Classical molecular dynamics (MD) were performed using the GPU code (pmemd) of the Amber 12 package on the substrate conformations and the transition states for 500 ns in enzyme. The FF99SBildn force field was used for the protein residues. Parameters for the substrate conformations and transition states were generated within the antechamber module using the general Amber force field (gaff), with the partial charges set to fit the electrostatic potential calculated at the HF/6-31G(d) level by the RESP model. The charges were computed according to the Merz-Singh-Kollman scheme using the Gaussian 09 package. Each enzyme complex was immersed in a pre-equilibrated truncated cuboid box with a 10 Å buffer of TIP3P water molecules using the tleap module. The systems were neutralized by addition of explicit counter ions (Na^+ or Cl^-). The systems were optimized for total 10000 steps, followed by gentle heating

from 0 K to 300 K under constant-volume and periodic-boundary conditions. Each system was then equilibrated for 2 ns with a 2 fs time step. Production trajectories were then run for additional 500 ns under the same simulation conditions.

DFT Calculation:

Density functional theory computations were performed using Gaussian09. Geometry optimizations were performed at the B3LYP/6-31G(d) level of theory, which has been shown to yield accurate conformational energetics. The energy is scanned along the dihedral angle with Opt=ModRedundant option. Reported energies are Gibbs free energies. The 3D rendering of stationary points were generated using CYLview. GaussView and Avogadro were used to construct the structures used in our computations.

Statistical analyses

Data are presented as mean ± SD with number of biological replicates indicated. Comparisons of two groups were calculated using indicated unpaired two-tailed Student's t-test and P values less than 0.05 were considered significant. Comparisons of more than two groups were calculated using one-way ANOVA followed by Bonferroni's multiple comparison tests, and P values less than 0.05/m, where m is the total number of possible comparisons, were considered significant.

1.5.2 General Chemistry Methods

All chemicals, reagents and solvents were obtained from commercial sources and were used without further purification. Unless otherwise noted, reactions were carried out in oven-dried glassware under an atmosphere of argon using commercially available anhydrous solvents. Tetrahydrofuran (THF) was distilled from sodium under an argon atmosphere. Dichloromethane was distilled from calcium hydride. Solvents used for extractions and chromatography were not

anhydrous. Analytical TLC was carried out on precoated silica gel (Merck silica gel 60, F254) and visualized with UV light. Column chromatography was performed with silica (Fisher, 230–400 mesh). ^{1}H NMR, ^{13}C NMR, and ^{19}F NMR spectra were measured in $CDCl_3$ or DMSO-d_6 on Bruker AV spectrometers at 400 or 500 MHz. Chemical shifts were reported in parts per million (δ) relative to residual solvent signals. The signals observed were described as follows: s (singlet), d (doublet), t (triplet), q (quartet), dd (doublet of doublets), dt (doublet of triplets), ddd (doublet of doublet of doublets), tt (triplet of triplets), tdd (triplet of doublet of doublets), m (multiplet), br s (broad singlet), br m (broad multiplet). Mass spectra were obtained on a Waters LCT Premier with ACQUITY UPLC mass spectrometer under electrospray ionization (ESI) or Thermo Fisher Scientific Exactive Plus with direct analysis in real time (DART) ionization. All microwave-assisted reactions were carried out in a CEM Discover 908005 Microwave synthesizer system.

1.5.3 General Method A – Synthesis of Thioamide Intermediates

With appropriate carbonitrile starting materials, all thioamide intermediate compounds were synthesized using the following General Method A for synthesis of 4-methoxy-3-(2-morphlinoethoxy)benzothioamide:

To a homogenous solution of 4-methoxy-3-(2-morpholinoethoxy)benzonitrile (1.52 g, 5.79 mmol) in pyridine (12 mL) was added Et_3N (1 mL, 7.17 mmol) and ammonium sulfide solution (20 wt% in water, 5.93 mL, 17.4 mmol). The reaction solution was heated to 60 °C and stirred for 12 hr. The reaction solution was then cooled to room temperature and concentrated *in vacuo*. The resulting residue was taken up in ethyl acetate and washed with deionized water and brine. The organic layer was dried over anhydrous $MgSO_4$, concentrated *in vacuo*, and purified by flash

chromatography over silica gel (1:2 to 2:1 ethyl acetate/hexanes) to yield the desired 4-methoxy-3-(2-morpholinoethoxy)benzothioamide (1.35 g, 79% yield). ^{1}H NMR (300 MHz, $CDCl_3$) δ 7.75 (br s, 1H), 7.65 (d, J = 2.2 Hz, 1H), 7.41 (dd, J = 8.5, 2.2 Hz, 1H), 7.36 (br s, 1H), 6.81 (d, J = 8.5 Hz, 1H), 4.21 (t, J = 5.9 Hz, 2H), 3.88 (s, 3H), 3.72 (t, J = 4.7 Hz, 4H), 2.85 (t, J = 5.9 Hz, 2H), 2.59 (t, J = 4.6 Hz, 4H). DART-MS: m/z calcd. for $C_{14}H_{21}N_2O_3S$ $[M + H]^+$, 297.12729; found 297.12241.

1.5.4 General Method B – Synthesis of 2-substituted 1-(5-methyl-thiazol-4-yl)-ethan-1-one Intermediates

With appropriately substituted thioamide precursors, all 2-substituted 1-(5-methyl-thiazol-4-yl)-ethan-1-one intermediate compounds were synthesized using the following General Method B for synthesis of 1-(2-(4-methoxy-3-(2-morpholinoethoxy)phenyl)-5-methylthiazol-4-yl)ethan-1-one:

To a solution of 4-methoxy-3-(2-morphlinoethoxy)benzothioamide (276 mg, 0.931 mmol) in ethanol (3 mL) at room temperature was added 4-bromopentane-2,3-dione (200 mg, 1.12 mmol) and the reaction solution was heated to reflux for 3 hr. The reaction solution was then concentrated *in vacuo*, and the resulting residue was directly purified by trituration with ethyl acetate and hexanes to yield the desired thiazole (190 mg, 54% yield). ^{1}H NMR (500 MHz, $CDCl_3$) δ 7.50 (d, J = 2.0 Hz, 1H), 7.47 (dd, J = 8.4, 2.1 Hz, 1H), 6.90 (d, J = 8.4 Hz, 1H), 4.66 (t, J = 4.4 Hz, 2H), 4.30 (br m, 2H), 4.02 (br m, 2H), 3.88 (s, 3H), 3.72 (br m, 2H), 3.55 (t, J = 4.3 Hz, 2H), 3.22 (br m, 2H), 2.74 (s, 3H), 2.68 (s, 3H). DART-MS: m/z calcd. for 377.15350 $[M + H]^+$; found 377.15920.

1.5.5 General Method C – Synthesis of 2-substituted ethyl-4-carboxylate Thiazole Intermediates

With appropriately substituted thioamide precursors, all 2-substituted ethyl-4-carboxylate thiazole intermediates were synthesized using the following General Method C for synthesis of ethyl 2-methylthiazole-4-carboxylate:

To a solution of ethanethioamide (230 mg, 3.06 mmol) in ethanol (12 mL) was added ethyl bromopyruvate (0.46 mL, 3.67 mmol). The reaction solution was heated to reflux and stirred for 2 hr. The reaction solution was then diluted with deionized water and extracted three times with ethyl acetate. The combined organic layers were washed with brine, dried over anhydrous $MgSO_4$, and concentrated *in vacuo*. The residue was then purified by flash column chromatography with 35% ethyl acetate in hexanes as the eluent. The product was obtained as a crystalline solid (380 mg, 73% yield). ^{1}H NMR (400 MHz, $CDCl_3$) δ 8.03 (s, 1H), 4.41 (q, J = 7.1 Hz, 2H), 2.76 (s, 3H), 1.40 (t, J = 7.1 Hz, 3H); ^{13}C NMR (100 MHz, $CDCl_3$) δ 166.9, 161.6, 147.0, 127.4, 61.6, 19.5, 14.5; HRMS-ESI (m/z) $[M+H]^+$ calcd for $C_7H_{10}NO_2S$ $[M+H]^+$ 171.03540, found 171.03738.

1.5.6 General Method D – Synthesis of 2-substituted 1-(thiazol-4-yl)-ethan-1-ol Intermediates

With appropriate 2-substituted 1-(5-methyl-thiazol-4-yl)-ethan-1-one precursors, all 2-substituted 1-(thiazol-4-yl)-ethan-1-ol thiazole intermediates were synthesized using the following General Method D for synthesis of 1-(5-methyl-propylthiazol-4-yl)-ethan-1-ol:

To a homogenous solution of 1-(5-methyl-propylthiazol-4-yl)-ethan-1-one (407 mg, 2.22 mmol) in THF at 0 °C was added DIBAL-H (1.0 M solution in THF, 3.11 mL, 3.11 mmol) dropwise.

The reaction solution was stirred at 0 °C for 15 min and then at room temperature for 75 min. Upon reaction completion, the solution was then cooled to 0 °C and carefully quenched by addition of Rochelle's Salt. This mixture was stirred for 30 min, diluted with deionized water, and extracted three times with ethyl acetate. The organic layers were then combined and dried over anhydrous $MgSO_4$ and concentrated *in vacuo*. The resulting oil was purified by flash column chromatography over silica gel with 10% ethyl acetate in hexanes as the eluent. The desired alcohol was obtained as an oil (468 mg, 98% yield). ^{1}H NMR (400 MHz, $CDCl_3$) δ 4.88 (m, 1H), 2.87 (d, J = 15.3 Hz, 1H), 2.85 (d, J = 15.3 Hz, 1H), 2.77 (br s, 1H), 2.35 (s, 3H), 1.75 (m, 2H), 1.48 (d, J = 6.5 Hz, 3H), 0.99 (t, J = 7.4 Hz, 3H); ^{13}C NMR (100 MHz, $CDCl_3$) δ 168.1, 153.8, 125.5, 64.6, 35.4, 24.2, 23.5, 13.8, 10.9; HRMS-ESI (m/z) $[M+H]^+$ calcd for $C_9H_{16}NOS$ 186.09526, found 186.09952.

1.5.7 General Method E – Synthesis of 2-substituted 2-(thiazol-4-yl)-propan-2-ol Intermediates

With appropriate 2-substituted ethyl-4-carboxylate substituted thiazole precursors, all 2-substituted 2-(thiazol-4-yl)-propan-2-ol intermediates were synthesized using the following General Method E for synthesis of 2-(2-phenylthiazol-4-yl)propan-2-ol:

To a solution of ethyl 2-phenylthiazole-4-carboxylate (740 mg, 3.17 mmol) in THF (20 mL) at 0 °C was added methyl magnesium bromide (3.0 M in THF, 4.2 mL, 12.7 mmol). The reaction solution was stirred for 30 min before warming to room temperature. Once the starting material was consumed, the reaction solution was quenched by carefully pouring into a saturated NH_4Cl solution. The aqueous solution was extracted three times with ethyl acetate and the combined

organic layers were dried over $MgSO_4$, concentrated *in vacuo*, and resulting residue was purified by flash column chromatography over silica gel using 15 % ethyl acetate in hexanes as the eluent. Desired alcohol obtained as an off-white solid (536 mg, 77% yield). ^1H NMR (400 MHz, $CDCl_3$) δ 7.95 (m, 2H), 7.42 (m, 3H), 7.08 (s, 1H), 3.04 (br s, 1H), 1.65 (s, 6H); ^{13}C NMR (100 MHz, $CDCl_3$) δ 168.0, 165.0, 133.7, 130.1, 129.0, 126.7, 111.3, 71.3, 30.2; HRMS-ESI (*m/z*) $[M+H]^+$ calcd for $C_{12}H_{14}NOS$ 220.07961, found 220.08266.

1.5.8 General Method F – Synthesis of 2-substituted 1-(5-methyl-thiazol-4-yl)-ethyl 2,2,2-trifluoroacetate Intermediates

With appropriate 2-substituted 1-(thiazol-4-yl)-ethan-1-ol precursors, all 2-substituted 1-(5-methyl-thiazol-4-yl)-ethyl 2,2,2-trifluoroacetate intermediates were synthesized using the following General Method F for the synthesis of (*S*)-1-(2-(4-methoxy-3-(2-morpholinoethoxy)phenyl)-5- methylthiazol-4-yl)ethyl 2,2,2-trifluoroacetate:

To a solution of (S)-1-(2-(4-methoxy-3-(2-morpholinoethoxy)phenyl)-5- methylthiazol-4-yl)ethan-1-ol (47 mg, 0.124 mmol) in DCM (5 mL) at 0 °C was added trifluoroacetic anhydride (TFAA, 0.07 mL, 0.5 mmol) dropwise. After stirring for 30 min at 0 °C the reaction solution was warmed to room temperature prior to quenching with a saturated aqueous solution of sodium bicarbonate. The resulting aqueous solution was extracted with DCM three times, the combined organic layers washed with brine, concentrated *in vacuo* and used directly in next step due to the instability of the trifluoroacetate product. HRMS-ESI (*m/z*) calcd for $C_{21}H_{26}F_3N_2O_5S$ $[M+H]^+$ 475.15145, found 475.15481.

1.5.9 General Method G – Synthesis of 2-substituted 2-(1-(5-methyl-thiazol-4-yl)-ethyl) thiopyrimidine-4,6-diamine Final NMc Compounds (NMc 1–4)

With appropriate 2-substituted 1-(5-methyl-thiazol-4-yl)-ethyl 2,2,2-trifluoroacetate precursors, final NMc compounds 1–4 were synthesized using the following General Method E for synthesis of (*R*)-2-((1-(2-(4-methoxy-3-(2-morpholinoethoxy)-phenyl)-5-methylthiazol-4-yl)ethyl)thio)pyrimidine-4,6-diamine (DI-87):

To a solution of crude (*S*)-1-(2-(4-methoxy-3-(2-morpholinoethoxy)phenyl)-5-methylthiazol-4-yl)ethyl 2,2,2-trifluoroacetate (71 mg, 0.15 mmol) and Cs_2CO_3 (195 mg, 0.60 mmol) from the previous step in DMF (3 mL) was added 4,6-diamino-2-mercaptopyrimidine (43 mg, 0.30 mmol) and the reaction solution was stirred at 80 °C. After 3 hr, the reaction solution was filtered through a pad of Celite, concentrated *in vacuo*, and purified by flash chromatography over silica gel (1:20 to 1:10 methanol/DCM). Final product obtained as a pale brown solid (20 mg, 27% yield (two steps)). ^{1}H NMR (400 MHz, $CDCl_3$) δ 7.54 (d, J = 2.0 Hz, 1H), 7.37 (dd, J = 8.4, 2.0 Hz, 1H), 6.86 (d, J = 8.4, 1H), 5.24 (s, 1H), 5.22 (q, J = 7.0 Hz, 1H), 4.60 (s, 4H), 4.24 (t, J = 5.9 Hz, 2H), 3.88 (s, 3H), 3.76 (t, J = 4.7 Hz, 4H), 2.87 (t, J = 5.9 Hz, 2H), 2.61, (t, J = 4.5 Hz, 4H), 2.50 (s, 3H), 1.80 (d, J = 7.0 Hz, 3H); ^{13}C NMR (100 MHz, $CDCl_3$) δ 170.5, 163.8, 163.3, 153.5, 150.8, 148.4, 127.4, 126.9, 119.9, 111.6, 111.3, 80.7, 67.0, 66.7, 57.6, 56.1, 54.2, 37.7, 22.1, 11.7; HRMS-ESI (*m*/*z*) calcd for $C_{23}H_{31}N_6O_3S_2$ $[M+H]^+$ 503.18991, found 503.18727.

1.5.10 General Method H – Synthesis of 2-substituted 4-(2-chloropropan-2-yl) Thiazole Intermediates

With appropriate 2-substituted 2-(thiazol-4-yl)-propan-2-ol precursors, all 2-substituted 4-(2-chloropropan-2-yl) intermediates were synthesized using the following General Method H for synthesis of 4-(2-chloropropan-2-yl)-2-phenylthiazole:

To a heterogenous solution of 2-(2-phenylthiazol-4-yl)propan-2-ol (214 mg, 0.976 mmol) and sodium bicarbonate (517 mg, 4.88 mmol) in diethyl ether (5 mL) was added thionyl chloride (0.078 mL, 1.07 mmol). The reaction solution was stirred for 15 min, filtered through a pad of Celite and concentrated *in vacuo* at low temperature. The crude product was used directly in the following step due to instability of the tertiary chloride. HRMS-ESI (*m*/*z*) calcd for $C_{12}H_{13}ClNS$ $[M+H]^+$ 238.04572, found 238.04814.

1.5.11 General Method I – Synthesis of 2-substituted 2-((2-(thiazol-4-yl)propan-2-yl)thio)pyrimidine-4,6-diamine Final NMc Compounds (NMc 5–16)

With appropriate 2-substituted 4-(2-chloropropan-2-yl) precursors, all final *gem*-dimethyl NMc compounds 5–16 were synthesized using the following General Method I for synthesis of 2-((2-(2-phenylthiazol-4-yl)propan-2-yl)thio)pyrimidine-4,6-diamine (NMc-7):

To a solution of crude 4-(2-chloropropan-2-yl)-2-phenylthiazole (0.638 mmol) in DMF was added sodium 4,6-diaminopyrimidine-2-thiolate (105 mg, 0.638 mmol) and the resulting solution was stirred at room temperature for 3 hr. The reaction solution was then filtered through Celite, concentrated *in vacuo* and purified by flash column chromatography using an eluent gradient of 3–5% methanol in DCM. Product obtained as an off-white solid (22 mg, 10% yield). ^{1}H NMR (400 MHz, $CDCl_3$) δ 7.94 (m, 2H), 7.40 (m, 3H), 7.22 (s, 1H), 5.16 (s, 1H), 4.58 (br s, 4H), 2.02

(s, 6H); ^{13}C NMR (100 MHz, $CDCl_3$) δ 170.1, 166.4, 162.8, 152.9, 134.2, 129.8, 128.9, 126.7, 114.2, 80.9, 50.4, 29.2;

1.6 Experimental Details

4-Methoxy-3-(2-morpholinoethoxy)benzonitrile (I1)

To a heterogeneous solution of 4-methoxy-3-hydroxybenzonitrile (2.44 g, 16.4 mmol) and Cs_2CO_3 (10.68 g, 32.8 mmol) in *N*,*N*-dimethylformamide (DMF) and acetone (1:1, 60 mL) was added 4-(2-chloroethyl)morpholine hydrochloride (2.45 g, 16.4 mmol). The reaction solution was stirred under argon at 70 °C for 12 hr. The reaction solution was then filtered and the filtrate diluted with deionized water before extracting three times with ethyl acetate. The combined organic layers were dried over anhydrous $MgSO_4$ and concentrated *in vacuo* before purification by flash chromatography over silica gel (2:3 ethyl acetate/ hexanes) to yield the desired product **I1** (3.91 g, 91% yield).

^{1}H NMR (500 MHz, $CDCl_3$) δ:

7.29 (dd, *J* = 8.4, 1.9 Hz, 1H)

7.13 (d, *J* = 1.9 Hz, 1H)

6.91 (d, *J* = 8.4 Hz, 1H)

4.16 (t, *J* = 5.9 Hz, 2H)

3.91 (s, 3H)

3.73 (t, *J* = 4.7 Hz, 4H)

2.85 (t, *J* = 5.9 Hz, 2H)

2.59 (t, *J* = 4.6 Hz, 4H).

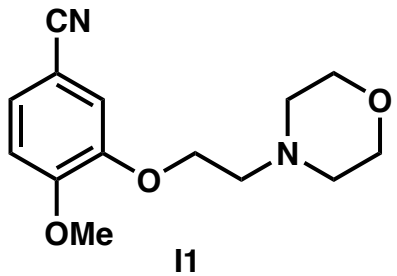

I1

HRMS-ESI (*m*/*z*) calcd for $C_{14}H_{19}N_2O_3$ $[M+H]^+$ 263.13957, found 263.14203.

4-Methoxy-3-(2-morpholinoethoxy)benzothioamide (I2)

I2 was synthesized according to General Method A starting from precursor **I1**. 1.35 g, 79% yield.

^{1}H NMR (300 MHz, $CDCl_3$) δ:

7.75 (br s, 1H)

7.65 (d, J = 2.2 Hz, 1H)

7.41 (dd, J = 8.5, 2.2 Hz, 1H)

7.36 (br s, 1H)

6.81 (d, J = 8.5 Hz, 1H)

4.21 (t, J = 5.9 Hz, 2H)

3.88 (s, 3H)

3.72 (t, J = 4.7 Hz, 4H)

2.85 (t, J = 5.9 Hz, 2H)

2.59 (t, J = 4.6 Hz, 4H).

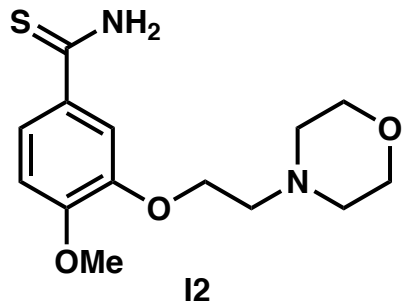

I2

DART-MS: m/z calcd. for $C_{14}H_{21}N_2O_3S$ $[M + H]^+$ 297.12729; found 297.12241.

1-(2-(4-Methoxy-3-(2-morpholinoethoxy)phenyl)-5- methylthiazol-4-yl)ethan-1-one (I3)

I3 was synthesized according to General Method B starting from precursor **I2**. (90 mg, 54% yield.

^{1}H NMR (500 MHz, $CDCl_3$) δ:

7.50 (d, J = 2.0 Hz, 1H)

7.47 (dd, J = 8.4, 2.1 Hz, 1H)

6.90 (d, J = 8.4 Hz, 1H)

4.66 (t, J = 4.4 Hz, 2H)

4.30 (br m, 2H)

4.02 (br m, 2H)

3.88 (s, 3H)

3.72 (br m, 2H)

3.55 (t, J = 4.3 Hz, 2H)

3.22 (br m, 2H)

2.74 (s, 3H)

2.68 (s, 3H).

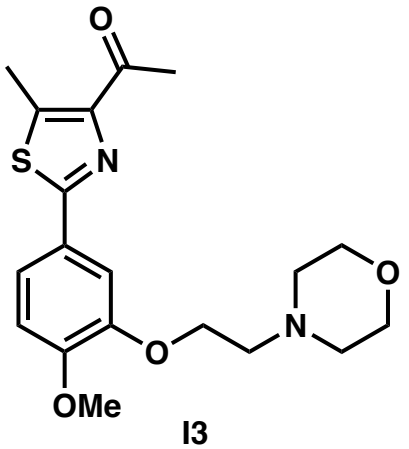

I3

DART-MS: m/z calcd. for $C_{19}H_{25}N_2O_4S$ $[M + H]^+$ 377.15350; found 377.15920.

(*S*)-1-(2-(4-Methoxy-3-(2-morpholinoethoxy)phenyl)-5-methylthiazol-4-yl)ethan-1-ol (I4)

To a solution of (*R*)-(+)-2-methyl-CBS-oxazaborolidine (3.0 mL of a 1.0 M solution in toluene, 3.0 mmol) in THF (13 mL) at −78 °C was added borane–THF complex (4.4 mL of a 1.0 M solution in THF, 4.4 mmol) followed by a solution of **3** (125 mg, 0.332 mmol) in THF (7 mL) by syringe pump over 6 hr while stirring at −78 °C. Upon completion of addition by syringe pump, the reaction solution was stirred for another 20 min before addition of DI water (10 mL) and methanol (5 mL) and warming to room temperature. The aqueous solution was extracted with ethyl acetate, and the resulting organic layer was dried over anhydrous $MgSO_4$ and concentrated *in vacuo*. The resulting residue was purified by flash chromatography over silica gel (1:20 to 1:10 methanol/DCM) to yield the desired alcohol **14** (50 mg, 40% yield).

^{1}H NMR (500 MHz, $CDCl_3$) δ:

7.49 (d, J = 2.1 Hz, 1H)

7.39 (dd, J = 8.4, 2.1 Hz, 1H)

6.86 (d, *J* = 8.4 Hz, 1H)

4.93 (q, *J* = 6.4 Hz, 1H)

4.22 (t, *J* = 6.1 Hz, 2H)

3.88 (s, 3H)

3.74(t, *J* = 4.7 Hz, 4H)

2.86(t, *J* = 6.1 Hz, 2H)

2.60(t, *J* = 4.5 Hz, 4H)

2.40 (s, 3H)

1.53 (d, *J* = 6.5 Hz, 3H).

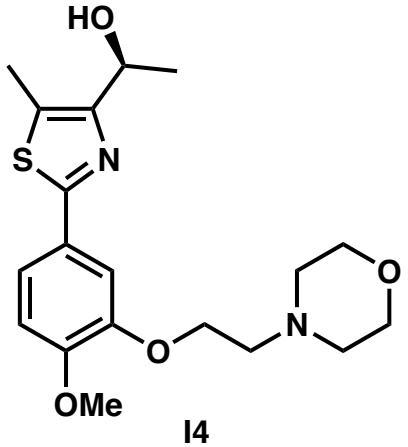

I4

DART-MS: *m/z* calcd. for $C_{19}H_{27}N_2O_4S$ $[M + H]^+$ 379.16915, found 379.17384.

(*S*)-1-(2-(4-Methoxy-3-(2-morpholinoethoxy)phenyl)-5- methylthiazol-4-yl)ethyl 2,2,2-trifluoroacetate (I5)

I5 was synthesized according to General Method F starting from precursor **I4**.

^{1}H NMR (500 MHz, $CDCl_3$) δ:

7.50 (d, *J* = 1.9 Hz, 1H)

7.48 (dd, *J* = 8.4, 1.8 Hz, 1H)

6.91 (d, *J* = 8.4 Hz, 1H)

6.16 (q, *J* = 6.6 Hz, 1H)

4.48 (t, *J* = 4.4 Hz, 2H)

4.01 (t, *J* = 4.7 Hz, 4H)

3.88 (s, 3H)

3.51 (t, *J* = 4.2 Hz, 2H)

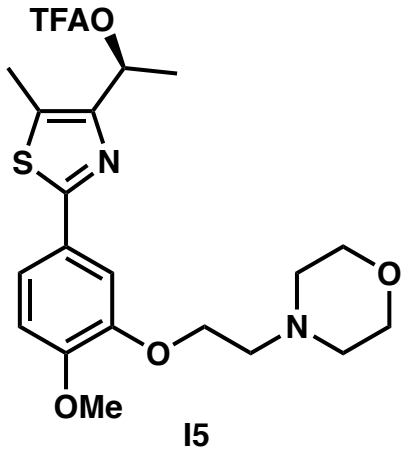

I5

3.41 (br m, 4H)

2.52 (s, 3H)

1.81 (d, J = 6.6 Hz, 3H).

HRMS-ESI (m/z) calcd for $C_{21}H_{26}F_3N_2O_5S$ $[M+H]^+$ 475.15145, found 475.15481.

(*R*)-2-((1-(2-(4-Methoxy-3-(2-morpholinoethoxy) phenyl)-5-methylthiazol-4-yl)ethyl)thio)pyrimidine-4,6-diamine (DI-87)

DI-87 was synthesized according to General Method G starting from precursor **I5**. 20 mg, 27% yield (two steps).

^{1}H NMR (400 MHz, $CDCl_3$) δ:

7.54 (d, J = 2.0 Hz, 1H)

7.37 (dd, J = 8.4, 2.0 Hz, 1H)

6.86 (d, J = 8.4, 1H)

5.24 (s, 1H)

5.22 (q, J = 7.0 Hz, 1H)

4.60 (s, 4H)

4.24 (t, J = 5.9 Hz, 2H)

3.88 (s, 3H)

3.76 (t, J = 4.7 Hz, 4H)

2.87 (t, J = 5.9 Hz, 2H)

2.61, (t, J = 4.5 Hz, 4H)

2.50 (s, 3H)

1.80 (d, J = 7.0 Hz, 3H).

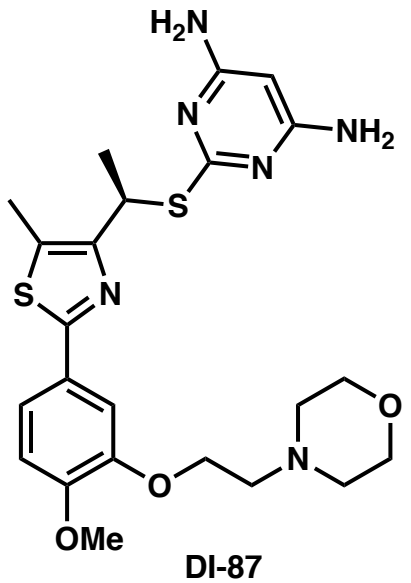

DI-87

^{13}C NMR (100 MHz, $CDCl_3$) δ 170.5, 163.8, 163.3, 153.5, 150.8, 148.4, 127.4, 126.9, 119.9, 111.6, 111.3, 80.7, 67.0, 66.7, 57.6, 56.1, 54.2, 37.7, 22.1, 11.7.

HRMS-ESI (*m/z*) calcd for $C_{23}H_{31}N_6O_3S_2$ $[M+H]^+$ 503.18991, found 503.18727.

1-(5-Methyl-2-phenylthiazol-4-yl)ethan-1-one (I6)

I6 was synthesized according to General Method B starting from benzothioamide (2.804 g, 53% yield).

^{1}H NMR (400 MHz, $CDCl_3$) δ:

7.91 (m, 2H)

7.44 (m, 3H)

2.80 (s, 3H)

2.72 (s, 3H).

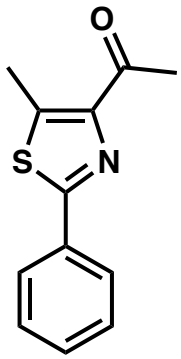

I6

^{13}C NMR (100 MHz, $CDCl_3$) δ 196.0, 162.6, 149.2, 143.7, 133.3, 130.3, 129.1, 126.5, 29.5, 13.6.

HRMS-ESI (*m/z*) calcd for $C_{12}H_{12}NOS$ $[M+H]^+$ 218.06396, found 218.06825.

1-(5-Methyl-2-phenylthiazol-4-yl)ethan-1-ol (I7)

I7 was synthesized according to General Method D starting from precursor **I6**. 350 mg, 99% yield.

^{1}H NMR (400 MHz, $CDCl_3$) δ:

7.90 (m, 2H)

7.41 (m, 3H)

4.96 (q, J = 6.5 Hz, 1H)

3.03 (br s, 1H)

2.44 (s, 3H)

1.56 (d, J = 6.5 Hz, 3H).

HRMS-ESI (m/z) calcd for $C_{12}H_{12}NOS$ $[M+H]^+$ 220.07961, found 220.08247.

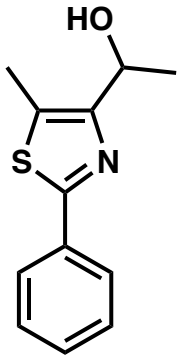

I7

1-(5-Methyl-2-phenylthiazol-4-yl)ethyl 2,2,2-trifluoroacetate (I8)

I8 was synthesized according to General Method F starting from precursor **I7** and taken directly to the next step due to the instability of the trifluoroacetate.

HRMS-ESI (m/z) calcd for $C_{14}H_{13}F_3NO_2S$ $[M+H]^+$ 316.06191, found 316.06092.

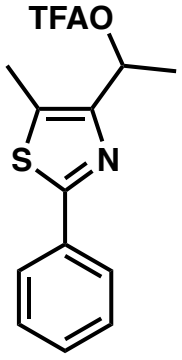

I8

2-((1-(5-Methyl-2-phenylthiazol-4-yl)ethyl)thio)pyrimidine-4,6-diamine (NMc-1)

NMc-1 was synthesized according to General Method G starting from precursor **I8**. 22 mg, 67% yield.

^{1}H NMR (400 MHz, DMSO-d_6) δ:

7.85 (m, 2H)

7.47 (m, 3H)

6.11 (br s, 4H)

5.24 (q, J = 7.0 Hz, 1H)

5.16 (s, 1H)

2.50 (s, 3H)

1.70 (d, J = 7.0 Hz, 3H).

^{13}C NMR (100 MHz, DMSO-d_6) δ 168.0, 163.5, 162.9, 154.1, 133.1, 129.8, 129.2, 127.6, 125.7, 79.1, 36.1, 22.2, 11.2.

HRMS-ESI (m/z) calcd for $C_{16}H_{18}N_5S_2$ $[M+H]^+$ 344.10036, found 344.10087.

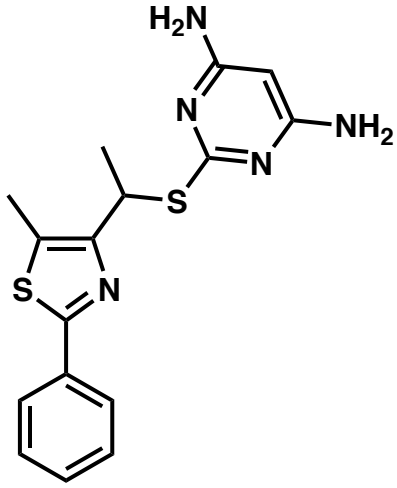

NMc-1

Pyridine-2-carbothioamide (I9)

To a homogenous solution of 2-pyridinecarbonitrile (500 mg, 4.8 mmol) in methanol (48 mL) was added ammonium sulfide (20% aqueous solution, 1.72 mL, 5.04 mmol) and the resulting reaction solution was stirred at room temperature for 18 hr. Reaction solution was then concentrated *in vacuo* to a yellow solid which was taken up in a mixture of ethyl acetate and deionized water. This solution was extracted three times with ethyl acetate. The combined organic layers were washed with brine, dried over anhydrous Na_2SO_4, and concentrated *in vacuo* to give a **I9** as a fine yellow powder (545 mg, 82% yield).

^{1}H NMR (400 MHz, $CDCl_3$) δ:

9.52 (br s, 1H)

8.70 (dt, J = 8.0, 1.0 Hz, 1H)

8.52 (ddd, J = 4.7, 1.7, 0.9 Hz, 1H)

7.84 (ddd, J = 7.8, 7.8, 1.7 Hz, 1H)

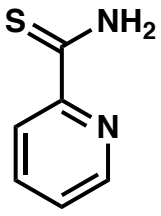

I9

7.79 (br s, 1H)

7.45 (ddd, J = 7.6, 4.7, 1.2 Hz)

^{13}C NMR (100 MHz, $CDCl_3$) δ 195.9, 150.5, 147.2, 137.2, 126.4, 125.1.

HRMS-ESI (m/z) calcd for $C_6H_7N_2S$ $[M+H]^+$ 139.03299, found 139.03345.

1-(5-Methyl-2-(pyridin-2-yl)thiazol-4-yl)ethan-1-one (I10)

I10 was synthesized according to General Method B starting from precursor **I9**. 225 mg, 49% yield.

^{1}H NMR (400 MHz, $CDCl_3$) δ:

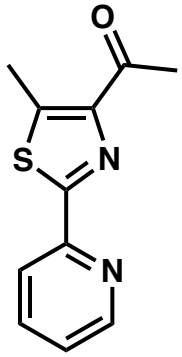

I10

8.59 (ddd, J = 4.9, 1.7, 0.9 Hz, 1H)

8.19 (dt, J = 7.9, 1.1 Hz, 1H)

7.80 (ddd, J = 7.7, 7.7, 1.7 Hz, 1H)

7.33 (ddd, J = 7.5, 4.9, 1.2 Hz, 1H)

2.82 (s, 3H)

2.72 (s, 3H).

^{13}C NMR (100 MHz, $CDCl_3$) δ 195.9, 163.5, 151.2, 149.59, 149.55, 146.2, 137.2, 124.7, 119.6, 29.3, 13.9.

HRMS-ESI (m/z) calcd for $C_{11}H_{11}N_2OS$ $[M+H]^+$ 219.05921, found 219.06183.

1-(5-Methyl-2-(pyridin-2-yl)thiazol-4-yl)ethan-1-ol (I11)

I11 was synthesized according to General Method D starting from precursor **I10**. The crude product taken directly to the next step following confirmation by mass spectrometry.

HRMS-ESI (*m*/*z*) calcd for $C_{11}H_{13}N_2OS$ $[M+H]^+$ 221.07486, found 221.06937.

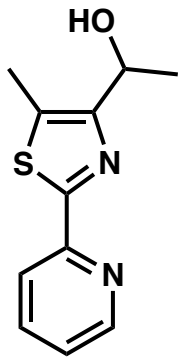

I11

1-(5-Methyl-2-(pyridin-2-yl)thiazol-4-yl)ethyl 2,2,2-trifluoroacetate (I12)

I12 was synthesized according to General Method F using precursor **I11**.

^{1}H NMR (400 MHz, $CDCl_3$) δ:

8.58 (ddd, *J* = 4.9, 1.7, 0.9 Hz, 1H)

8.18 (dt, *J* = 7.9, 1.0 Hz, 1H)

7.78 (ddd, *J* = 7.6, 7.6, 1.7 Hz, 1H)

7.29 (ddd, *J* = 7.5, 4.9, 1.2 Hz, 1H)

6.19 (q, *J* = 6.6 Hz, 1H)

2.56 (s, 3H)

1.82 (d, *J* = 6.6 Hz, 3H).

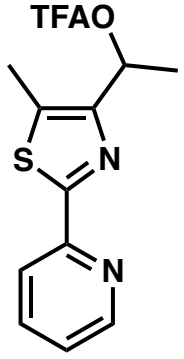

I12

HRMS-ESI (*m*/*z*) calcd for $C_{13}H_{12}F_3N_2O_2S$ $[M+H]^+$ 317.05716, found 317.05442.

2-((1-(5-Methyl-2-(pyridin-2-yl)thiazol-4-yl)ethyl)thio)pyrimidine-4,6-diamine (NMc-2)

NMc-2 was synthesized according to General Method G using precursor **I12**. 157 mg, 48% yield.

^{1}H NMR (400 MHz, DMSO-d_6) δ:

8.59 (ddd, J = 4.8, 1.7, 0.9 Hz, 1H)

8.08 (dt, J = 7.9, 1.0 Hz, 1H)

7.93 (ddd, J = 7.6, 7.6, 1.7 Hz, 1H)

7.45 (ddd, J = 7.5, 4.8, 1.2 Hz, 1H)

6.11 (br s, 4H)

5.25 (q, J = 7.0 Hz, 1H)

5.16 (s, 1H)

2.51 (s, 3H)

1.71 (d, J = 7.0 Hz, 3H).

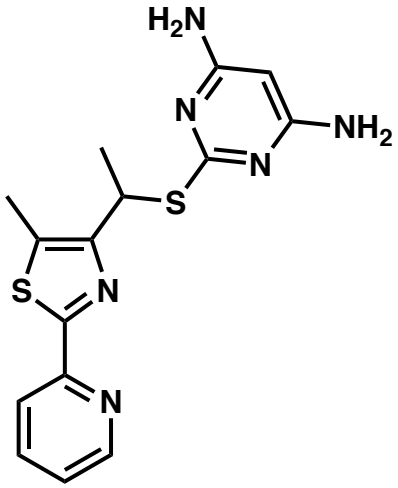

NMc-2

^{13}C NMR (100 MHz, $CDCl_3$) δ 168.0, 164.1, 163.5, 154.6, 150.6, 149.6, 137.6, 130.1, 124.7, 118.7, 79.1, 36.1, 22.1, 11.4.

HRMS-ESI (m/z) calcd for $C_{15}H_{17}N_6S_2$ $[M+H]^+$ 345.09561, found 345.09283.

Adamantane-1-carbothioamide (I13)

I13 was synthesized according to General Method A from 1-adamantanecarbonitrile. 2.3 g, 89% yield.

^{1}H NMR (400 MHz, $CDCl_3$) δ:

7.63 (br s, 1H)

7.02 (br s, 1H)

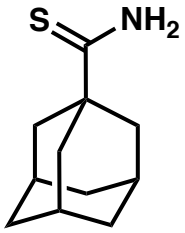

I13

2.09 (m, 3H)

1.97 (m, 6H)

1.73 (m, 6H).

HRMS-ESI (*m/z*) calcd for $C_{11}H_{18}NS$ $[M+H]^+$ 196.11600, found 196.11483.

1-(2-(Adamantan-1-yl)-5-methylthiazol-4-yl)ethan-1-one (I14)

I14 was synthesized according to General Method B from precursor **I13**. 1.25g, 72% yield.

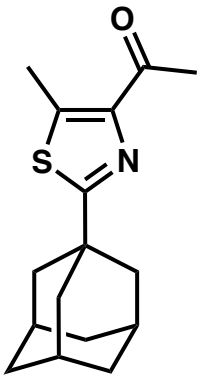

I14

^1H NMR (400 MHz, $CDCl_3$) δ:

2.72 (s, 3H)

2.63 (s, 3H)

2.10 (m, 3H)

2.02 (m, 6H)

1.78 (m, 6H).

HRMS-ESI (*m/z*) calcd for $C_{16}H_{22}NOS$ $[M+H]^+$ 276.14221, found 276.13983.

1-(2-(Adamantan-1-yl)-5-methylthiazol-4-yl)ethan-1-ol (I15)

I15 was synthesized according to General Method D using precursor **I14**, though after aqueous workup crude product was taken on to next step without further purification. 878 mg, 70% crude yield.

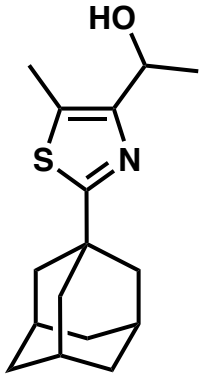

I15

HRMS-ESI (*m/z*) calcd for $C_{16}H_{24}NOS$ $[M+H]^+$ 278.15786, found 278.15835.

1-(2-(Adamantan-1-yl)-5-methylthiazol-4-yl)ethyl 2,2,2-trifluoroacetate (I16)

I16 was synthesized according to General Method F from crude **I15**. 1.066g, 92% crude yield.

^{1}H NMR (400 MHz, $CDCl_3$) δ:

6.11 (q, J = 6.6 Hz, 1H)

2.44 (s, 3H)

2.08 (m, 3H)

2.00 (m, 6H)

1.77 (m, 6H)

1.74 (d, J = 6.6 Hz, 3H).

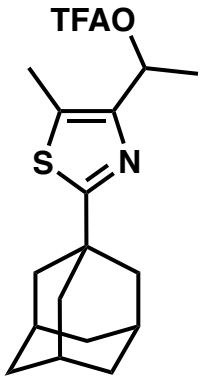

I16

^{13}C NMR (100 MHz, $CDCl_3$) δ 178.2, 157.4, 146.8, 130.2, 113.3, 71.7, 43.2, 39.5, 36.7, 28.7, 19.7, 11.1.

2-((1-(2-Adamantan-1-yl)-5-methylthiazol-4-yl)ethyl)thio)pyrimidine-4,6-diamine (NMc-3)

NMc-3 was synthesized according to General Method G. 580 mg, 52% yield.

^{1}H NMR (400 MHz, $CDCl_3$) δ:

5.23 (s, 1H)

5.18 (q, J = 6.9 Hz, 1H)

4.56 (br s, 4H)

2.44 (s, 3H)

2.06 (m, 3H)

2.00 (m, 6H)

1.75 (m, 6H)

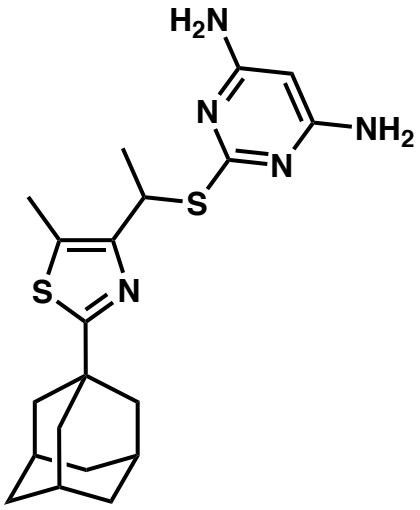

NMc-3

1.74 (d, J = 7.0 Hz, 3H).

^{13}C NMR (100 MHz, $CDCl_3$) δ 177.0, 171.1, 163.3, 151.5, 125.1, 80.7, 43.2, 39.4, 38.1, 36.8, 28.8, 22.2, 11.6.

HRMS-ESI (m/z) calcd for $C_{20}H_{28}N_5S_2$ $[M+H]^+$ 402.17861, found 402.17482.

Butanethioamide (I17)

I17 was synthesized according to General Method A. 844 mg, 36% yield.

^{1}H NMR (400 MHz, $CDCl_3$) δ:

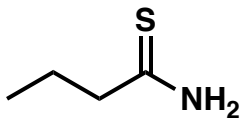

I17

7.55 (br s, 1H)

6.84 (br s, 1H)

2.63 (t, J = 7.5 Hz, 2H)

1.81 (tq, J = 7.5, 7.4 Hz, 2H)

0.99 (t, J = 7.4 Hz, 3H).

^{13}C NMR (100 MHz, $CDCl_3$) δ 211.2, 47.5, 22.7, 13.5.

HRMS-ESI (m/z) calcd for $C_4H_{10}NS$ $[M+H]^+$ 104.05340, found 104.05300.

1-(5-Methyl-2-propylthiazol-4-yl)ethan-1-one (I18)

I18 was synthesized according to General Method B with precursor **I17**. 1.075g, 66% yield.

^{1}H NMR (400 MHz, $CDCl_3$) δ:

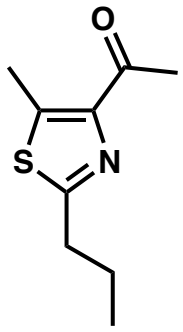

I18

2.87 (t, J = 7.7 Hz, 2H)

2.69 (s, 3H)

2.61 (s, 3H)

1.77 (tq, J = 7.5, 7.5 Hz, 2H)

1.00 (t, J = 7.4 Hz, 3H).

^{13}C NMR (100 MHz, $CDCl_3$) δ 195.8, 166.0, 148.0, 143.1, 35.3, 29.5, 23.3, 13.7, 13.4.

1-(5-Methyl-2-propylthiazol-4-yl)ethan-1-ol (I19)

I19 was synthesized according to General Procedure D with precursor **I18**. 491 mg, 68% yield.

^{1}H NMR (400 MHz, $CDCl_3$) δ:

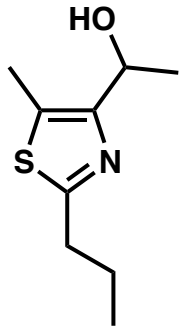

I19

4.88 (m, 1H)

2.86 (t, J = 7.6 Hz, 2H)

2.77 (br s, 1H)

2.35 (s, 3H)

1.75 (tq, J = 7.5, 7.5 Hz, 2H)

1.48 (d, J = 6.5 Hz, 3H)

0.99 (t, J = 7.4 Hz, 3H).

^{13}C NMR (100 MHz, $CDCl_3$) δ 168.1, 153.8, 125.5, 64.6, 35.4, 24.2, 23.5, 13.8, 10.9.

1-(5-Methyl-2-propylthiazol-4-yl)ethyl 2,2,2-trifluoroacetate (I20)

I20 was synthesized according to General Method F starting from precursor **I19**. 703 mg, 94% crude yield. The product was taken directly to next step due to the instability of the trifluoroacetate.

HRMS-ESI (m/z) calcd for $C_{11}H_{15}F_3NO_2S$ $[M+H]^+$ 282.07756, found 282.07472.

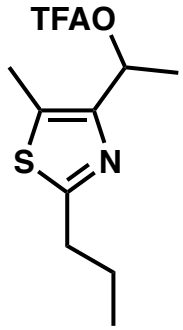

I20

2-((1-(5-Methyl-2-propylthiazol-4-yl)ethyl)thio)pyrimidine-4,6-diamine (NMc-4)

NMc-4 was synthesized according to General Method G from precursor **I20**. 204 mg, 25% yield.

^{1}H NMR (400 MHz, DMSO-d_6) δ:

6.09 (br s, 4H)

5.14 (q, J = 7.0 Hz, 1H)

5.14 (s, 1H)

2.82 (t, J = 7.5 Hz, 2H)

2.39 (s, 3H)

1.67 (sext, J = 7.4 Hz, 2H)

1.60 (d, J = 7.0 Hz, 3H)

0.94 (t, J = 7.3 Hz, 3H).

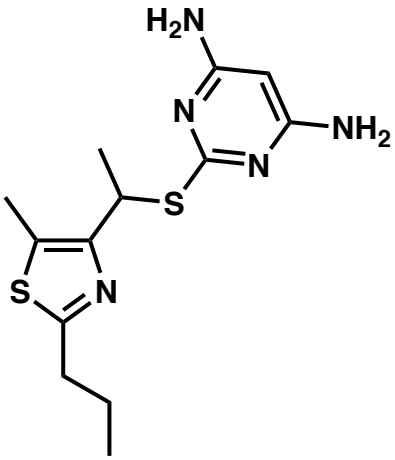

NMc-4

^{13}C NMR (100 MHz, DMSO-d_6) δ 168.1, 166.5, 163.4, 151.9, 125.5, 79.0, 36.0, 34.5, 22.8, 22.3, 13.4, 11.0.

HRMS-ESI (m/z) calcd for $C_{13}H_{20}N_5S_2$ $[M+H]^+$ 310.11601, found 310.11396.

Morpholine-4-carbothioamide (I21)

I21 was synthesized according to General Method A from morpholine-4-carbonitrile. 1.316 g, 91% yield.

^{1}H NMR (400 MHz, DMSO-d_6) δ:

7.49 (br s, 2H)

3.71 (t, J = 4.4 Hz, 4H)

3.56 (t, J = 4.9 Hz, 4H).

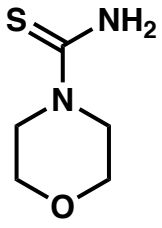

I21

HRMS-ESI (m/z) calcd for $C_5H_{11}N_2OS$ $[M+H]^+$ 147.05921, found 147.06193.

1-(5-Methyl-2-morpholinothiazol-4-yl)ethan-1-one (I22)

I22 was synthesized according to General Method B from precursor **I21.** 42 mg, 19% yield.

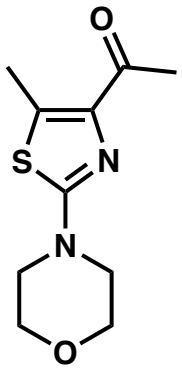

I22

^{1}H NMR (400 MHz, $CDCl_3$) δ:

3.81 (t, J = 4.9 Hz, 4H)

3.41 (t, J = 4.9 Hz, 4H)

2.61 (s, 3H)

2.52 (s, 3H).

^{13}C NMR (100 MHz, $CDCl_3$) δ 196.1, 166.0, 145.1, 133.3, 66.3, 48.6, 29.5, 13.1.

1-(5-Methyl-2-morpholinothiazol-4-yl)ethan-1-ol (I23)

I23 was synthesized according to General Method D starting from precursor **I22**. 24 mg, 57% yield.

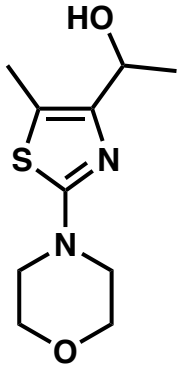

I23

HRMS-ESI (m/z) calcd for $C_{10}H_{17}N_2O_2S$ $[M+H]^+$ 229.10107, found 229.10375.

1-(5-Methyl-2-morpholinothiazol-4-yl)ethyl 2,2,2-trifluoroacetate (I24)

I24 was synthesized according to General Method F from precursor **I23**. The crude product taken directly to the next step following workup due to the instability of the trifluoroacetate.

HRMS-ESI (*m/z*) calcd for $C_{12}H_{16}F_3N_2O_3S$ $[M+H]^+$ 325.08337, found 325.08372.

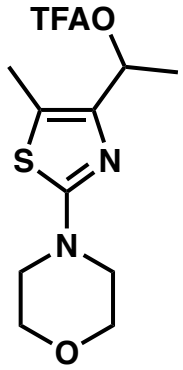

I24

2-((1-(5-Methyl-2-morpholinothiazol-4-yl)ethyl)thio)pyrimidine-4,6-diamine (NMc-5)

NMc-5 was synthesized according to General Method G. 22 mg, 59% yield.

^{1}H NMR (400 MHz, DMSO-d_6) δ:

6.07 (br s, 4H)

5.13 (br s, 1H)

5.04 (q, J = 6.9 Hz, 1H)

3.68 (t, J = 4.8 Hz, 4H)

3.28 (t, J = 4.8 Hz, 4H)

2.27 (s, 3H)

1.55 (d, J = 7.0 Hz).

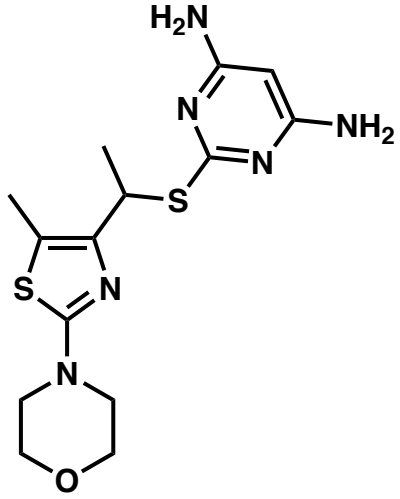

NMc-5

^{13}C NMR (100 MHz, DMSO-d_6) δ 168.3, 167.6, 163.5, 148.6, 114.6, 79.0, 65.4, 48.0, 36.2, 22.2, 10.8.

HRMS-ESI (*m/z*) calcd for $C_{14}H_{21}N_6S_2$ $[M+H]^+$ 353.12183, found 353.12249.

2-(5-Methyl-2-phenylthiazol-4-yl)propan-2-ol (I25)

I25 was synthesized according to General Method E from precursor **I6**. 1.70 g, 75% yield.

^{1}H NMR (400 MHz, $CDCl_3$) δ:

7.87 (m, 2H)

7.40 (m, 3H)

3.97 (br s, 1H)

2.55 (s, 3H)

1.64 (s, 6H).

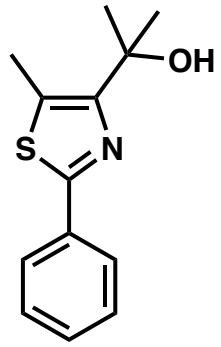

I25

^{13}C NMR (100 MHz, $CDCl_3$) δ 162.0, 158.0, 133.4, 129.7, 128.9, 126.1, 125.8, 71.8, 30.1, 12.6.

HRMS-ESI (*m*/*z*) calcd for $C_{13}H_{16}NOS$ $[M+H]^+$ 234.09526, found 234.09582.

4-(2-Chloropropan-2-yl)-5-methyl-2-phenylthiazole (I26)

I26 was synthesized according to General Method H from precursor **I25**. It was taken directly to the next step due to the instability of the tertiary chloride.

HRMS-ESI (*m*/*z*) calcd for $C_{13}H_{15}ClNS$ $[M+H]^+$ 252.06137, found 252.05949.

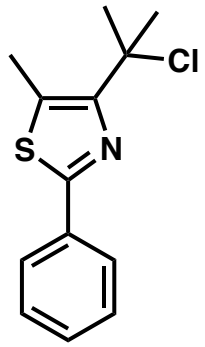

I26

2-((2-(5-Methyl-2-phenylthiazol-4-yl)propan-2-yl)thio)pyrimidine-4,6-diamine (NMc-6)

NMc-6 was synthesized according to General Method I from crude precursor **I26**. 61 mg, 19% yield.

^{1}H NMR (400 MHz, DMSO-d_6) δ:

7.83 (m, 2H)

7.46 (m, 3H)

5.92 (br s, 4H)

5.12 (s, 1H)

2.67 (s, 3H)

2.07 (s, 6H).

^{13}C NMR (100 MHz, DMSO-d_6) δ 169.2, 163.2, 159.7, 155.2, 133.3, 129.6, 129.5, 129.1, 125.6, 79.3, 50.2, 29.1, 13.4.

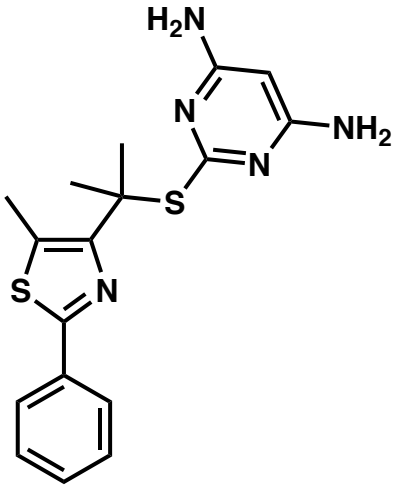

NMc-6

Ethyl 2-phenylthiazole-4-carboxylate (I27)

I27 was synthesized according to General Method C from precursor thiobenzamide. 1.40 g, 78% yield.

^{1}H NMR (400 MHz, $CDCl_3$) δ:

8.13 (s, 1H)

7.98 (m, 2H)

7.42 (m, 3H)

4.42 (q, J = 7.1 Hz, 2H)

1.40 (t, J = 7.1 Hz, 3H).

^{13}C NMR (100 MHz, $CDCl_3$) δ 168.9, 161.5, 148.1, 132.8, 130.7, 129.0, 127.1, 127.0, 61.5, 14.4.

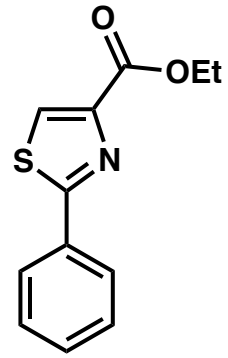

I27

2-(2-Phenylthiazol-4-yl)propan-2-ol (I28)

I28 was synthesized according to General Method E from precursor **I27**. 322 mg, 70% yield.

^{1}H NMR (400 MHz, $CDCl_3$) δ:

7.95 (m, 2H)

7.42 (m, 3H)

7.08 (s, 1H)

3.04 (br s, 1H)

1.65 (s, 6H).

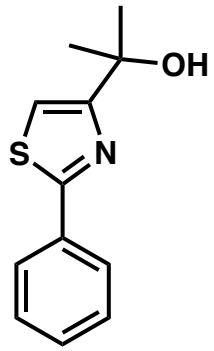

I28

^{13}C NMR (100 MHz, $CDCl_3$) δ 168.0, 165.0, 133.7, 130.1, 129.0, 126.7, 111.3, 71.3, 30.2.

HRMS-ESI (*m*/*z*) $[M+H]^+$ calcd for $C_{12}H_{14}NOS$ 220.07961, found 220.08266.

4-(2-Chloropropan-2-yl)-2-phenylthiazole (I29)

I29 was synthesized according to General Method H from precursor **I28**. The crude product was taken directly to the next step due to the instability of the tertiary chloride.

HRMS-ESI (*m*/*z*) calcd for $C_{12}H_{13}ClNS$ $[M+H]^+$ 238.04572, found 238.04814.

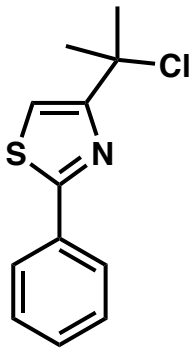

I29

2-((2-(2-Phenylthiazol-4-yl)propan-2-yl)thio)pyrimidine-4,6-diamine (NMc-7)

NMc-7 was synthesized according to General Method I from precursor **I29**. 22 mg, 10% yield (two steps).

^{1}H NMR (400 MHz, $CDCl_3$) δ:

7.94 (m, 2H)

7.40 (m, 3H)

7.22 (s, 1H)

5.16 (s, 1H)

4.58 (br s, 4H)

2.02 (s, 6H).

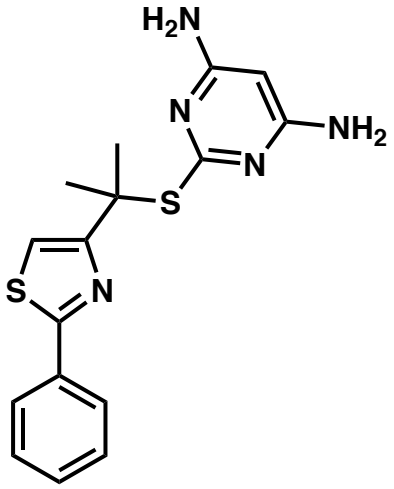

NMc-7

^{13}C NMR (100 MHz, $CDCl_3$) δ 170.1, 166.4, 162.8, 152.9, 134.2, 129.8, 128.9, 126.7, 114.2, 80.9, 50.4, 29.2.

HRMS-ESI (*m*/*z*) calcd for $C_{16}H_{18}N_5S_2$ $[M+H]^+$ 344.10036, found 344.10073.

Ethyl 2-(adamantan-1-yl)thiazole-4-carboxylate (I30)

I30 was synthesized according to General Method C from precursor **I13**. 530 mg, 68% yield.

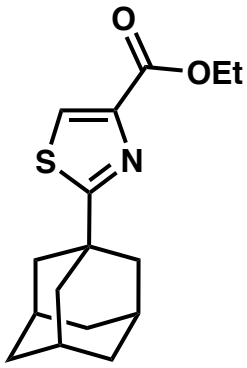

I30

^{1}H NMR (400 MHz, $CDCl_3$) δ:

8.02 (s, 1H)

4.39 (q, J = 7.1 Hz, 2H)

2.09 (br m, 9H)

1.77 (br m, 6H)

1.38 (t, J = 7.1 Hz, 3H).

^{13}C NMR (100 MHz, $CDCl_3$) δ 182.4, 161.8, 146.7, 126.0, 61.3, 43.1, 40.0, 36.5, 28.6, 14.5.

2-((2-Adamantan-1-yl)thiazol-4-yl)propan-2-ol (I31)

I31 was synthesized according to General Method E from precursor **I30**. 435 mg, 96% yield.

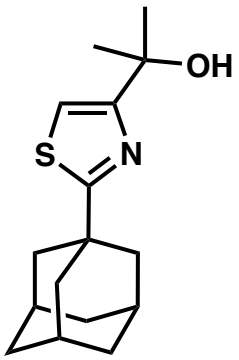

I31

^{1}H NMR (400 MHz, $CDCl_3$) δ:

6.87 (s, 1H)

3.19 (br s, 1H)

2.04 (br m, 9H)

1.78 (br m, 6H)

1.57 (s, 6H).

^{13}C NMR (100 MHz, $CDCl_3$) δ 181.34, 163.1, 109.0, 70.9, 43.3, 36.7, 35.9, 30.1, 28.7.

HRMS-ESI (*m*/*z*) calcd for $C_{16}H_{24}NOS$ $[M+H]^+$ 278.15786, found 178.15738.

2-(Adamantan-1-yl)-4-(2-chloropropan-2-yl)thiazole (I32)

I32 was synthesized using General Method H from precursor **I31**. The crude product was taken directly to the next step due to the instability of the tertiary chloride.

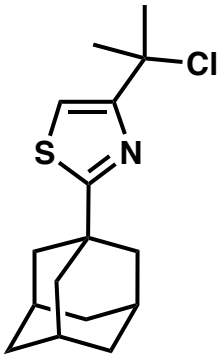

I32

2-((2-(2-Adamantan-1-yl)thiazol-4-yl)propan-2-yl)thiopyrimidine-4,6-diamine (NMc-8)

NMc-8 was synthesized according to General Method I from crude precursor **I32**. 95 mg, 16% yield (two steps).

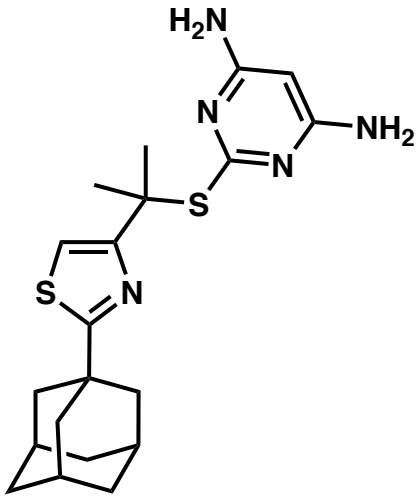

NMc-8

^{1}H NMR (400 MHz, DMSO-d_6) δ:

7.50 (s, 1H)

6.05 (br s, 4H)

5.10 (s, 1H)

2.04 (br m, 3H)

1.95 (br m, 6H)

1.94 (s, 6H)

1.73 (br m, 6H).

^{13}C NMR (100 MHz, DMSO-d_6) δ 178.2, 169.0, 162.9, 159.4, 113.6, 79.0, 49.1, 42.7, 38.8, 36.0, 28.3, 28.0.

HRMS-ESI (*m*/*z*) calcd for $C_{20}H_{28}N_5S_2$ $[M+H]^+$ 402.17861, found 402.17839.

Ethyl 2-(3-hydroxy-4-methoxyphenyl)thiazole-4-carboxylate (I33)

I33 was synthesized according to General Method A from 3-hydroxy-4-methoxybenzothioamide. 1.0 g, 97% yield.

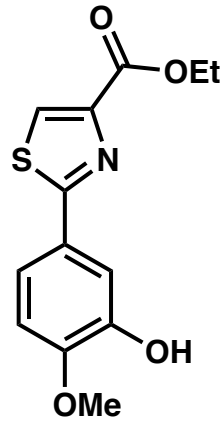

I33

^{1}H NMR (400 MHz, DMSO-d_6) δ:

8.44 (s, 1H)

7.44 (d, J = 2.2 Hz, 1H)

7.37 (dd, J = 8.4, 2.2 Hz, 1H)

7.0 (d, J = 8.4 Hz, 1H)

4.32 (q, J = 7.1 Hz, 2H)

3.82 (s, 3H)

1.32 (t, J = 7.1 Hz, 3H).

^{13}C NMR (100 MHz, DMSO-d_6) δ 167.9, 160.8, 150.2, 147.0, 146.7, 128.2, 125.3, 118.2, 113.0, 112.4, 60.8, 55.7, 14.2.

Ethyl 2-(4-methoxy-3-((triisopropylsilyl)oxy)phenyl)thiazole-4-carboxylate (I34)

To a solution of **I33** (1.0g, 3.58 mmol) in THF (14 mL) and DMF (0.5 mL) was added imidazole (730 mg, 10.7 mmol) and then TIPSCl (1.07 mL, 5.01 mL). The reaction was stirred for 18 hr and then concentrated *in vacuo*. The resulting residue was dissolved in ethyl acetate and washed with deionized water and brine before drying over Na_2SO_4. The organic layer was then concentrated *in vacuo* and the crude residue was purified by flash column chromatography on silica gel (20% ethyl acetate in hexanes. 1.192 g, 76% yield.

^{1}H NMR (400 MHz, $CDCl_3$) δ:

8.07 (s, 1H)

7.61 (dd, J = 8.4, 2.2 Hz, 1H)

7.47 (d, J = 2.2 Hz, 1H)

6.88 (d, J = 8.5 Hz, 1H)

4.43 (q, J = 7.1 Hz, 2H)

3.85 (s, 3H)

1.42 (t, J = 7.1 Hz, 3H)

1.28 (m, 3H)

1.11 (d, J = 7.3 Hz, 18H).

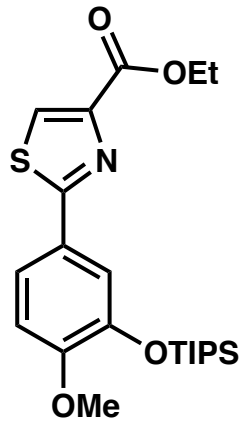

I34

^{13}C NMR (100 MHz, $CDCl_3$) δ 169.0, 161.7, 153.3, 148.0, 145.8, 126.4, 126.0, 120.7, 119.2, 111.9, 61.5, 55.6, 18.0, 14.5, 13.1.

2-(2-(4-Methoxy-3-((triisopropylsilyl)oxy)phenyl)thiazol-4-yl)propan-2-ol (I35)

I35 was synthesized according to General Procedure E from precursor **I34**. 860 mg, 98% yield.

^{1}H NMR (400 MHz, $CDCl_3$) δ:

7.52 (dd, J = 8.4, 2.1 Hz, 1H)

7.47 (d, J = 2.2 Hz, 1H)

6.98 (s, 1H)

6.87 (d, J = 8.4 Hz, 1H)

3.85 (s, 3H)

3.05 (br s, 1H)

1.63 (s, 6H)

1.28 (m, 3H)

1.12 (d, J = 7.2 Hz, 18H).

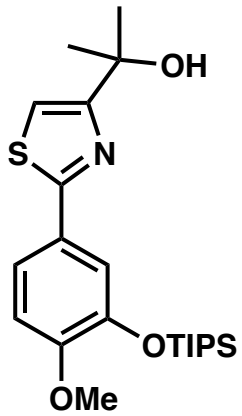

I35

^{13}C NMR (100 MHz, $CDCl_3$) δ 167.9, 164.5, 152.7, 145.7, 126.5, 120.0, 118.6, 111.9, 110.1, 71.1, 55.5, 30.1, 17.9, 12.9.

HRMS-ESI (*m*/*z*) calcd for $C_{22}H_{36}NO_3SSi$ $[M+H]^+$ 421.21069, found 421.21028.

4-(2-Chloropropan-2-yl)-2-(4-methoxy-3-((triisopropylsilyl)oxy)phenyl)thiazole (I36)

I36 was synthesized according to General Method H from precursor **I35**. The crude product was taken directly to the next step due to the instability of the tertiary chloride.

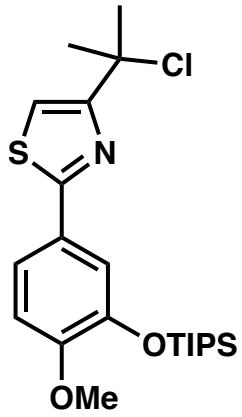

I36

2-((2-(2-(4-Methoxy-3-((triisopropylsilyl)oxy)phenyl)thiazol-4-yl)propan-2-yl)thio)pyrimidine-4,6-diamine (I37)

I37 was synthesized according to General Method I with precursor **I36.**

^{1}H NMR (400 MHz, $CDCl_3$) δ:

7.52 (dd, J = 8.3, 2.2 Hz, 1H)

7.46 (d, J = 2.1 Hz, 1H)

7.14 (s, 1H)

6.84 (d, J = 8.5 Hz, 1H)

5.18 (s, 1H)

4.68 (br s, 4H)

3.83 (s, 3H)

2.00 (s, 6H)

1.26 (m, 3H)

1.11 (d, J = 7.2 Hz, 18H).

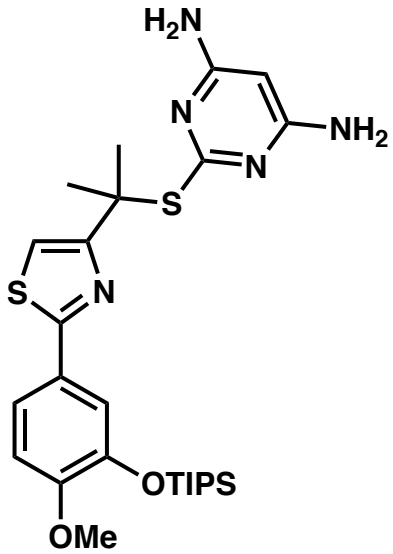

I37

HRMS-ESI (m/z) calcd for $C_{22}H_{40}N_5O_2S_2Si$ $[M+H]^+$ 535.23144, found 535.23185.

5-(4-(2-((4,6-Diaminopyrimidin-2-yl)thio)propan-2-yl)thiazol-2-yl)-2-methoxyphenol (NMc-10)

To a solution of **I37** (58 mg, 0.1063 mmol) in THF (1.2 mL) at 0 °C was added TBAF (1.0 M in THF, 0.13 mL, 0.13 mmol) and the mixture was stirred for 2 hr before a second addition of TBAF (1.0 M in THF, 0.08 mL, 0.08 mmol). The reaction solution was stirred for an additional hour and then quenched with deionized water. The aqueous solution was then extracted four times with ethyl acetate. The combined organic layers were washed with saturated sodium bicarbonate solution, brine, dried over anhydrous Na_2SO_4 and concentrated *in vacuo*. The residue was purified by flash column chromatography over silica gel using 50–75% ethyl acetate in hexanes. 30 mg, 72% yield.

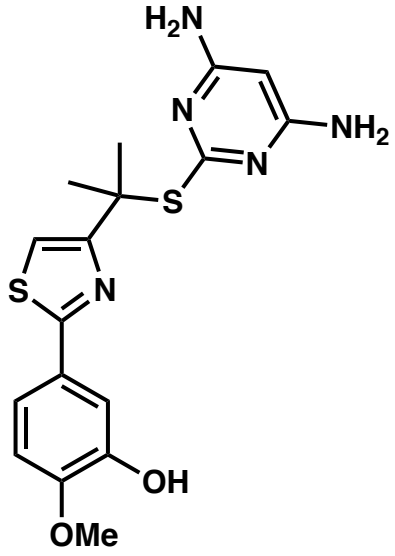

NMc-10

H NMR (400 MHz, DMSO-d_6) δ:

9.36 (s, 1H)

7.59 (s, 1H)

7.39 (d, J = 2.0 Hz, 1H)

7.29 (dd, J = 8.4, 2.0 Hz, 1H)

7.00 (d, J = 8.4 Hz, 1H)

6.00 (m, 4H)

5.08 (s, 1H)

3.81 (s, 3H)

1.97 (s, 6H).

^{13}C NMR (100 MHz, DMSO-d_6) δ 169.0, 165.1, 163.1, 161.0, 149.4, 146.8, 126.3, 117.5, 114.9, 112.7, 112.3, 79.0, 55.6, 48.8, 28.4.

HRMS-ESI (m/z) calcd for $C_{17}H_{20}N_5O_2S_2$ $[M+H]^+$ 390.1058, found 390.1043.

2-((2-(2-(4-Methoxy-3-(2-morpholinoethoxy)phenyl)thiazol-4-yl)propan-2-yl)thio)pyrimidine-4,6-diamine (NMc-9)

To a heterogenous solution of **NMc-10** (22 mg, 0.0565 mmol) and K_2CO_3 (23.4 mg, 0.169 mmol) in DMF was added 4-(2-chloroethyl)morpholine hydrochloride (11 mg, 0.0565 mmol) and the reaction was stirred at 70 °C for 12 hr. The reaction was then concentrated *in vacuo* and the residue purified by flash column chromatography over silica gel using 5% methanol in DCM as eluent. 21 mg, 75% yield.

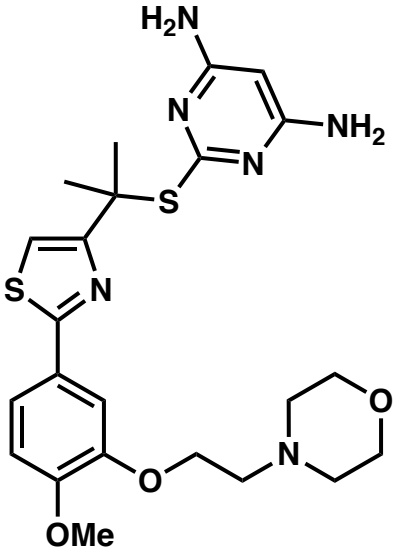

NMc-10

^{1}H NMR (400 MHz, $CDCl_3$) δ:

7.56 (d, *J* = 1.8 Hz, 1H)

7.47 (dd, *J* = 8.4, 1.9 Hz, 1H)

7.14 (s, 1H)

6.86 (d, *J* = 8.4 Hz, 1H)

5.15 (s, 1H)

4.56 (br s, 4H)

4.24 (t, *J* = 6.0 Hz, 2H)

3.88 (s, 3H)

3.74 (t, *J* = 9.2 Hz, 4H)

2.87 (t, *J* = 6.0 Hz, 2H)

2.62 (t, *J* = 8.6 Hz, 4H)

2.01 (s, 6H).

^{13}C NMR (100 MHz, $CDCl_3$) δ 170.4, 166.2, 162.9, 162.4, 151.1, 148.4, 127.4, 120.2, 113.4, 111.8, 111.7, 80.9, 67.0, 66.9, 57.6, 56.1, 54.2, 50.3, 29.1.

HRMS-ESI (*m*/*z*) calcd for $C_{23}H_{31}N_6O_3S_2$ $[M+H]^+$ 503.18991, found 503.18724.

Ethyl 2-(3,4-dimethoxyphenyl)thiazole-4-carboxylate (I38)

To a solution of **I33** (560 mg, 2.00 mmol) and K_2CO_3 in DMF was added methyl triflate (0.33 mL, 3.00 mmol) dropwise. The reaction was stirred for 12 hr and then concentrated *in vacuo*, the residue taken up in ethyl acetate and the organic layer consecutively washed with saturated sodium bicarbonate solution, water, and brine. The organic layer dried over anhydrous Na_2SO_4, concentrated *in vacuo*, and resulting crude product purified by flash chromatography over silica gel using 1% MeOH in DCM as the eluent. 421 mg, 72% yield.

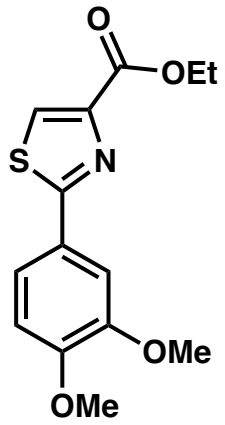

I38

^{1}H NMR (400 MHz, $CDCl_3$) δ:

8.09 (s, 1H)

7.60 (d, J = 2.1 Hz, 1H)

7.50 (dd, J = 8.3, 2.1 Hz, 1H)

6.90 (d, J = 8.4 Hz, 1H)

4.44 (q, J = 7.1 Hz, 2H)

3.99 (s, 3H)

3.93 (s, 3H)

1.42 (t, J = 7.1 Hz, 3H).

^{13}C NMR (100 MHz, $CDCl_3$) δ 169.0, 161.6, 151.4, 149.4, 147.9, 126.6, 126.1, 120.4, 111.1, 109.7, 61.6, 56.3, 56.1, 14.5.

2-(2-(3,4-Dimethoxyphenyl)thiazol-4-yl)propan-2-ol (I39)

I39 was synthesized according to General Method E from precursor **I38**. 300 mg, 82% yield.

^{1}H NMR (400 MHz, $CDCl_3$) δ:

7.51 (d, J = 2.0 Hz, 1H)

7.47 (dd, J = 8.3, 2.1 Hz, 1H)

7.00 (s, 1H)

6.89 (d, J = 8.4 Hz, 1H)

3.97 (s, 3H)

3.92 (s, 3H)

3.04 (br s, 1H)

1.64 (s, 6H).

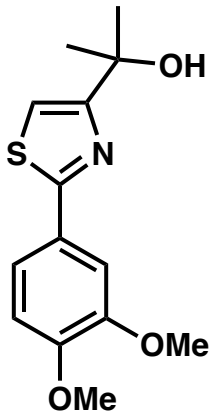

I39

^{13}C NMR (100 MHz, $CDCl_3$) δ 167.9, 164.6, 150.8, 149.2, 126.8, 119.7, 111.1, 110.4, 109.3, 71.1, 56.1, 56.0, 30.1.

4-(2-Chloropropan-2-yl)-2-(3,4-dimethoxyphenyl)thiazole (I40)

I40 was synthesized according to General Method H. The crude product was taken directly to the next step due to the instability of the tertiary chloride.

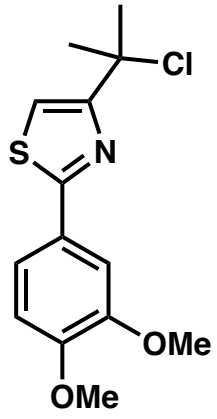

I40

2-((2-(2-(3,4-Dimethoxyphenyl)thiazol-4-yl)propan-2-yl)thio)pyrimidine-4,6-diamine (NMc-11)

NMc-11 was synthesized according to General Method I from crude precursor **I40**. 39 mg, 7% yield.

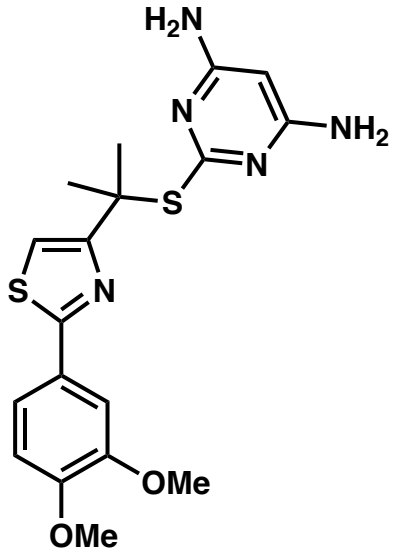

NMc-11

^{1}H NMR (400 MHz, $CDCl_3$) δ:

7.53 (d, J = 2.0 Hz, 1H)

7.47 (dd, J = 8.3, 2.0 Hz, 1H)

7.16 (s, 1H)

6.87 (d, J = 8.4 Hz, 1H)

5.17 (s, 1H)

4.53 (br s, 4H)

3.97 (s, 3H)

3.92 (s, 3H)

2.03 (s, 6H).

^{13}C NMR (100 MHz, $CDCl_3$) δ 166.5, 162.7, 162.4, 162.1, 150.6, 149.3, 127.4, 119.7, 113.5, 111.2, 109.5, 80.7, 56.2, 56.1, 50.69, 29.1.

HRMS-ESI (m/z) calcd for $C_{18}H_{22}N_5O_2S_2$ $[M+H]^+$ 404.12149, found 404.12186.

Ethyl 2-(4-fluorophenyl)thiazole-4-carboxylate (I41)

I41 was synthesized according to General Method C starting from 4-fluorothiobenzoamide. 478 mg, 68% yield.

^{1}H NMR (400 MHz, $CDCl_3$) δ:

8.13 (s, 1H)

7.99 (m, 2H)

7.13 (m, 2H)

4.44 (q, *J* = 7.1 Hz, 2H)

1.42 (t, *J* = 7.1 Hz, 3H).

^{13}C NMR (100 MHz, $CDCl_3$) δ 166.68 (*J*C–F = 213.8 Hz), 163.12, 161.5, 148.3, 129.3 (d, *J*C–F = 3.3 Hz), 129.1 (d, *J*C–F = 8.6 Hz), 127.1, 116.2 (d, *J*C–F = 22.2 Hz), 61.7, 14.5.

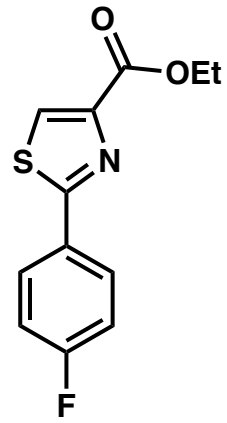

I41

2-(2-(4-Fluorophenyl)thiazol-4-yl)propan-2-ol (I42)

I42 was synthesized according to General Method E from precursor **I41**. 101 mg, 92% yield.

^{1}H NMR (400 MHz, $CDCl_3$) δ:

7.94 (m, 2H)

7.12 (m, 2H)

7.08 (s, 1H)

2.86 (br s, 1H)

1.65 (s, 6H).

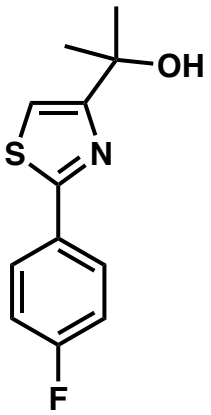

I42

HRMS-ESI (*m*/*z*) calcd for $C_{12}H_{13}FNOS$ $[M+H]^+$ 238.07019, found 238.07284.

4-(2-Chloropropan-2-yl)-2-(4-fluorophenyl)thiazole (I43)

I43 was synthesized according to General Method H from precursor **I42**. The crude product was taken directly to the next step due to the instability of the tertiary chloride.

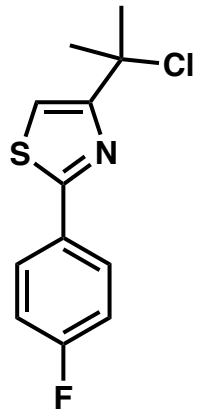

I43

2-((2-(2-(4-Fluorophenyl)thiazol-4-yl)propan-2-yl)thio)pyrimidine-4,6-diamine (NMc-12)

NMc-12 was synthesized according to General Method I from crude precursor **I43**.

^{1}H NMR (400 MHz, DMSO-d_6) δ:

7.95 (m, 2H)

7.75 (s, 1H)

7.32 (m, 2H)

6.28 (br s, 4H)

5.12 (s, 1H)

1.98 (s, 6H).

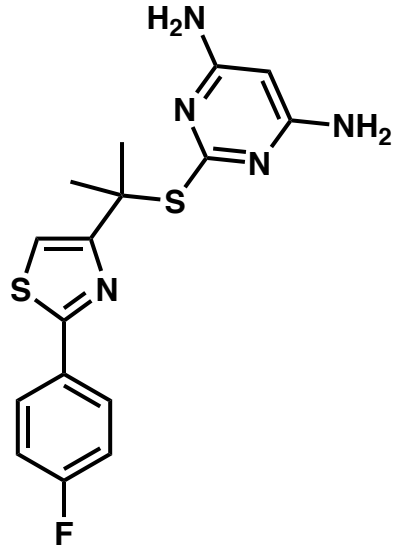

NMc-12

HRMS-ESI (*m/z*) calcd for $C_{16}H_{17}FN_5S_2$ $[M+H]^+$ 362.0909, found 362.08878.

2,4-Difluorobenzothioamide (I44)

I44 was synthesized according to General Method A from 2,4-difluorobenzonitrile. 487 mg, 58% yield.

^{1}H NMR (400 MHz, $CDCl_3$) δ:

8.42 (td, *J* = 13.9, 6.6 Hz, 1H)

8.08 (br s, 1H)

7.73 (br s, 1H)

6.97 (m, 1H)

6.84 (ddd, *J* = 12.5, 8.3, 2.5 Hz, 1H).

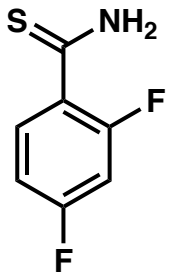

I44

^{13}C NMR (100 MHz, $CDCl_3$) δ 195.8, 165.3 (*J*C–F = 257.3, 13.0), 159.0 (*J*C–F = 252.9, 12.4 Hz), 137.2 (dd, *J*C–F = 10.1, 2.3 Hz), 121.7 (dd, *J*C–F = 9.8, 4.0 Hz), 112.5 (dd, *J*C–F = 21.1, 3.4 Hz), 104.2 (dd, *J*C–F = 28.5, 25.9 Hz).

Ethyl 2-(2,4-difluorophenyl)thiazole-4-carboxylate (I45)

I45 was synthesized according to General Method C from precursor **I44**. 478 mg, 68% yield.

^{1}H NMR (400 MHz, $CDCl_3$) δ:

8.40 (td, *J* = 13.0, 6.5 Hz, 1H)

8.24 (s, 1H)

7.01 (m, 1H)

6.95 (ddd, *J* = 11.1, 8.6, 2.5 Hz, 1H)

4.44 (q, *J* = 7.1 Hz, 2H)

1.42 (t, *J* = 7.1 Hz, 3H).

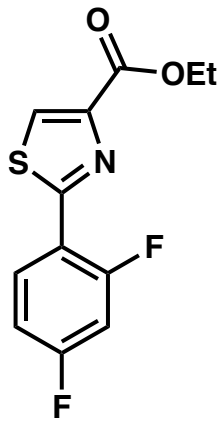

I45

^{13}C NMR (100 MHz, $CDCl_3$) δ 164.1 (dd, *J*C–F = 254.2, 12.2 Hz), 161.5, 160.5 (dd, *J*C–F = 254.5, 12.1 Hz), 160.5 (d, *J*C–F = 5.1 Hz), 147.1, 130.9 (dd, *J*C–F = 9.9, 4.0 Hz), 128.0 (d, *J*C–F = 8.9 Hz), 117.4 (dd, *J*C–F = 11.6, 3.9 Hz), 112.5 (dd, *J*C–F = 21.7, 3.4 Hz), 104.5 (t, *J*C–F = 25.8 Hz), 61.7, 14.5.

2-(2-(2,4-Difluorophenyl)thiazol-4-yl)propan-2-ol (I46)

I46 was synthesized according to General Method E from precursor **I45**. 354 mg, 84% yield.

^{1}H NMR (400 MHz, $CDCl_3$) δ:

8.30 (td, *J* = 13.0, 6.5 Hz, 1H)

7.21 (s, 1H)

7.00 (m, 1H)

6.94 (ddd, *J* = 11.1, 8.6, 2.5 Hz, 1H)

2.88 (br s, 1H)

1.65 (s, 6H).

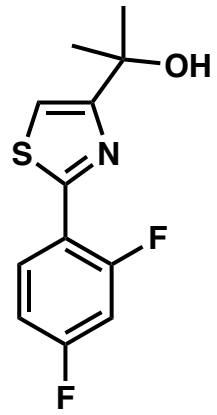

I46

HRMS-ESI (*m/z*) calcd for $C_{12}H_{12}F_2NOS$ $[M+H]^+$ 256.06077, found 256.06389.

4-(2-Chloropropan-2-yl)-2-(2,4-difluorophenyl)thiazole (I47)

I47 was synthesized according to General Method H from precursor **I46**. The crude product was taken directly to the next step due to the instability of the tertiary chloride.

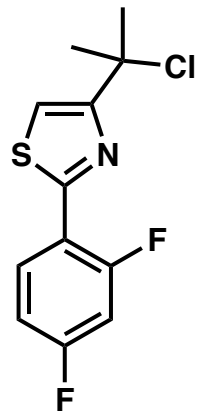

I47

2-((2-(2-(2,4-Difluorophenyl)thiazol-4-yl)propan-2-yl)thio)pyrimidine-4,6-diamine (NMc-13)

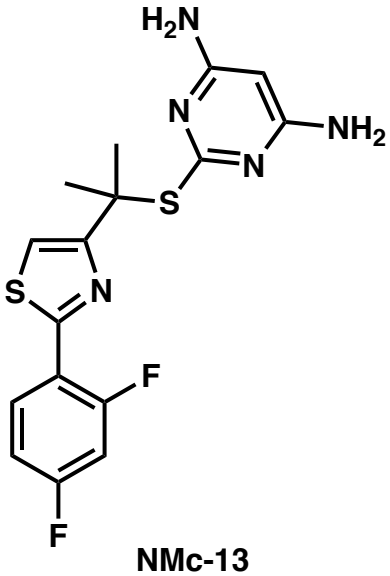

NMc-13

NMc-13 was synthesized according to General Method I. 41 mg, 16% yield. The 4 amine protons of the 4,6-diaminopyrimidine ring exchanged in the NMR solvent (CD_3OD).

^{1}H NMR (400 MHz, CD_3OD) δ:

8.30 (m, 1H)

7.60 (s, 1H)

7.09 (m, 2H)

5.23 (s, 1H)

2.03 (s, 6H).

HRMS-ESI (*m/z*) calcd for $C_{16}H_{16}F_2N_5S_2$ $[M+H]^+$ 379.07369, found 379.07728.

Cyclopropanecarbothioamide (I48)

I48 was synthesized according to General Method A from cyclopropanecarbonitrile. 545 mg, 40% yield.

^{1}H NMR (400 MHz, $CDCl_3$) δ:

7.57 (br s, 1H)

7.11 (br s, 1H)

1.89 (m, 1H)

1.27 (m, 2H)

1.01 (m, 2H).

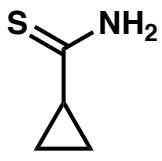

I48

^{13}C NMR (100 MHz, $CDCl_3$) δ: 212.5, 23.6, 13.5.

Ethyl 2-cyclopropylthiazole-4-carboxylate (I49)

I49 was synthesized according to General Method C from precursor **I48**. 273 mg, 15% yield.

^{1}H NMR (400 MHz, $CDCl_3$) δ:

7.93 (d, J = 0.5 Hz, 1H)

4.40 (q, J = 7.1 Hz, 2H)

2.40 (m, 1H)

1.39 (t, J = 7.1 Hz, 3H)

1.17 (m, 2H)

1.07 (m, 2H).

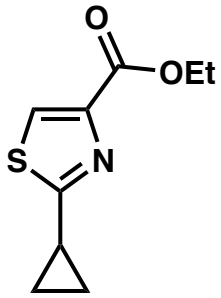

I49

HRMS-ESI (m/z) calcd for $C_9H_{12}NO_2S$ $[M+H]^+$ 198.05887, found 198.06382.

2-(2-Cyclopropylthiazol-4-yl)propan-2-ol (I50)

I50 was synthesized according to General Method E from precursor **I49**. 180 mg, 73% yield.

^{1}H NMR (400 MHz, $CDCl_3$) δ:

6.80 (s, 1H)

2.85 (br s, 1H)

2.30 (m, 1H)

1.57 (s, 6H)

1.11 (m, 2H)

1.04 (m, 2H).

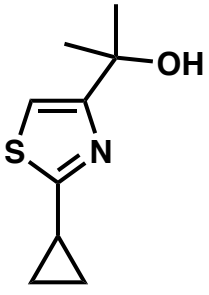

I50

HRMS-ESI (m/z) calcd for $C_9H_{14}NOS$ $[M+H]^+$ 184.07961, found 184.08291.

4-(2-Chloropropan-2-yl)-2-cyclopropylthiazole (I51)

I51 was synthesized according to General Method H from precursor **I50**. The crude product was taken directly to the next step due to the instability of the tertiary chloride.

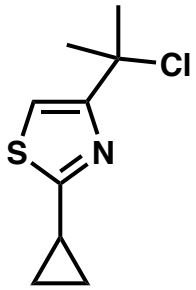

I51

2-((2-(2-Cyclopropylthiazol-4-yl)propan-2-yl)thio)pyrimidine-4,6-diamine (NMc-14)

NMc-14 was synthesized according to General Method I from crude precursor **I51**. 31 mg, 11% yield. The 4 amine protons of the 4,6-diaminopyrimidine ring exchanged in the NMR solvent (CD_3OD).

^{1}H NMR (400 MHz, CD_3OD) δ:

7.19 (s, 1H)

5.25 (s, 1H)

2.33 (m, 1H)

1.95 (s, 6H)

1.12 (m, 2H)

0.91 (m, 2H).

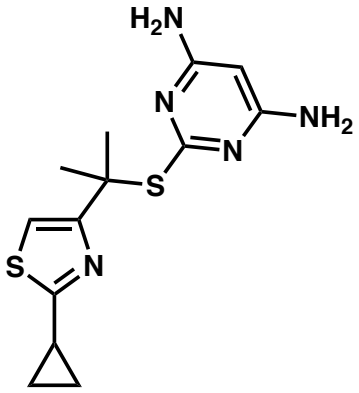

NMc-14

^{13}C NMR (100 MHz, CD_3OD) δ: 174.7, 169.7, 164.3, 161.3, 113.6, 80.5, 51.1, 29.1, 15.2, 11.4.

HRMS-ESI (*m*/*z*) calcd for $C_{13}H_{15}N_5S_2$ $[M+H]^+$ 309.10036, found 309.0993.

Ethyl 2-methylthiazole-4-carboxylate (I52)

I52 was synthesized according to General Method C from thioacetamide. 380 mg, 73% yield.

^{1}H NMR (400 MHz, $CDCl_3$) δ:

8.03 (s, 1H)

4.42 (q, J = 7.1 Hz, 2H)

2.76 (s, 3H)

1.40 (t, J = 7.1 Hz, 3H).

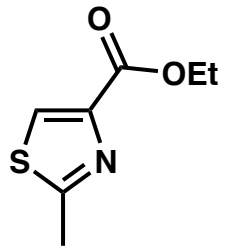

I52

^{13}C NMR (100 MHz, $CDCl_3$) δ: 166.9, 161.6, 147.0, 127.4, 61.6, 19.5, 14.5.

2-(2-Methylthiazol-4-yl)propan-2-ol (I53)

I53 was synthesized according to General Method E from precursor **I52**.

HRMS-ESI (m/z) calcd for $C_7H_{12}NOS$ $[M+H]^+$ 158.06396, found 158.06924.

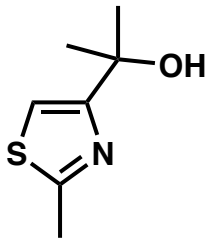

I53

4-(2-Chloropropan-2-yl)-2-methylthiazole (I54)

I54 was synthesized according to General Method H using precursor **I53**. The crude product was taken directly to the next step due to the instability of the tertiary chloride.

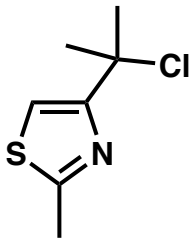

I54

2-((2-(2-Methylthiazol-4-yl)propan-2-yl)thio)pyrimidine-4,6-diamine (NMc-15)

NMc-15 was synthesized according to General Method I from crude precursor **I54**.

^{1}H NMR (400 MHz, DMSO-d_6) δ:

7.44 (s, 1H)

5.99 (br s, 4H)

5.07 (s, 1H)

2.60 (s, 3H)

1.91 (s, 6H).

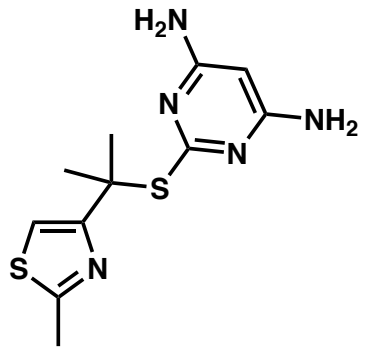

NMc-15

^{13}C NMR (100 MHz, DMSO-d_6) δ: 169.0, 163.2, 163.1, 159.8, 115.0, 79.1, 48.8, 28.4, 18.9.

2-Hydroxyethanethioamide (I55)

To a solution of ethyl thiooxamate (965 mg, 7.25 mmol) in THF (15 mL) and ethanol (15 mL) at 0 °C was added $NaBH_4$ (685 mg, 18.1 mmol) portion wise over five min. The reaction was stirred at 0 °C for 3 hr, at which point the reaction was quenched by careful addition of saturated ammonium chloride solution. The aqueous solution was extracted three times with ethyl acetate, and three times with DCM. The combined organic layers were dried over anhydrous Na_2SO_4 and then concentrated *in vacuo*. The product was taken on to next step without further purification. 485 mg, 73% yield.

^{1}H NMR (400 MHz, DMSO-d_6) δ:

9.84 (br s, 1H)

9.05 (br s, 1H)

5.77 (t, J = 5.9 Hz, 1H)

4.07 (d, J = 5.8 Hz, 2H).

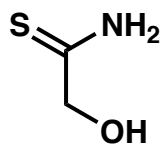

I55

Ethyl 2-(hydroxymethyl)thiazole-4-carboxylate (I56)

I56 was synthesized according to General Method C from precursor **I56**. 675 mg, 70% yield.

^{1}H NMR (400 MHz, $CDCl_3$) δ:

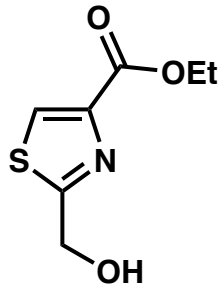

I56

8.15 (s, 1H)

5.00 (s, 2H)

4.41 (q, J = 7.1 Hz, 2H)

2.62 (br s, 1H)

1.40 (t, J = 7.1 Hz, 3H).

^{13}C NMR (100 MHz, $CDCl_3$) δ: 172.7, 161.5, 147.2, 127.7, 62.4, 61.7, 14.5.

2-(2-(Hydroxymethyl)thiazol-4-yl)propan-2-ol (I57)

I57 was synthesized according to General Method E from precursor **I56**. 331 mg, 67% yield.

^{1}H NMR (400 MHz, $CDCl_3$) δ:

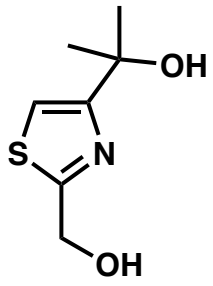

I57

7.08 (s, 1H)

4.91 (s, 2H)

2.61 (br s, 1H)

1.60 (s, 6H).

^{13}C NMR (100 MHz, $CDCl_3$) δ: 170.9, 163.9, 111.9, 71.2, 62.2, 30.1.

HRMS-ESI (m/z) calcd for $C_7H_{12}NO_2S$ $[M+H]^+$ 174.05887, found 174.05274.

4-(2-Hydroxypropan-2-yl)thiazole-2-carbaldehyde (I58)

To a solution of **I57** (173 mg, 1.0 mmol) in acetonitrile (2 mL) was added a solution of tetrakis(acetonitrile)copper(I) hexafluorophosphate (18.6 mg, 0.05 mmol) in acetonitrile (1 mL). A solution of bipyridine (7.8 mg, 0.05 mmol) in acetonitrile (1 mL) was then added, followed by TEMPO (7.8 mg, 0.05 mmol) in acetonitrile (1 mL) and *N*-methylimidazole (0.008 mL, 0.1 mmol) in acetonitrile (1 mL). The reaction solution was then stirred vigorously while open to air for three hr before concentrating *in vacuo*. The resulting residue was purified by flash column chromatography over silica gel using 40% ethyl acetate in hexanes as the eluent. 156 mg, 91% yield.

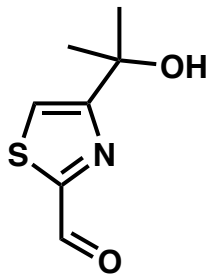

I58

^{1}H NMR (400 MHz, $CDCl_3$) δ:

9.97 (d, J = 1.2 Hz, 1H)

7.61 (d, J = 1.3 Hz, 1H)

2.53 (br s, 1H)

1.66 (s, 6H).

^{13}C NMR (100 MHz, $CDCl_3$) δ: 183.9, 167.5, 165.7, 119.6, 71.7, 30.5.

(*E*)-4-(2-Hydroxypropan-2-yl)thiazole-2-carbaldehyde oxime (I59)

To a solution of **I58** (141 mg, 0.824 mmol) and sodium acetate (108 mg, 1.32 mmol) in methanol (3 mL) was added hydroxylamine hydrochloride (86 mg, 1.24 mmol). The reaction solution was stirred for 40 min and then concentrated *in vacuo*. The resulting solid was partitioned between ethyl acetate and deionized water, the aqueous layer was extracted three times with ethyl acetate, and the combined organic layers dried over anhydrous sodium sulfate. The organic layer was

then concentrated *in vacuo* to yield the desired product as a 1:1 mixture of the *E* and *Z* isomers.

^{1}H NMR taken in DMSO-d_6, ^{13}C NMR taken in $CDCl_3$.

^{1}H NMR (400 MHz, DMSO-d_6) δ:

12.70 (s, 1H)

11.89 (s, 1H)

8.28 (d, J = 0.8 Hz, 1H)

7.95 (d, J = 1.0 Hz, 1H)

7.62 (d, J = 1.0 Hz, 1H)

7.36 (d, J = 0.9 Hz, 1H)

1.46 (s, 6H)

1.44 (s, 6H).

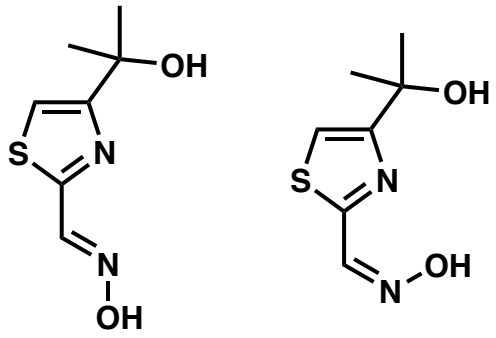

I59

^{13}C NMR (100 MHz, $CDCl_3$) δ: 164.7, 163.9, 161.9, 154.7, 145.1, 141.0, 116.9, 113.2, 71.33, 71.28, 30.3, 30.1.

HRMS-ESI (*m*/*z*) calcd for $C_7H_{11}N_2O_2S$ $[M+H]^+$ 187.05412, found 187.05468.

4-(2-Hydroxypropan-2-yl)thiazole-2-carbonitrile (I60)

To a solution of **I59** (135 mg, 0.832 mmol) in acetonitrile (3 ml) was added copper(II) acetate (15.1 mg, 0.0832 mmol) and the reaction heated to reflux for 15 min. The reaction solution was then concentrated *in vacuo* and the residue purified by flash column chromatography over silica gel using 40–66% ethyl acetate in hexanes as the eluent. 40 mg, 29% yield.

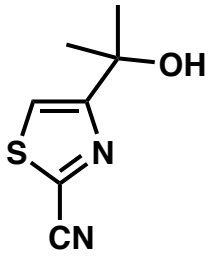

I60

^{1}H NMR (400 MHz, $CDCl_3$) δ:

7.56 (s, 1H)

2.43 (br s, 1H)

1.63 (s, 6H).

^{13}C NMR (100 MHz, $CDCl_3$) δ: 167.3, 136.2, 118.4, 112.9, 72.0, 30.5.

HRMS-ESI (*m*/*z*) calcd for $C_7H_9N_2OS$ $[M+H]^+$ 169.0436, found 169.04254.

***N*'-Hydroxy-4-(2-hydroxypropan-2-yl)thiazole-2-carboximidamide (I61)**

To a solution of **I60** (170 mg, 1.01 mmol) in ethanol (3 ml) was added hydroxylamine (50% aqueous solution, 0.11 mL, 2.02 mmol) and the reaction solution was heated to 98 °C for two hr. The reaction solution was then concentrated *in vacuo*, yielding a crystalline solid. The solid was dissolved in ethanol and concentrated once more. The product was obtained as a white crystalline solid. 200 mg, 99% yield.

^{1}H NMR (400 MHz, DMSO-d_6) δ:

10.04 (s, 1H)

7.31 (s, 1H)

5.81 (s, 2H)

5.14 (s, 1H)

1.46 (s, 6H).

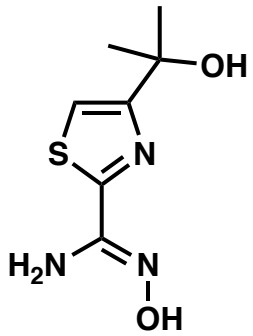

I61

^{13}C NMR (100 MHz, DMSO-d_6) δ: 164.7, 160.3, 146.9, 113.0, 70.3, 30.4.

HRMS-ESI (*m*/*z*) calcd for $C_7H_{12}N_3O_2S$ $[M+H]^+$ 202.0650, found 202.06370.

***N*'-Acetoxy-4-(2-hydroxypropan-2-yl)thiazole-2-carboximidamide (I62)**

To a solution of **I61** (143 mg, 0.711 mmol) and triethylamine (0.18 ml, 1.28 mmol) in THF (4.3 ml) was added acetyl chloride (1.0 M solution in THF, 0.782 ml, 0.782 mmol) dropwise. The

reaction solution was stirred for 70 min and then concentrated *in vacuo*. The resulting solution was partitioned between ethyl acetate and saturated ammonium chloride solution. The aqueous solution was extracted three times with ethyl acetate and the combined organic layers were dried over anhydrous sodium sulfate before being concentrated *in vacuo* to give an oil which crystallized upon standing. 164 mg, 95% yield.

^{1}H NMR (400 MHz, $CDCl_3$) δ:

7.25 (s, 1H)

5.65 (br s, 2H)

2.50 (br s, 1H)

2.26 (s, 3H)

1.62 (s, 6H).

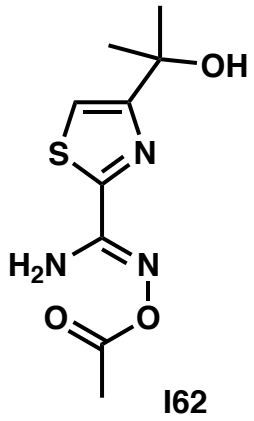

I62

^{13}C NMR (100 MHz, $CDCl_3$) δ: 168.5, 164.3, 158.1, 150.4, 115.1, 71.4, 30.3, 19.9.

2-(2-(5-Methyl-1,2,4-oxadiazol-3-yl)thiazol-4-yl)propan-2-ol (I63)

To a solution of **I62** (205 mg, 0.843 mmol) in THF (25 ml) at 0 °C was added tetrabutylammonium fluoride (TBAF, 1.0 M solution in THF, 0.17 ml, 0.17 mmol). The reaction vessel was removed from ice bath and stirred at room temperature following addition of TBAF. After two hr the reaction was quenched by addition of deionized water. Brine was added to the aqueous solution, which was then extracted with ethyl acetate four times. The combined organic layers were dried over anhydrous sodium sulfate, concentrated *in vacuo* to give a yellow oil, which was purified by flash column chromatography over silica using 1:1 ethyl acetate:hexanes as the eluent. 188 mg, 99% yield.

^{1}H NMR (400 MHz, $CDCl_3$) δ:

7.39 (s, 1H)

2.77 (br s, 1H)

2.70 (s, 3H)

1.67 (s, 6H).

^{13}C NMR (100 MHz, $CDCl_3$) δ: 177.8, 166.7, 164.1, 153.8, 115.4, 71.6, 30.3, 12.6.

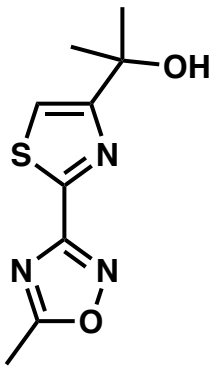

I63

HRMS-ESI (*m*/*z*) calcd for $C_9H_{12}N_3O_2S$ $[M+H]^+$ 226.0650, found 226.0674.

3-(4-(2-Chloropropan-2-yl)thiazol-2-yl)-5-methyl-1,2,4-oxadiazole (I64)

I64 was synthesized according to General Method H using precursor **I63**. The crude product was taken directly to the next step due to the instability of the tertiary chloride.

HRMS-ESI (*m*/*z*) calcd for $C_9H_{11}ClN_3OS$ $[M+H]^+$ 244.03114, found 244.03247.

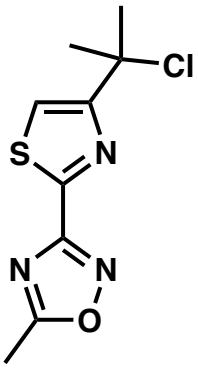

I64

2-((2-(2-(5-Methyl-1,2,4-oxadiazol-3-yl)thiazol-4-yl)propan-2-yl)thio)pyrimidine-4,6-diamine (NMc-16)

NMc-16 was synthesized according to General Method I from precursor **I64**.

^{1}H NMR (400 MHz, $CDCl_3$) δ:

7.55 (s, 1H)

5.17 (s, 1H)

4.46 (br s, 4H)

2.68 (s, 3H)

2.01 (s, 6H).

^{13}C NMR (100 MHz, $CDCl_3$) δ: 177.6, 170.1, 165.1, 164.3, 162.9, 151.8, 118.1, 80.9, 49.8, 29.6, 12.6.

HRMS-ESI (*m*/*z*) calcd for $C_{13}H_{16}N_7OS_2$ $[M+H]^+$ 350.0858, found 350.0828.

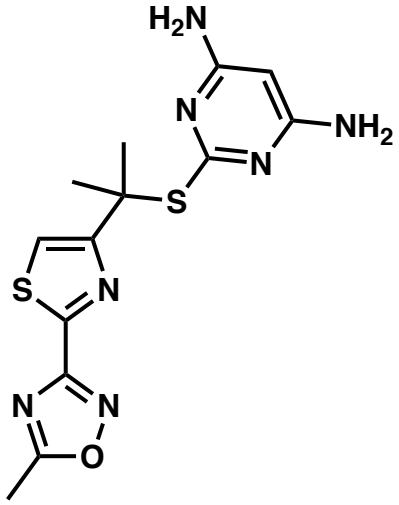

NMc-16

1.7 References

1. Hess, J. R.; Greenberg, N. A. The role of nucleotides in the immune and gastrointestinal systems: potential clinical applications. *Nutr. Clin. Pract.* **2012**, *27*, 281–294.
2. Carver, J. D.; Walker, W. A. The role of nucleotides in human nutrition. *J. Nutr. Biochem.* **1995**, *6*, 58–72.
3. Pai, C. C.; Kearsey, S. E. A Critical Balance: dNTPs and the Maintenance of Genome Stability. *Genes* **2017**, *57*, 1–14.
4. Reichard, P. Interactions Between Deoxyribonucleotide and DNA Synthesis. *Annu. Rev. Biochem.* **1988**, 57, 349–374.
5. Evans, D. R.; Guy, H. I. Mammalian pyrimidine biosynthesis: fresh insights into an ancient pathway. *J. Biol. Chem.* **2004**, *32*, 33035–33038.
6. Arner, E. S. J.; Eriksson, S. Mammalian Deoxyribonucleoside Kinases. *Pharmacol. Ther.* **1995**, *2*, 155–186.
7. Eriksson, S.; Munch-Petersen, B.; Johansson, K.; Ecklund, H. Structure and function of cellular deoxyribonucleoside kinases. *Cell. Mol. Life Sci.* **2002**, *59*, 1327–1346 (2002).
8. Toy, G.;, Austin, W. R.; Liao, H.; Cheng, D.; Singh, A.; Campbell, D. O.; Ishikawa, T.; Lehmann, L. W.; Satyamurthy, N.; Phelps, M. E.; Herschmann, H. R.; Czernin, J.; Witte, O. N.; Radu, C. G. Requirement for deoxycytidine kinase in T and B lymphocyte development. *Proc. Natl. Acad. Sci.* **2010**, *12*, 5551–5556.
9. Smal, C.; Vertommen, D.; Bertrand, L.; Ntamashimikiro, S.; Rider, M. H.; Van Den Neste, E.; Bontemps, F. Identification of Phosphorylation Sites on Human Deoxycytidine Kinase: Role of Ser-74 in the Control of Enzyme Activity. *J. Biol. Chem.* **2006**, *8*, 4887-4893.

10. Hazra, S.; Szewczak, A.; Ort, S.; Konrad, M.; Lavie, A. Post-translational phosphorylation of serine 74 of human deoxycytidine kinase favors the enzyme adopting the open conformation making it competent for nucleoside binding and release. *Biochemistry* **2011**, *14*, 2870-2880.

11. Sabini, E.; Hazra, S.; Ort, S.; Konrad, M.; Lavie, A. Structural basis for substrate promiscuity of dCK. *J. Mol. Biol.* **2008**, *3*, 607-621.

12. Van Rompay, A. R.; Johansson, M.; Karlsson, A. Substrate specificity and phosphorylation of antiviral and anticancer nucleoside analogues by human deoxyribonucleoside kinases and ribonucleoside kinases. *Pharmacol. Ther.* **2003**, *2*, 119-139.

13. Aird, K. M.; Zhang, R. Nucleotide metabolism, oncogene-induced senescence and cancer. *Cancer Lett.* **2015**, *2*, 204-210.

14. Kohnken, R.; Kodigepalli, K. M.; Wu, L. Regulation of deoxynucleotide metabolism in cancer: novel mechanisms and therapeutic implications. *Mol. Cancer.* **2015**, *14*, 176-187.

15. Madaan, K.; Kaushik, D.; Verma, T. Hydroxyurea: a key player in cancer chemotherapy. *Expert Rev. Anticancer Ther.* **2012**, 12, 19-29.

16. Kunos, C. A.; Chu, E.; Beumer, J. H.; Sznol, M.; Ivy, S. P. Phase I trial of daily triapine in combination with cisplatin chemotherapy for advanced-stage malignancies. *Cancer Chemother. Pharmacol.* **2017**, *1*, 201-207.

17. Nathanson, D. A.; Armijo, A. L.; Tom, M.; Li, Z.; Dimitrova, E.; Austin, W. R.; Nomme, J.; Campbell, D. O.; Ta, L.; Le, T. M.; Lee, J. T.; Darvish, R.; Gordin, A.; Wei, L.; Liao, H.; Wilks, M.; Martin, C.; Sadeghi, S.; Murphy, J. M.; Boulos, N.; Phelphs, M. E.; Faull, K. F.; Herschman, H. R.; Jung, M. E.; Czernin, J.; Lavie, A.; Radu, C. G. Co-targeting of

convergent nucleotide biosynthetic pathways for leukemia eradication. *J. Exp. Med.* **2014**, *3*, 473-486.

18. Cerami, E.; Gao, J.; Dogrusoz, U.; Gross, B. E.; Sumer, S. O.; Aksoy, B. A.; Jacobsen, A.; Byrne, C. J.; Heuer, M. L.; Larsson, E.; Antipin, Y.; Reva, B.; Goldberg, A. P.; Sander, C.; Schultz, N. The cBio cancer genomics portal: an open platform for exploring multidimensional cancer genomics data. *Cancer Discov.* **2012**, *2*, 401-404.
19. Austin, W. R.; Armijo, A. L.; Campbell, D. O.; Singh, A. S.; Hsieh, T.; Nathanson, D.; Herschman, H. R.; Phelps, M. E.; Czernin, J.; Radu, C. G. Nucleoside salvage pathway kinases regulate hematopoiesis by linking nucleotide metabolism with replication stress. *J. Exp. Med.* **2012**, *12*, 2215-2228.
20. Yang, C.; Lee, M.; Hao, J.; Cui, X.; Guo, X.; Smal, C.; Bontemps, F.; Ma, S.; Liu, X.; Engler, D.; Parker, W. B.; Xu, B. Deoxycytidine kinase regulates the G2/M checkpoint through interaction with cyclin-dependent kinase 1 in response to DNA damage. *Nucleic Acids Research* **2012**, *19*, 9621-9632.
21. Murphy, J. M.; Armijo, A. L.; Nomme, J.; Lee, C. H.; Smith, Q. A.; Li, Z.; Campbell, D. O.; Liao, H.; Nathanson, D. A.; Austin, W. R.; Lee, J. T.; Darvish, R.; Wei, L.; Wang, J.; Su, Y.; Damoiseaux, R.; Sadeghi, S.; Phelps, M. E.; Herschman, H. R.; Czernin, J.; Alexandrova, A. N.; Jung, M. E.; Lavie, A.; Radu, C. G. Development of New Deoxycytidine Kinase Inhibitors and Noninvasive in Vivo Evaluation Using Positron Emission Tomography. *J. Med. Chem.* **2013**, *17*, 6696-6708 (2013).
22. Nomme, J.; Li, Z.; Gipson, R. M.; Wang, J.; Armijo, A. L.; Le, T. M.; Poddar, S.; Smith, T.; Santarsiero, B. D.; Nguyen, H.; Czernin, J.; Alexandrova, A. N.; Jung, M. E.; Radu, C. G.;

Lavie, A. Structure-Guided Development of Deoxycytidine Kinase Inhibitors with Nanomolar Affinity and Improved Metabolic Stability. *J. Med. Chem.* **2014**, *22*, 9480-9494.

23. Gambhir, S. S. Molecular imaging of cancer with positron emission tomography. *Nat. Rev. Cancer* **2002**, *9*, 683-693.

24. Czernin, J.; Benz, M. R.; Allen-Auerbach, M. S. PET/CT imaging: The incremental value of assessing the glucose metabolic phenotype and the structure of cancers in a single examination. *Eur. J. Radiol.* **2010**, *3*, 470-480.

25. Hargreaves, R. J. The Role of Molecular Imaging in Drug Discovery and Development. *Clin. Pharmacol. Ther.* **2008**, *2*, 349-353.

26. Phelps, M. E. Positron emission tomography provides molecular imaging of biological processes. *Proc. Natl. Acad. Sci.* **2000**, *16*, 9226-9233.

27. Wagner, C. C.; Muller, M.; Lappin, G.; Langer, O. Positron emission tomography for use in microdosing studies. *Curr. Opin. Drug Discov. Devel.* **2008**, *1*, 104-110.

28. Kim, W.; Le, T. M.; Wei, L.; Poddar, S.; Bazzy, J. Wang, X.; Uong, N. T.; Abt, E.R. Capri, J. R.; Austin, W. R.; Van Valkenburgh, J. S.; Steele, D.; Gipson, R. M.; Slavik, R.; Cabebe, A. E.; Taechariyakul, T.; Yaghoubi, S. S.; Lee, J. T.; Sadeghi, S.; Lavie, A.; Faull, K. F.; Witte, O. N.; Donahue, T. R.; Phelps, M. E.; Herschman, H. R.; Herrmann, K.; Czernin, J.; Radu, C.G. [18F]CFA as a clinically translatable probe for PET imaging of deoxycytidine kinase activity. *Proc. Natl. Acad. Sci.* **2017**, *15*, 4027-4032.

29. Laing, R. E.; Walter, M. A.; Campbell, D. O.; Herschman, H. R.; Satyamurthy, N.; Phelphs, M. E.; Czernin, J.; Witte, O. N.; Radu, C. G. Noninvasive prediction of tumor responses to gemcitabine using positron emission tomography. *Proc. Natl. Acad. Sci.* **2009**, *8*, 2847-2852.

30. Radu, C. G.; Shu, C. J.; Nair-Gill, E.; Shelly, S. M.; Barrio, J. R.; Satyamurthy, N.; Phelps, M. E.; Witte, O. N. Molecular imaging of lymphoid organs and immune activation by positron emission tomography with a new [18F]-labeled 2′-deoxycytidine analog. *Nat. Med.* **2008**, *7*, 783-788.

31. Tzara, A.; Xanthopoulos, D.; Kourounakis, A. P. Morpholine As a Scaffold in Medicinal Chemistry: An Update on Synthetic Strategies. *Chem. Med. Chem.* **2020**, *5*, 392-403.

32. Gobburu, J. V.; Jusko, W. J. Role of dosage regimen in controlling indirect pharmacodynamic responses. *Adv. Drug Deliv. Rev.* **2001**, *46*, 45-57.

33. Matthews, P. M.; Rabiner, E. A.; Passchier, J.; Gunn, R. N. Positron emission tomography molecular imaging for drug development: PET for drug development. *Br. J. Clin. Pharmacol.* **2012**, *2*, 175-186.

34. 18F-Clofarabine PET/CT in Imaging Cancer Patients Before and After Interventions. *https://clinicaltrials.gov/ct2/show/NCT02888301* (2020).

35. Valkenburgh, J. V. Development of Small-Molecule Modulators of Nucleotide Metabolism Enzymes. [Doctoral dissertation, University of California, Los Angeles], **2019**.

36. Nomme, J.; Murphy, J. M.; Su, Y.; Sansone, N. D.; Armijo, A. L.; Olson, S. T.; Radu, C. G.; Lavie, A. Structural characterization of new deoxycytidine kinase inhibitors rationalizes the affinity-determining moieties of the molecules. *Acta. Crystallogr. D. Biol. Crystallogr.* **2014**, *1*, 68-78.

37. Lipinski, C. A.; Lombardo, F.; Dominy, B. W.; Feeney, P. J. Experimental and computational approaches to estimate solubility and permeability in drug discovery and development settings. *Adv. Drug. Deliv. Rev.* **2001**, *1–3*, 3-26.

38. Benet, L. Z.; Hosey, C. M.; Ursu, O.; Oprea, T. I. BDDCS, the Rule of 5 and drugability. *Adv. Drug Deliv. Rev.* **2016**, *101*, 89-98.

39. Poddar, S.; Capparelli, E. V.; Rosser, E. W.; Gipson, R. M.; Wei, L.; Le, T. M.; Jung, M. E.; Radu, C. R.; Nikanjam, M. Development and preclinical pharmacology of a novel dCK inhibitor, DI-87. *Biochem. Pharmacol.* **2020**, *172*, 113742.

40. Creary, X.; Zhu, C.; Jiang, Z. Carbocations in the β-Lactam and β-Thiolactam Series. *J. Am. Chem. Soc.* **1996**, *49*, 12331-12338.

41. Kornblum, N. D.; Thomas M.; Earl, G. W.; Holy, N. L.; Kerber, R. C.; Musser, M. T.; Snow, D. H. New and facile substitution reactions at tertiary carbon. *J. Am. Chem. Soc.* **1967**, *3*, 727.

42. Hiroyoshi, H.; Ingaki, M.; Kawamato, S.; Sasaki, Y. Isoquinolinesulfonamides, Novel and Potent Inhibitors of Cyclic Nucleotide Dependent Protein Kinase and Protein Kinase C. *Biochemistry* **1984**, *23*, 5036-5041.

43. Zhang, J.; Yang, P. L.; Gray, N. S. Targeting cancer with small molecule kinase inhibitors. *Nat. Rev. Cancer* **2009**, *9*, 28-39.

44. Gross, S.; Rahal, R.; Stransky, N.; Lengauer, C.; Hoeflich, K. P. Targeting cancer with kinase inhibitors. *J. Clin. Invest.* **2015**, *5*, 1780-1789.

45. Manning, G.; Whyte, D. B.; Martinez, R., Hunter, T.; Sudarsanam, S. The protein kinase complement of the human genome. *Science* **2002**, *5600*, 1912-1934.

46. Traxler, P.; Furet, P. Strategies toward the design of novel and selective protein tyrosine kinase inhibitors. *Pharmacol. Ther.* **1999**, *2–3*, 195-206.

47. Abt, E. R.; Rosser, E. W.; Durst, M. A.; Lok, V.; Poddar, S.; Le, T. M.; Cho, A.; Kim, W.; Wei, L.; Song, J.; Capri, J. R.; Xu, S.; Wu, N.; Slavik, R.; Jung, M. E.; Damoiseaux, R.;

Czernin, J.; Donahue, T. R.; Lavie, A.; Radu, C. G. Metabolic Modifier Screen Reveals Secondary Targets of Protein Kinase Inhibitors within Nucleotide Metabolism. *Cell Chem. Biol*. **2020**, *2*, 197-205.

48. Fernandez-Banet, J.; Esposito, A. Coffin, S.; Horvath, I. B.; Estrella, H.; Schefzick, S.; Deng, S.; Wang, K.; AChing, K.; Ding, Y.; Roberts, P.; Rejito, P. A.; Kan, Z. OASIS: web-based platform for exploring cancer multi-omics data. *Nat. Methods* **2016**, *1*, 8-9.

49. Van Rompay, A. R.; Norda, A.; Linden, K.; Johansson, M.; Karlsson, A. Phosphorylation of Uridine and Cytidine Nucleoside Analogs by Two Human Uridine-Cytidine Kinases. *Mol. Pharmacol*. **2001**, *59*, 1181-1186 (2001).

50. Peters, G. J.; Smid, K.; Vecchi, L.; Kathmann, L.; Sarkisjan, D.; Honeywell, R. J.; Losekoot, N.; Ohne, O.; Orbach, A.; Blaugrund, E.; Jeong, L. S.; Lee, Y. B.; Ahn, C.; Kim, D. J. Metabolism, mechanism of action and sensitivity profile of fluorocyclopentenylcytosine (RX-3117; TV-1360). *Invest. New Drugs* **2013**, *6*, 1444-1457.

51. Siegel, R. L.; Miller, K. D.; Jemal, A. Cancer Statistics, 2020. *CA. Cancer J. Clin*. **2020**, *1*, 7-30.

52. Derle, A.; De Santis, M. C.; Gozzelino, L.; Ratto, E.; Martini, M. The role of metabolic adaptation to nutrient stress in pancreatic cancer. *Cell Stress* **2018**, *12*, 332-339.

53. Bryant, K. L.; Mancias, J. D.; Kimmelman, A. C.; Der, C. J. KRAS: feeding pancreatic cancer proliferation. *Trends Biochem. Sci*. **2014**, *2*, 91-100.

54. Vanzo, R.;, Bartkova, J.; Merchut-Maya, J. M.; Hall, A.; Bouchal, J.; Dyrskjot, L.; Frankel, L. B.; Gorgoulis, V.; Maya-Mendoza, A.; Jaattela, M.; Bartek, J. Autophagy role(s) in response to oncogenes and DNA replication stress. *Cell Death Differ.* **2020**, *3*, 1134-1153.

55. Terai, C.; Wasson, D. B.; Carrera, C. J.; Carson, D. A. Dependence of cell survival on DNA repair in human mononuclear phagocytes. *J. Immunol.* **1991**, *12*, 4302-4306.

56. Huang, S.; Li, J.; Tam, N. L.; Sun, C.; Hou, Y.; Hughes, B.; Wang, Z.; Zhou, Q.; He, X.; Wu, L. Uridine-cytidine kinase 2 upregulation predicts poor prognosis of hepatocellular carcinoma and is associated with cancer aggressiveness. *Mol. Carcinog.* **2019**, *4*, 603-615.

57. Lim, M.; Moyer, J. D.; Cysyk, R. L.; Marquez, V. E. Cyclopentenyluridine and Cyclopentenylcytidine Analogues as Inhibitors of Uridine-Cytidine Kinase. *J. Med. Chem.* **1984**, *12*, 1536-1538.

58. Cysyk, R. L.; Malinowski, N.; Marquez, V.; Zaharevitz, D.; August, E. M.; Moyer, J. D. Cyclopentenyl Uracil: An Effective Inhibitor of Uridine Salvage In Vivo. *Biochem. Pharmacol.* **1995**, *2*, 203-207.

59. White, R. M.; Cech, J.; Ratanasirintrawoot, S.; Lin, C. Y.; Rahl, P. B.; Burke, C. J.; Langdon, E.; Tomlinson, M. L.; Mosher, J.; Kaufman, C.; Chen, F.; Long, H. K.; Kramer, M.; Datta, S.; Neuberg, D.; Granter, S.; Young, R. A.; Morrison, S.; Wheeler, G. N.; Zon, L. I. DHODH modulates transcriptional elongation in the neural crest and melanoma. *Nature* **2011**, *7339*, 518-522.

60. McLean, J. E.; Neidhardt, E. A.; Grossman, T. H.; Hedstrom, L. Multiple inhibitor analysis of the brequinar and leflunomide binding sites on human dihydroorotate dehydrogenase. *Biochemistry* **2001**, *7*, 2194-2200.

61. Munier-Lehmann, H.; Vidalain, P. O.; Tangy, F.; Janin, Y. L. On dihydroorotate dehydrogenases and their inhibitors and uses. *J. Med. Chem.* **2013**, *8*, 3148-3167.

62. Le, T. M.; Poddar, S.; Capri, J. R.; Abt, E. R.; Kim, W.; Wei, L.; Uong, N. T.; Cheng, C. M.; Braas, D.; Nikanjam, M.; Rix, P.; Merkurjev, D.; Zaretsky, J.; Kornblum, H. I.; Ribas, A.;

Herschman, H. R.; Whitelegge, J.; Faull, K. F.; Donahue, T. R.; Czernin, J.; Radu, C. G. ATR inhibition facilitates targeting of leukemia dependence on convergent nucleotide biosynthetic pathways. *Nat. Commun.* **2017**, *5600*, 1912-1934.

63. Shu, C.J.;Campbell, D. O.; Lee, J. T.; Tran, A. Q.; Wengrod, J. C.; Witte, O. N.; Phelps, M. E.; Satyamurthy, N.; Czernin, J.; Radu, C. G. Novel PET probes specific for deoxycytidine kinase. *J. Nucl. Med.* **2010**, *7*, 1092–1098.

64. Upton, R. N.; Mould, D. R. Basic concepts in population modeling, simulation, and model-based drug development: part 3-introduction to pharmacodynamic modeling methods, *CPT Pharmacometrics Syst. Pharmacol.* **2014**, *1*, e88.

CHAPTER TWO

Identification of Small Molecule Modulators of Pyrimidine Nucleotide Metabolism

Adapted from: Evan R. Abt*, Ethan W. Rosser*, Matthew A. Durst*, Soumya Poddar, Vincent Lok, Liu Wei, Woosuk Kim, Janet Song, Joseph R. Capri, Thuc M. Le, Roger Slavik, Michael E. Jung, Robert Damoiseaux, Johannes Czernin, Timothy R. Donahue, Arnon Lavie, Caius G. Radu. *Cell Chem Biol*. **2019**, 27(2), 197-205. (*These authors contributed equally).

2.1 Introduction

The redundant and plastic nature of metabolic networks represents a significant obstacle in the pharmacological targeting of cancer metabolism. This redundancy manifests in two ways, the first being the expression of multiple enzymes that perform ostensibly identical biochemical reactions, such as the hexokinase isozymes which each phosphorylate glucose.[1] The second is the existence of convergent metabolic pathways that produce a common metabolite from unique precursors. Generally, these parallel networks consist of *de novo* and scavenging pathways that synthesize or recycle (either from the extracellular environment or by breakdown of macromolecules) their common metabolite, respectively. Such convergent metabolic nodes have been noted in nucleotide,[2] lipid (cholesterol),[3] and amino acid (aspartate)[4] metabolism.

Despite these difficulties, the development of metabolism modifiers remains a robust area of research. One such therapeutically relevant target is pyrimidine nucleotide biosynthesis, which consists of nucleoside salvage (NSP) and *de novo* (DNP) pathways that converge to generate uridine monophosphate (UMP), the common precursor for all pyrimidine nucleotides.[5] The NSP

allows for the scavenging of uridine from the extracellular environment, shuttling it into the cell *via* nucleoside transporters where it is phosphorylated by uridine-cytidine kinases (UCKs) to produce UMP. UCK2 is thought to be the primary NSP kinase, given its 20-fold higher catalytic efficiency compared to UCK1.[6] The DNP is a six-step process that utilizes glutamine, aspartate, bicarbonate, and glucose to produce UMP through the action of three enzymes: trifunctional CAD, electron transport chain-linked dihydroorotate dehydrogenase (DHODH), and bifunctional UMP synthase (UMPS). Among the DNP enzymes, DHODH in particular has emerged as a therapeutic target in multiple cancers including pancreatic ductal adenocarcinoma (PDAC).[7–9] Additionally, over 90 patent applications involving DHODH inhibition have been filed in the last decade.[10]

In this study, we show that the pyrimidine NSP and DNP are interchangeable in their ability to sustain cancer cell proliferation and that a synthetic lethal phenotype can be achieved through their simultaneous inhibition. We leverage this observation to construct a metabolic modifier screen that allows for the identification of selective modulators of NSP and DNP pathways. In screening a library of protein kinase inhibitors, we identified multiple compounds with previously uncharacterized nucleotide metabolism-modifying activity. We show that the c-Jun N-terminal kinase (JNK) inhibitor JNK-IN-8 is a potent inhibitor of uridine transport which is vital for NSP function, and that the 3-phosphoinositide-dependent protein kinase 1 (PDK1) inhibitor OSU-03012 (also known as AR-12) and the pan-RAF inhibitor TAK-632 both bind and inhibit the pyrimidine DNP enzyme DHODH.

2.2 Design of a Differential Metabolic Modifier Screen for Identification of Novel Modulators of Pyrimidine Nucleotide Metabolism

While the UMP-DNP and -NSP are interchangeable in their ability to sustain cell proliferation, their relative activity at baseline (when both pathways are functional) is poorly defined. *De novo* pyrimidine biosynthesis is allosterically inactivated by its end product, UTP, which is also produced by the uridine (rU) NSP.[12] This allosteric control functions at the level of the CPSase activity of the trifunctional protein CAD, which performs the first committed step in *de novo* pyrimidine biosynthesis (**Figure S2.1A**). To quantitatively evaluate the discrete activities of the pyrimidine *de novo* and salvage pathways, we modified and applied a LC-MS/MS assay previously used by our group to track the contribution of stable isotope-labeled glucose and deoxycytidine to newly replicated DNA.[2] In this assay, cells are cultured in the presence of [$^{13}C_6$]glucose (to track DNP activity) and 10 μM [$^{13}C_9$; $^{15}N_2$]rU (to track NSP activity). Their DNA is then extracted and hydrolyzed and the abundance of stable isotope-labeled nucleosides is evaluated using LC-MS/MS in the multiple reaction monitoring (MRM) mode (**Figure S2.1B**). We applied this assay to a panel of cancer cell lines and observed a heterogenous degree of total labeling ([$^{13}C_6$]glucose + [$^{13}C_9$; $^{15}N_2$]rU) in the deoxycytidine compartment of DNA (DNA-C) after 24 hr (**Figure S2.1C**). Consistent with the aforementioned model in which UTP produced by uridine savage allosterically impairs *de novo* biosynthesis, we found that the fractional contribution of [$^{13}C_9$; $^{15}N_2$]rU exceeded that of [$^{13}C_6$]glucose in all models tested (**Figure S2.1D**). Interestingly, we found heterogeneity in the relative contribution of [$^{13}C_6$]glucose and [$^{13}C_9$; $^{15}N_2$]rU to DNA-C across the cell line panel, which likely reflects

differential expression or regulation of the various transporters, kinases, nucleotidases, and phosphorylases involved in rU salvage. Importantly, we confirmed that the contribution of [$^{13}C_6$]glucose to DNA-C could be blocked by NITD-982, an established DHODH inhibitor, and likewise the contribution of [$^{13}C_9$; $^{15}N_2$]rU could be prevented by the FDA-approved nucleoside transport inhibitor dipyridamole (DPA) (**Figure S2.1E**). Collectively, these results indicate that, under the conditions tested, both the UMP-DNP and -NSP pathways are simultaneously, but not equally, active.

Although redundant routes for UMP biosynthesis can complicate targeting, impaired cellular proliferation resulting from simultaneous restriction of both *de novo* (DNP) and salvage (NSP) pathways can be leveraged for the identification of selective DNP or NSP activity modifiers (**Figure S2.1F**). A metabolic modifier screen was developed for the discovery of small molecule modulators of UMP production by leveraging this biosynthetic redundancy. This cell-based platform concurrently tests the effects of small molecule compounds on the proliferation of cells cultured in baseline (both NSP and DNP active), NSP-only, and DNP-only conditions (**Figure 2.1A**). Baseline conditions were those in which cells were incubated in standard media supplemented with physiological levels of uridine. To promote DNP-only conditions, cells were grown in standard media without uridine, effectively abrogating the activity of the NSP and forcing cells to rely upon the DNP for UMP production. To achieve NSP-only conditions, cells were incubated in standard media with physiological levels of uridine in the presence of NITD-982, a potent and selective small molecule inhibitor of DHODH which prevents the DNP-synthesis of pyrimidine nucleotides.[11] Compounds which inhibit proliferation in baseline conditions are classified as non-specific inhibitors, those which inhibit proliferation in NSP-only

conditions are NSP inhibitors, while those that inhibit growth in DNP-only conditions are DNP inhibitors. The screen design was validated using NITD-982 and the FDA-approved nucleoside transport inhibitor dipyridamole (DPA), with Cell Titer Glo (CTG) utilized to evaluate proliferation impairment (**Figure S2.1G**).[11]

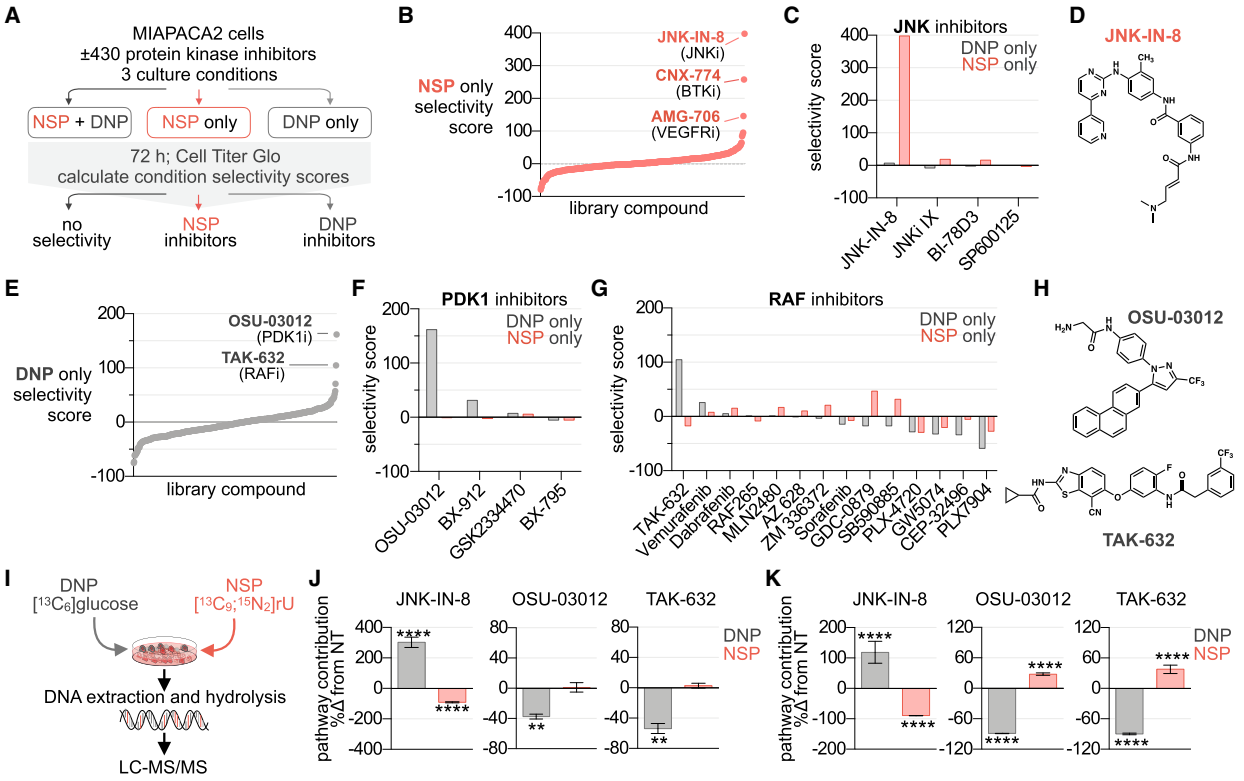

Figure 2.1 | Identification of nucleotide metabolism modulators in a small molecule protein kinase inhibitor library. (A) Phenotypic screening strategy. The impact of 430 protein kinase inhibitors on cell proliferation was evaluated in MIAPACA2 cells plated in 3 distinct culture conditions; 1) NSP + DNP (media +10 μM uridine (rU)); 2) NSP only (media +10 μM rU +1 μM NITD-982); or 3) DNP only (media alone). % proliferation values were calculated using Cell Titer Glo (CTG) following 72 hr treatment (7-point dose response; n=2). (B) Waterfall plot ranking library compounds based on NSP pathway selectivity score. (C) Summary of NSP and

DNP selectivity scores across library compounds annotated as JNK inhibitors. (D) Structure of JNK-IN-8. (E) Waterfall plot ranking library compounds based on DNP pathway selectivity score. (F,G) Summary of NSP and DNP selectivity scores across library compounds annotated as PDK1 (F) or RAF inhibitors (G). (H) Structures OSU-03012 and TAK-632. (I) Experimental design to track contribution of UMP-DNP and -NSP to newly replicated DNA using stable isotope-labeled metabolite tracers. (J,K) LC-MS/MS analysis of [$^{13}C_6$]glucose (5.5 mM) and [$^{13}C_9$; $^{15}N_2$] rU (10 μM) utilization for DNA-C replication in MIAPACA2 (J) or JURKAT (K) cells treated +1 μM JNK-IN-8 +5 μM OSU-03012 or +5 μM TAK-632 for 24 hr (NT: not-treated; mean±SD; n=3; unpaired T-test; ** $P < 0.01$, **** $P < 0.0001$).

Cancer cell lines exhibited varying degrees of sensitivity to DHODH inhibition (as determined by doubling-time-normalized proliferation inhibition) and were all rescued by rU supplementation (**Figure S2.2**).[13] MIAPACA2 PDAC cells were utilized for the screen due to their ability to maintain baseline proliferation levels in NSP-only or DNP-only conditions, while also exhibiting a significant decrease in proliferation upon simultaneous NSP and DNP inhibition (**Figure S2.3A**). A library of 430 protein kinase inhibitors was chosen for evaluation, the rationale being twofold. First, it was hypothesized that our synthetic lethality screen may identify compounds that indirectly target pyrimidine metabolism through regulatory signal transduction pathway inhibition. Second, because a substantial fraction of kinase inhibitors are ATP-mimetics and therefore resemble nucleotides, we predicted that protein kinase inhibitors may possess secondary, non-canonical targets within nucleotide metabolism. Consistently, several protein kinase inhibitors, specifically those exhibiting similarities with imatinib's phenylamino pyrimidine (PAP) scaffold, and a subset of p38 MAPK inhibitors, exhibit activity against

nucleoside transporters.[14,15] This kinase inhibitor library was screened at 7-point dose response in duplicate. Composite NSP and DNP pathway selectivity scores were calculated for each compound as the sum of condition-specific anti-proliferative effects across the dose range (**Figure S2.3B**). Phenotypic screen quality was monitored using the Z-factor metric (**Figure S2.3C**)[16].

The JNK inhibitor JNK-IN-8, the BTK inhibitor CNX-774, and the VEGFR inhibitor AMG-706 were active in the NSP-only condition, exhibiting positive NSP-selectivity scores (**Figure 2.1B**). The selectivity of these hits for the NSP was unique among inhibitors of JNK (**Figures 2.1C, 2.1D**), BTK, and VEGFR (**Figures S2.3D–F**), indicating this phenotype likely did not result from on-target effects. The PDK1 inhibitor OSU-03012 (also known as AR-12) and the pan-RAF inhibitor TAK-632 elicited potent and selective inhibition of proliferation in the DNP-only condition (**Figure 2.1E**).[17,18] Among the four PDK1 inhibitors and 14 RAF inhibitors tested, OSU-03012 and TAK-632 were unique in their ability to selectively inhibit the DNP, again suggesting that this effect was not the consequence of on-target activity (**Figures 2.1F–H**).

Microplate immunofluorescence microscopy nuclei scoring analysis of MIAPACA2 cells stained with Hoechst 33342 was performed as an orthogonal approach. These studies confirmed the culture-condition selectivity of our hits and validated the results of the CTG-based screen (**Figures S2.3G, S2.3H**). Additionally, we performed CTG analysis and trypan-blue exclusion cell scoring in a second cancer cell line, JURKAT, to confirm hit selectivity (**Figure S2.3I, S2.3J**).

In addition to its non-redundant role in *de novo* pyrimidine nucleotide biosynthesis, DHODH functions as an electron donor in the mitochondrial electron transport chain.[19] To

exclude the possibility that the selective activity of JNK-IN-8 reflects an interaction with NITD-982 at the level of electron transport chain modulation, we synthesized and evaluated N-phosphonacetyl-L-aspartate (PALA), an inhibitor of CAD which functions upstream of DHODH.[20,21] We determined that JNK-IN-8 inhibits JURKAT cell proliferation when both PALA and rU are present in the culture media, supporting that its selective activity results from the inhibition of uridine salvage (**Figure S2.4A**).

We next applied our LC-MS/MS stable isotope tracking approach to evaluate the impact of JNK-IN-8, OSU-03012, and TAK-632 on the incorporation of [$^{13}C_6$]glucose and [$^{13}C_9$; $^{15}N_2$]rU into newly replicated DNA (**Figure 2.1I**). In MIAPACA2 cells, we found that JNK-IN-8 blocked the NSP contribution while triggering a compensatory upregulation of the DNP. Conversely, OSU-03012 and TAK-632 selectively impaired DNP contribution (**Figure 2.1J**). Similar selectivity was observed in JURKAT cells, where both OSU-03012 and TAK-632 blocked DNP contribution while inducing compensatory up-regulation of the NSP (**Figure 2.1K**).

2.3 JNK-IN-8 Inhibits Nucleoside Uptake

While three protein kinase inhibitors were identified as selective inhibitors of the pyrimidine NSP, the JNK inhibitor JNK-IN-8 was exceptionally potent, with IC_{50} values in the low nanomolar range. We reasoned that the activity of JNK-IN-8 could arise from either the inhibition of nucleoside shuttling across the plasma membrane, which is achieved by nucleoside transporters, or through the inhibition of nucleoside phosphorylation by nucleoside kinases. To determine the level at which JNK-IN-8 is active, we determined the effects of JNK-IN-8 upon

the uptake of a panel of ^{3}H-labeled purine (dA, dG) and pyrimidine nucleosides (rU, dC) in MIAPACA2 cells. These nucleosides rely upon the same nucleoside transporters to enter the cell but require unique kinases for conversion into their respective monophosphate forms and intracellular accumulation. UCKs are required for the phosphorylation of rU while deoxycytidine kinase (dCK) is required for the phosphorylation of both purine and pyrimidine deoxyribonucleosides including dC, dA, and dG (**Figure 2.2A**).[2]

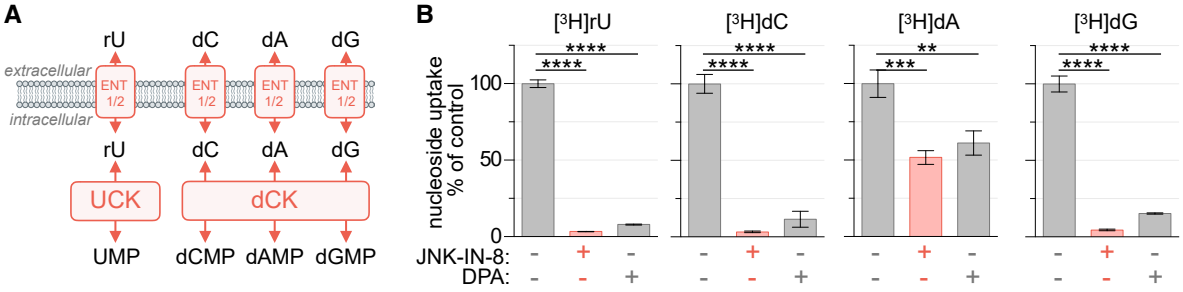

Figure 2.2 | JNK-IN-8 inhibits nucleoside uptake. (**A**) Uridine salvage pathway activity can be prevented by inhibition of either nucleoside transporters or kinases. (**B**) Uptake of [^{3}H]rU, [^{3}H]dC, [^{3}H]dA (+10 μM dCF) and [^{3}H]dG (+1 μM BCX-1777) in MIAPACA2 cells following 2 hr incubation ± 1 μM JNK-IN-8 or 1 μM dipyridamole (DPA; 18.5 kBq; mean±SD; n=3; one-way ANOVA corrected for multiple comparisons by Bonferroni adjustment; ** P<0.01; *** P<0.001; **** P<0.0001).

We found that JNK-IN-8 prevented the uptake of all nucleosides tested, but exhibited greater potency toward rU and dC. Importantly, JNK-IN-8 exhibits a selectivity pattern similar to the established ENT1 inhibitor DPA (**Figure 2.2B**). We confirmed JNK-IN-8 inhibited the uptake of both rU and dC with similar potency (33 nM and 31 nM, respectively), further suggesting that the compound inhibits nucleoside transport (**Figure S2.4C**). Additionally, JNK-IN-8 treatment prevented the anti-proliferative effects of gemcitabine (dFdC), a dCK-dependent nucleoside

analog prodrug which relies upon nucleoside transporters for its activation, in a dose-dependent manner (**Figure S2.4D**).[22] A similar pattern of dA, dG, rU and dC uptake inhibition by JNK-IN-8 and DPA was observed in a second cell line, the murine pancreatic cancer model KP4662 (**Figures S2.4E, S2.4F**).[23]

Seven nucleoside transporters have been described and categorized into two families. Concentrative nucleoside transporters (CNT1-3; SLC28A1-3) are unidirectional inward transporters which co-transport Na^+. Equilibrative nucleoside transporters (ENT1-4; SLC29A1-4) are bidirectional, energy-independent, and accept a broad range of purine and pyrimidine nucleosides and nucleoside analogs.[24] We evaluated the expression of these transporters in MIAPACA2 and JURKAT cells and found that ENT1 (SLC29A1) is the predominantly expressed transporter in both models (**Figure S2.4G**).[25] ENT1 is an established transporter of a variety of nucleosides including natural purines and pyrimidines as well as therapeutic analogs such as gemcitabine.[24] We next utilized a cellular thermal shift assay (CETSA), an approach that leverages the altered thermostability of proteins following ligand binding, to confirm ENT1 engagement by JNK-IN-8 (**Figure S2.4H**).[26] The assay showed that upon incubation with JNK-IN-8, ENT1 demonstrated increased thermostability, relative to incubation with vehicle only. Collectively, these results indicate that JNK-IN-8 inhibits UMP-NSP activity by blocking ENT1 and interfering with the transport of rU.

2.4 OSU-03012 and TAK-632 Target *de novo* UMP Biosynthesis and Activate the DNA Replication Response Pathway

Two protein kinase inhibitors, TAK-632 and OSU-03012, were identified as potent and selective inhibitors of MIAPACA2 proliferation in the DNP-only culture condition (**Figure 2.1E**). We reasoned that these compounds could inhibit *de novo* pyrimidine biosynthesis by targeting either CAD, DHODH, or UMPS – the three enzymes essential for the six-step *de novo* biosynthesis of UMP (**Figure 2.3A**). Both OSU-03012 and TAK-632 induced S-phase arrest in MIAPACA2 cells cultured in the DNP-only condition (**Figure 2.3B**). S-phase arrest is a phenotype associated with dNTP biosynthesis levels insufficient to sustain DNA replication, and is the result of activation of intra-S-phase cell cycle signaling checkpoints. This effect was rescued by orotate (the product of DHODH) supplementation and could be completely reversed by rU supplementation (**Figures 2.3B, 2.3C**). These data implicated DHODH as a likely target of both OSU-03012 and TAK-632. DHODH catalyzes one of three committed steps within the UMP-DNP and is an established druggable protein.[7] In addition, both OSU-03012 and TAK-632 possess fluorine substituents, which have been shown to stabilize bioactive conformations of DHODH inhibitors within the ubiquinone transport tunnel of the protein.[27,28] In an *in vitro* colorimetric recombinant human DHODH activity assay, TAK-632 and OSU-03012 both inhibited DHODH activity in a dose-dependent manner (**Figure 2.3D**).[28] Additionally, the response to TAK-632 or OSU-03012 correlated with the response to a known DHODH inhibitor in a panel of 25 pancreatic cancer cell lines (**Figure 2.3E**).

OSU-03012 was recently reported to synergize with replication stress response kinase inhibitors in RSK-subtype mutant KRAS cancer models.[29] However, after confirming that

OSU-03012 binds DHODH, we hypothesized that the observed synergy resulted from DHODH inhibition rather than from inhibition of PDK1, the canonical target of OSU-03012. Immunoblot analysis of S6K and S6 phosphorylation, PDK1 downstream targets, confirmed that the known PDK1 inhibitor GSK-2334470 potently blocked PDK1 while OSU-03012 triggered S345 CHEK1 phosphorylation, a replication stress biomarker, only in the absence of rU (**Figure 2.3F**). Similarly, TAK-632 only triggered CHEK1 phosphorylation in the absence of rU whereas an established pan-RAF inhibitor which does not exhibit paradoxical RAF activation, LY3009120, down-regulated ERK1/2 phosphorylation but had no impact on CHEK1 phosphorylation (**Figure 2.3G**).[30] Consistently, we found that neither GSK-2334470 nor LY3009120 induced S-phase arrest at doses where we observed down-regulation of their target substrates, whereas a known DHODH inhibitor induced potent S-phase accumulation that was completely reversed by rU supplementation (**Figures S2.4I, S2.4J**).

To complement our evaluation of replication stress response biomarker induction, we performed an assessment of DNA damage induced by OSU-03012, TAK-632, and the ATR inhibitor VE-822 as a positive control using γ-H2A.X flow cytometry. We found that while OSU-03012 and TAK-632 trigger activation of the replication stress response, they do not significantly induce γ-H2A.X. We hypothesize that activation of the replication stress response pathway by OSU-03012 or TAK-632 limits DNA double-strand breaks by preventing the collapse of stalled replication forks (**Figure S2.4K**).[31]

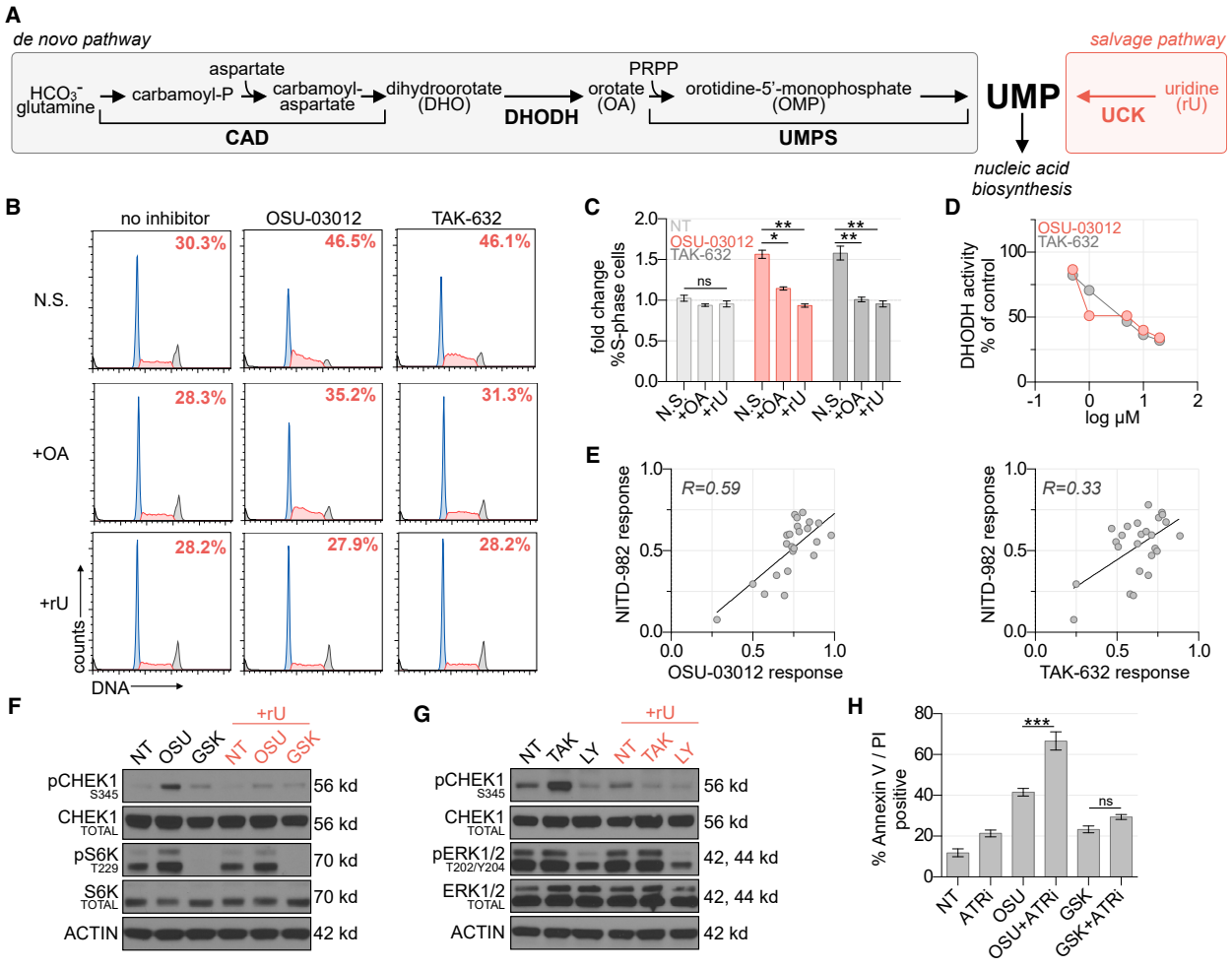

Figure 2.3 | OSU-03012 and TAK-632 inhibit DHODH and activate the DNA replication stress response pathway. (**A**) Schematic of UMP biosynthesis *via* the *de novo* and salvage pathways. (**B**) Propidium iodide cell cycle analysis of MIAPACA2 PDAC cells treated ± 5 μM TAK-632 or ± 5 μM OSU-03012 and supplemented with 50 μM orotate (OA) or 10 μM rU (N.S.: no supplement). Insert indicates % S-phase cells. (**C**) Summary of fold changes in S-phase cells from **B** (mean±SD; n=2; one-way ANOVA corrected for multiple comparisons by Bonferroni adjustment, ns: not significant; * P<0.05; ** P<0.01). (**D**) *in vitro* DHODH enzyme assay performed in the presence of OSU-03012 or TAK-632. (**E**) Correlation between DHODH inhibitor (1 μM NITD-982) and OSU-03012 (3.17 μM) or TAK-632 (3.17 μM) response across a panel of 25 PDAC cell lines determined using CTG following 72 hr treatment. Response

calculated as doubling time normalized proliferation inhibition. Pearson correlation coefficient is indicated. (**F**) Immunoblot analysis of MIAPACA2 cells treated ± 1 μM PDK1 inhibitor GSK-2334470 (GSK) ± 1 μM OSU-03012 (OSU) ± 10 μM rU for 24 h. (**G**) Immunoblot analysis of MIAPACA2 cells treated ± 10 μM RAF inhibitor LY3009120 (LY) ± 10 μM TAK-632 (TAK) ± 10 μM rU for 24 h. (**H**) Annexin V/PI flow cytometry analysis of MIAPACA2 PDAC cells treated ± 1 μM OSU-03012 or 1 μM GSK-2334470 (GSK) ± 500 nM VE-822 (ATRi) ± 25 μM rU for 72 hr (mean ± SD; n=2; one-way ANOVA corrected for multiple comparisons by Bonferroni adjustment; ns: not significant; ** P<0.01; *** P<0.001).

To investigate the interaction between OSU-03012 and replication stress response inhibitors, we treated MIAPACA2 cells with VE-822, an inhibitor of the proximal replication stress response kinase ATR, and either OSU-03012 or GSK-2334470 for 72 hr. A synergistic increase in cell death was observed when OSU-03012 and the ATR inhibitor were combined, whereas the combination of potent PDK1 inhibitor GSK-2334470 and VE-822 demonstrated only a nominal increase in cell death as determined by AnnexinV/PI flow cytometry (**Figure 2.3H**). Taken together, these data indicate that replication stress triggered by OSU-03012 is the consequence of DHODH inhibition rather than inhibition of its canonical target PDK1.

2.5 Co-Crystal Structures of OSU-03012 and TAK-632 in Complex with Human DHODH

To determine the molecular interactions between the protein and its putative inhibitors, complete DHODH co-crystallization data sets were obtained and processed to 1.4 Å and 2.7 Å for OSU-03012 and TAK-632, respectively (**Table S2.1**).[28] Both compounds bind in a hydrophobic channel composed by two N-domain α-helices through which ubiquinone travels, a mechanism consistent with previously identified DHODH inhibitors. A long-range hydrogen

bond between Arg 69 and OSU-03012 helps orient the molecule to the hydrophobic pocket where the phenanthrene moiety inserts, while the remainder of the molecule lies on the outer surface of DHODH, blocking the hydrophobic channel (**Figures 2.4A, S2.4A**). Three hydrogen bonds stabilize TAK-632 in the same hydrophobic pocket: two with Tyr 37 and Leu 66 help stabilize the inhibitor at the opening of the channel, while a third with Gln 46 helps pull the inhibitor deep into the pocket (**Figures 42.B, S2.4B**).

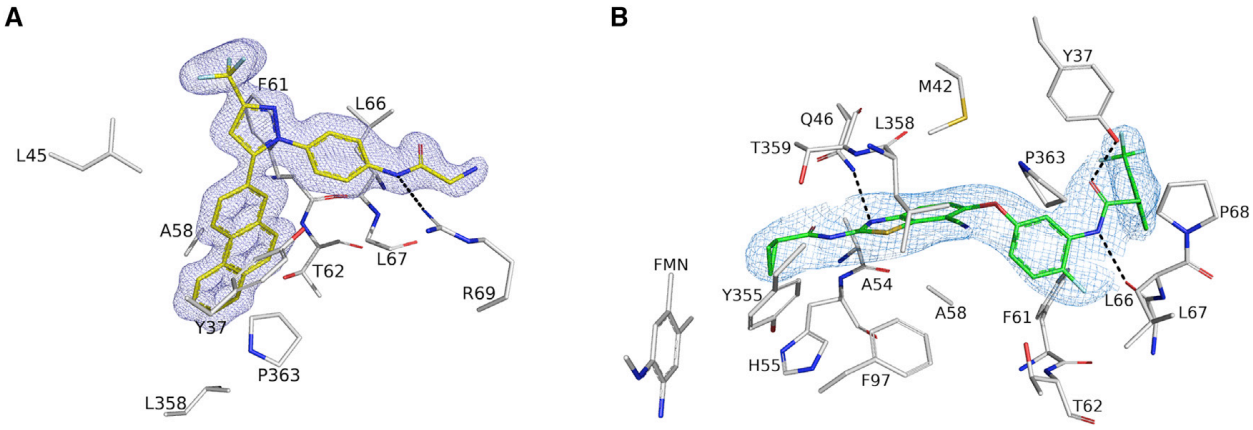

Figure 2.4 | OSU-03012 and TAK-632 bind DHODH. (**A, B**) Crystal Structure of DHODH with compounds OSU-03012 (**A**) or TAK-632 (**B**). 2mFo-DFc electron density for OSU-03012 (carbons in yellow) or TAK-632 (carbons in green) contoured at 1 σ. Dashed black lines represent hydrogen bonds between DHODH and its ligands. Interacting residues as predicted by LigPlot+ are shown and labeled.

2.6 Discussion

Our screening strategy expands upon previously described "nutrient-sensitized" genetic and small molecule cell-based screening approaches that leveraged the production of a proliferation-enabling metabolite by parallel and redundant metabolic networks to identify selective metabolism modifiers.[32,33] UMP biosynthesis (i.e. pyrimidine metabolism) proved to be

compatible with this screening framework, as UMP is produced by convergent (*de novo* and salvage) pathways, and UMP depletion triggers a quantifiable change in cellular proliferation.

JNK-IN-8, developed as an irreversible inhibitor of c-Jun N-terminal kinases 1, 2, and 3 with low-nanomolar affinity, was the most potent of three uridine salvage inhibitors identified in our study.[34] Our data confirm that JNK-IN-8 also functions as a potent inhibitor of uridine and deoxycytidine transport and engages the nucleoside transporter SLC29A1 (ENT1). We conclude that JNK-IN-8 should not be used in conjunction with compounds which rely upon nucleoside transport, such as the anticancer agent gemcitabine, in research or therapy settings. JNK-IN-8 was synthesized by the Gray group at the Dana Farber Cancer Institute as part of series of molecules for targeting JNK. We have started a collaboration with their group and are currently identifying additional compounds within their chemical library which possess ENT1-inhibiting ability.

In addition to their role in pyrimidine salvage, equilibrative nucleoside transporters are well studied for their ability to regulate levels of the immuno-modulatory metabolite adenosine. ENT1 inhibitors increase extracellular adenosine levels which signal through the P1 purinergic receptor and are used clinically for the treatment of hypertension, among other disorders.[35] ENT1 inhibitors have been shown to increase vasodilation and can exert cardioprotective effects upon ischemic cardiovascular tissue.[34] Additionally, due to the immunosuppressive effects of increased extracellular adenosine levels, ENT1 inhibitors could find utility in mitigating excessive late-stage immune responses which contribute to dangerous pathology related to cytokine storms and acute respiratory distress syndrome. Given the prevalence of these conditions in influence and the current COVID-19 pandemics, these therapeutic considerations

are particularly intriguing.[34] Thus, the development of potent and selective inhibitors of ENT1 is an active area of investigation with opportunity for clinical application.

The recently reported co-crystal structure of ENT1 in complex with two small molecule inhibitors (NBMPR and dilazep) provided new insight into the molecular mechanism of nucleoside transport and suggested that structurally diverse ENT1 inhibitors possess unique modes of inhibition.[36] ENT1 contains ten cysteine residues and ENT1-mediated uridine transport can be inhibited by covalent modification of Cys416 by *N*-ethylmaleimide.[37] Intriguingly, the two highest scoring NSP inhibitors in our screen, JNK-IN-8 and the BTK inhibitor CNX-774, both contain a reactive acrylamide group and are cysteine-targeting drugs. Future work will explore the mechanism of ENT1 inhibition by JNK-IN-8 with a specific focus on the contribution of covalent interactions, with additional efforts focused upon decoupling JNK affinity from ENT1 inhibition.

Positron emission tomography (PET) imaging is a powerful approach to monitor cellular metabolism *in vivo,* and several nucleoside analog PET probes have been developed including both pyrimidine ([^{18}F]FAC, [^{18}F]FLT) and purine analogs ([^{18}F]CFA).[38–40] Interestingly, ENT1-knockout mice exhibit significantly higher plasma thymidine but also paradoxically higher levels of thymidine analog [^{18}F]FLT uptake in the spleen and bone marrow compared to wild type controls.[41] Discrepancies between *in vitro* and *in vivo* findings could result from shifts in nucleoside gradients or differential expression of nucleoside transporters mediated by factors absent from traditional cell culture systems. Future work will focus on

exploring the utility of nucleoside analog PET as a pharmacodynamic biomarker for ENT inhibitor activity *in vivo*.

The structurally and functionally unrelated OSU-03012 and TAK-632 were identified as inhibitors of the pyrimidine DNP. A recent report described the ability of OSU-03012 and analogs to inhibit virus propagation *via* pyrimidine nucleotide biosynthesis inhibition, specifically implicating modulation of DHODH activity.[42] Our work substantiates these findings and confirms engagement of DHODH by OSU-03012 and TAK-632 through crystallography studies. Notably, our studies show that OSU-03012 and TAK-632 bind in the same hydrophobic tunnel of DHODH as known inhibitors brequinar and teriflunomide (the active metabolite of leflunomide). This suggests that these two protein kinase inhibitors compete with ubiquinone, a redox partner of DHODH which traverses this hydrophobic tunnel to regenerate FMN from $FMNH_2$. By competitively inhibiting the binding of ubiquinone, these compounds prevent DHODH from completing its redox cycle and effectively abrogate its activity.

OSU-03012 has orphan drug designation in the European Union for treatment of tularaemia and cryptococcosis. We hypothesize that its effectiveness in these indications stems from its ability to inhibit DHODH, rather than from 'on-target' effects against PDK1. Indeed, DHODH inhibitors have demonstrated efficacy against viruses such as dengue virus and respiratory syncytial virus.[11,42,43] Our results should encourage the further study and application of OSU-03012, and DHODH inhibitors in general, in antimicrobial therapy. In anticancer settings, OSU-03012 was recently demonstrated to synergize with CHK1 inhibitors in KRAS-mutant cancers,[29] which was initially attributed to its ability to inhibit PDK1. However, our data show that GSK-2334470, a PDK1 inhibitor more potent than OSU-03012, displayed little

synergy with ATR inhibition. In light of this and our crystallographic data, we conclude that the synergy observed between OSU-03012 and ATR inhibition is likely a result of the DHODH-inhibitory ability of the former. Taken together, our data suggest that DHODH inhibitors may have utility in oncology, particularly if used in conjunction with ATR inhibitors or other DNA-damage response/replication stress response pathway inhibitors.[2]

While a small library of 430 protein kinase inhibitors was assessed in this study, the design of our screen allows for much larger high-throughput screening campaigns which could be utilized for identification of hit compounds with the ability to modulate pyrimidine nucleotide metabolism. This may be beneficial for research groups or pharmaceutical companies who wish to screen small-molecule libraries to identify new hit compounds, or could be used to characterize the "off-target" effects of existing drugs. The utility of characterizing a drug's effects upon pyrimidine nucleotide metabolism is high, as off-target effects within these pathways can lead to misattribution of beneficial activities. This is demonstrated by the attribution of OSU-03012-mediated PDK1 inhibition as synergizing with CHK1 inhibition – this conclusion was made without the knowledge of the DHODH-inhibiting ability of OSU-03012, and could have led researchers to spend precious resources studying this supposed link.

In summary, we designed and applied a metabolic modifier screen which identified multiple protein kinase inhibitors as having non-canonical targets within pyrimidine metabolism. Similarly constructed phenotypic screens designed against other metabolic networks containing convergent nodes may find use in drug discovery campaigns or in repurposing screens using existing compounds.

2.7 Experimental Section

2.7.1 Methods and Materials

Cell culture

All cell cultures were between passages 3 and 20 and maintained in antibiotic free DMEM or RPMI +10% dialyzed FBS, at 37ºC in 5% CO_2. We routinely monitored for mycoplasma contamination using the PCR-based Venor Mycoplasma kit. PDAC cell lines were acquired either from a commercial vendor (ATCC, DSMZ) or from collaborators (KP4662 from Dr. Vonderheide, UPenn). Cell line identity was independently authenticated by PCR.

Drugs

Drug stocks were prepared in DMSO or H_2O and diluted fresh in cell culture media for treatments. NITD-982[43] and N-phosphonacetyl-L-aspartate (PALA)[44] were synthesized as previously described.

In vivo mouse studies

All animal studies were approved by the UCLA Animal Research Committee (ARC). 4-6 week-old male NCG mice obtained from Charles River Laboratories (CRL 572), were injected subcutaneously in the flank with $2x10^6$ CCRF-CEM cells suspended in 100 μL 1:1 in PBS:matrigel. 4-6 week-old male C57BL/6 mice, obtained from UCLA Radiation Oncology, were injected subcutaneously on bilateral flanks with $0.3x10^6$ KP4662 cells suspended in 100 μL PBS. 14 days following inoculation treatment was initiated. JNK-IN-8 was suspended in 2% ethanol and 5% Tween-80 in PBS and administered by intraperitoneal (i.p.) injection at 50 mg/kg.

Method Details

Protein kinase inhibitor phenotypic screen

A library of 430 protein kinase inhibitors was arrayed in polypropylene 384-well plates at 200x concentrations covering a 7-point concentration range (corresponding to 1x concentrations: 5 μM, 1.65 μM, 550 nM, 185 nM, 61.5 nM, 20.6 nM, 6.85 nM). 25 μl per well of condition-specific growth media (DNP + NSP: media + 10 μM rU; DNP: media alone; NSP: media +10 μM rU + 1 μM NITD-982) was plated in opaque-white 384-well plates using a BioTek multidrop liquid handler. Protein kinase inhibitors were added by 250 nL pin-tool transfer (BioMek FX, Beckman-Coulter) and inhibitor/media mixtures were incubated at room temperature for 30 m. 25 μL of a 40,000 cells/mL MIAPACA2 suspension (for 1000 cells / well) was subsequently added to each well. After 72 h, 50 μL of Cell Titer Glo reagent diluted 1:4 in deionized H_2O was added to each well and luminescence was measured using a Wallac plate reader (Perkin Elmer). Each condition was assayed in duplicate (n=2) and % proliferation values were calculated by normalizing experimental wells to plate negative controls and averaging replicate values. Composite pathway selectivity synergy scores for each test compound were defined as the sum of the excess over additivity (% proliferation inhibition observed - % proliferation inhibition expected) between individual protein kinase inhibitor concentrations across the 7-point concentration range. Z factor scores for individual assay plates were calculated using eight positive and eight negative control wells on each plate as previously described.[16] All plates gave a Z factor > 0.5 (**Figure S2.3C**).

Cell Titer Glo viability analysis

Cells were plated at $1x10^3$ cells / well at 50 μl / well in white opaque 384-well plates and treated as described. Following incubation 50 μl of Cell Titer. Glo reagent (Diluted 1:5 in deionized H_2O) was added to each well, plates incubated at room temperature for 5 min and luminescence was measured using a BioTek microplate luminescence reader. Proliferation rate normalized growth inhibition was calculated using the previously described GR metric.[13]

Trypan blue exclusion cell viability

Trypan blue exclusion cell viability analysis was performed using a ViCell analyzer following 72 hr of treatment. Trypan blue-negative population counts are reported.

Microplate immunofluorescence microscopy cell scoring

MIAPACA2 cells were plated at 1000 cells/well in black-walled clear-bottom 384 well plates in 50 μL of media and treated as indicated with n=4 replicate wells per condition. After 72 hr of drug exposure 50 μL of 10 μg/mL Hoechst 33342 dye diluted in culture media was added to microplate wells. Following a 30 min incubation at 37C images were acquired using a ImageXpress Micro Confocal High-Content Imaging System at 10x magnification and 1 image/ well. Analysis was performed using the *Cell Scoring Application Module* in the MetaXpress analysis software. Nuclei counts for treatment groups were normalized to control wells.

Mass spectrometry

For analysis of stable isotope-labeled metabolite incorporation into newly replicated DNA, cells were cultured in glucose-free DMEM (for MIAPACA2 cells) or RPMI (for JURKAT cells)

media supplemented with 10% dialyzed FBS, 4 mM glutamine, 1 g/L [$^{13}C_6$]glucose, 10 μM [$^{13}C_9$; $^{15}N_2$]rU and treated as indicated.

Genomic DNA was extracted using the Quick-gDNA MiniPrep kit and hydrolyzed to nucleosides using the DNA Degradase Plus kit, following manufacturer-supplied instructions. In the final step of DNA extraction, 50 µL of water was used to elute the DNA into 1.5 mL microcentrifuge tubes. A nuclease solution (5 µL; 10X buffer/DNA Degradase PlusTM/water, 2.5/1/1.5, v/v/v) was added to 20 µL of the eluted genomic DNA in an HPLC injector vial. The samples were incubated overnight at 37 ºC.

Hydrolyzed DNA was diluted 1/1 with solvent A (water/acetonitrile/formic acid, 95/5/0.1, v/v) and analyzed using a modified version of a previously reported method[2,45] in which aliquots of the solution (15 μL) were injected onto a porous graphitic carbon column (Thermo Hypercarb, 100 x 2.1 mm, 5 micron particle size) equilibrated in solvent A and eluted (300 μL/min) with an increasing concentration of solvent B (acetonitrile/water/formic acid, 90/10/0.1). The HPLC timetable, in terms of min/%B, is the following: 0/0, 5/0, 12/20, 15/30, 17/50, 19/50, 20/0, 24/0. The effluent from the column was directed to Agilent Jet Stream connected Agilent 6460 QQQ operating in the positive ion MRM mode. After verification of retention times using authentic standards, the peak areas of the protonated nucleoside/protonated base fragment ion transitions for each of the nucleosides were recorded with instrument manufacturer-supplied software.

^{3}H-labeled metabolite uptake assays

Radioactive probe uptake assays were conducted as previously described.[46] Briefly, cells were pretreated with JNK-IN-8 or DPA for 2 hr before incubation with 18.5 kBq of ^{3}H-labeled probe

for 2 h. For purine uptake assays, cells were cultured in the presence of 10 μM dCF (for ^{3}H-dA) or 1 μM BCX-1777 (for ^{3}H-dG) to prevent nucleoside catabolism. Following incubation, cells were washed with PBS and lysed. Cell lysate radioactivity was measured using a beta-counter (Perkin-Elmer).

Flow cytometry

All flow cytometry data were acquired on five-laser BD LSRII, and analyzed using FlowJo software.

AnnexinV/PI: Treated PDAC cells were washed with PBS and incubated with AnnexinV and propidium iodide diluted in 1x Annexin binding buffer. 20,000 events were collected per sample.

Propidium iodide cell cycle analysis: Treated PDAC cells were washed with PBS and suspended in propidium iodide cell cycle staining solution (100 μg/ml propidium iodide; 20 μg/ml Ribonuclease A). 10,000 events were collected per sample.

pH2A.X$_{S139}$ flow cytometry: Treated cells were collected by trypsinization, incubated with Cytofix/Cytoperm reagent for 15 min at 4C, washed with PBS and incubated in 100 μL PermWash buffer for 15 min at 4C. Cells were washed with 1 mL Perm/Wash buffer, resuspended in 50 μL of staining solution (1:800 dilution of FITC-conjugated pH2AX$_{S139}$ antibody diluted in Perm/Wash buffer) and incubated for 20 min at 25C protected from light. Stained cells were washed and incubated in 500 μL of DAPI staining solution (1 μg/mL DAPI in PBS) before acquisition.

Gene cloning, protein expression, and purification of DHODH in E.coli cells

Primers were ordered to add NdeI (AGAGAACAGATTGGTGGTCATATGATGGCCACGGGAGATGAG) upstream of residue 29 (after the mitochondrial membrane associated loop) and BamHI (TCGGGCTTTGTTAGCAGCCGGATCCTTACCTCCGATGATCTGCTCC) after the stop codon to insert into N-terminal His-Sumo pET 14b vector. This clone, His-Sumo-DHODH 29-395 (subsequently referred to as DHODH) was successfully inserted into the vector in XL1-blue cells for vector propagation.

The vector was transformed into C41(DE3) cells for productions. Cells were grown at 37 °C in 2xYT medium supplemented with 100 μg/mL ampicillin (Amp), treated with 0.1 mM isopropyl β-D-1-thiogalactopyranoside (IPTG) at an OD600 nm of 0.6-0.8, and then cultured for an additional 18 hr at 18 °C. Cells were harvested by centrifugation, washed with 200 mM NaCl and 25 mM Tris pH 7.5, and pelleted at 5000 rpm for 20 min before storage at -20°C. 6.7g/L of cell pellet was obtained.

DHODH was purified according to known purification conditions.[28] The cell pellet was resuspended in lysis buffer (50 mM Tris pH 7.5; 600 mM NaCl; 0.33% w/v Thesit; 10% Glycerol; 1 mM PMSF) and lysed by sonication on ice. Lysed cells were centrifuged at 58,500 RCF for 45 min at 4°C, and the supernatant was filtered through a 0.45 μM filter and loaded onto a 5-mL His-Trap column pre-equilibrated with buffer A (50 mM Tris pH 7.4; 600 mM NaCl; 0.05% w/v Thesit; 10% Glycerol). The column was washed with buffer A for 70 mL, buffer A with 25 mM imidazole for 50 mL, and buffer A with 50 mM imidazole for 50 mL. The protein was eluted with buffer A with 250 mM imidazole. The eluted fraction was diluted 1:1 with Buffer A. Sumo protease was added and the protein was dialyzed overnight at 4°C against 1L of

Buffer A. The dialyzed protein was loaded back onto the His-Trap column equilibrated with buffer A. The cut-DHODH was eluted with buffer A with 50 mM imidazole. The purified protein was concentrated to 5 mL and injected onto S-200 gel filtration column (GE Healthcare) equilibrated with: 50 mM HEPES pH 7.7, 400 mM NaCl, 10% Glycerol, 1mM EDTA, 0.05 % w/ v Thesit. Eluted fractions consistent with monomer size were collected, concentrated, flash frozen, and stored at -80°C.

Recombinant DHODH enzyme assay

Evaluation of DHODH inhibition was performed as previously described.[28] The standard assay mixture contained 50 μM decyclo-ubiquinone, 100 μM dihydroorotate, and 60 μM 2,6-dichloroindophenol (DCIP). The amount of DHODH was 337.4 ng/mL. Measurements were conducted in 50 mM TrisHCl, 150 mM KCl, 0.1% Triton X-100, pH 8.0, at 30 °C in a final volume of 1 mL. The components were mixed, and the reaction was started by adding dihydroorotate. The reaction was followed spectrophotometrically by measuring the decrease in absorption at 600 nm for 2.5 min at 30 second intervals. The assay was linear in time and enzyme concentration. Inhibitory studies were conducted in a standard assay with additional variable amounts of inhibitor.

Crystallization of DHODH with OSU-03012 and TAK-632 compounds

For co-crystallizaion of DHODH and OSU-03012, crystals were obtained using the same conditions reported in previously published DHODH structures[28,47–60], namely 1.6 – 2.6 M ammonium sulfate and 5-30% glycerol in the well in pH 4.5, with 20 mg/mL DHODH with 2 mM dihydroorotate (DHO), 20.8 mM dodecyldimethyl-N-amineoxide (DDAO), and 400 μM inhibitor. Protein was mixed 1:1 with mother liquor and hanging drops were used at room

temperature. Crystals appeared after 48 hr and reached maximal size within one week. Molecular replacement used 4OQV as the starting model.[61] Interestingly, DHODH-TAK-632 crystals grown in similar conditions to those used for the DHODH-OSU-03012 complex did not show TAK-632 density. As a result, novel DHODH crystallization conditions were identified using commercial screens. For co-crystallization of DHODH with TAK-632, crystals were obtained in conditions of 1.4-1.6 M sodium phosphate, pH 8.2. Protein solution (20 mg/mL DHODH with 2 mM DHO, 20.8 mM DDAO, and 400 μM inhibitor) was mixed 1:1 with mother liquor and hanging drops were used at room temperature. Crystals appeared after 48 hr and reached maximal size within one week. The lack of density of the TAK-632 structure in the initial crystallography condition is most likely due to the difference in pH between the conditions, pH 4.5 and pH 8.2 for the OSU-03012 and the TAK-632 structure, respectively. There are multiple hydrogen bonds and potentially labile hydrogens on the TAK-632 structure that at low pH could be protonated and charged, potentially preventing their insertion into the hydrophobic tunnel. Ligplot+ was used to determine hydrophilic and hydrophobic interactions between inhibitors and DHODH molecules.[62,63]

Immunoblot analysis

PBS-washed cell pellets were resuspended in cold RIPA buffer supplemented with protease and phosphatase inhibitors. Protein lysates were normalized using BCA assay, diluted using RIPA and 4x laemmli loading dye, resolved on 4-12% Bis-Tris gels and electro-transferred to nitrocellulose membranes. After blocking with 5% nonfat milk in TBS + 0.1% Tween-20 (TBS-T), membranes were incubated overnight in primary antibodies diluted (per manufacturers instructions) in 5% BSA in TBS-T. Membranes were washed with TBST-T and incubated with

HRP-linked secondary antibodies prepared at a 1:2500 dilution in 5% nonfat dry milk / TBS-T. HRP was activated by incubating membranes with a mixture of SuperSignal Pico and SuperSignal Femto ECL reagents (100:1 ratio). Exposure of autoradiography film was used for detection.

CETSA

MIAPACA2 cells were cultured in 10 cm plates, washed with PBS, and harvested by cell scraping following addition of 4 mL of lysis buffer (100 mM ammonium sulfate, 400 mM NaCl, 10% glycerol, 0.5% DDM and 1x protease inhibitor cocktail). The cell lysate was collected in a 15 mL conical tube, incubated on ice for 20 m, centrifuged at 5,000xg for 20 min at 4C and protein content of the supernatant was measured. 30 μL of protein lysate was aliquoted into 1.5 mL Eppendorf tubes and treated with either DMSO, JNK-IN-8 or dipyridamole for 30 min on ice. Lysates were subsequently heated at the indicated temperatures using an Eppendorf Thermomixer for 6 m, cooled to room temperature for 3 min and transferred to ice. Heated lysates were centrifuged at 12,000xg for 40 min to pellet the insoluble protein fraction. Supernatants were processed for immunoblot analysis.

Statistical analyses

Data are presented as mean ± SD with number of biological replicates indicated. Comparisons of two groups were calculated using indicated unpaired two-tailed Student's t-test and P values less than 0.05 were considered significant. Comparisons of more than two groups were calculated using one-way ANOVA followed by Bonferroni's multiple comparison tests, and P values less than 0.05/m, where m is the total number of possible comparisons, were considered significant.

2.8 Supplementary Figures

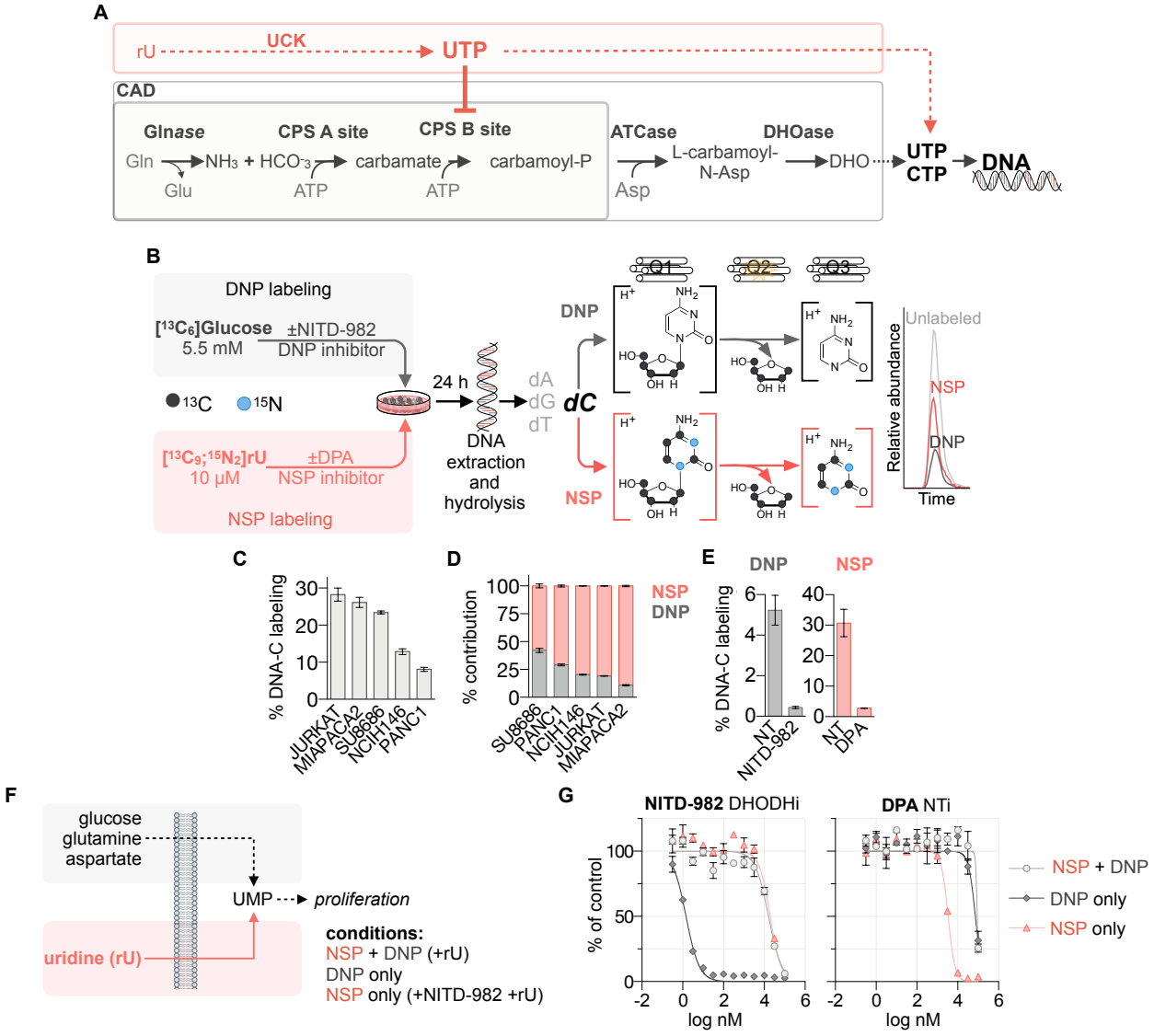

Figure S2.1 | Validation of UMP as a critical, convergent metabolic node in cancer cells. Related to Figure 2.1. (**A**) Schematic of CAD regulation by NSP produced UTP. (**B**) Schematic of the LC-MS/MS methodology used to determine the fractional contribution of UMP-DNP or -NSP specific stable isotope-labeled metabolite tracers to deoxycytidine (dC) in DNA (DNA-C). (**C**) Total % DNA-C labeling ([$^{13}C_6$]glucose + [$^{13}C_9$; $^{15}N_2$]uridine (rU) contribution) across a panel of cancer cell lines cultured for 24 hr determined by LC-MS/MS. (**D**) Relative contribution

of DNP and NSP pathways to DNA biosynthesis as determined by LC-MS/MS following 24 hr treatment (n=3). % contribution values are normalized to total % labeling in **E**. (**E**) LC-MS/MS analysis DNP([$^{13}C_6$]glucose) and NSP([$^{13}C_9$; $^{15}N_2$]rU) contribution to DNA-C in JURKAT cells cultured for 24 hr in media containing 5.5 mM [$^{13}C_6$]glucose and 10 μM [$^{13}C_9$; $^{15}N_2$]rU treated ±1 μM NITD-982 or ±1 μM dipyridamole (DPA; mean±SD; n=3). (**F**) UMP can be produced by a *de novo* pathway (DNP) from glucose, glutamine, bicarbonate and aspartate or from extracellular rU by a nucleoside transporter and kinase-dependent salvage pathway (NSP). (**G**) Dose response curves of DHODH inhibitor NITD-982 and nucleoside transport inhibitor (NTi) dipyridamole (DPA) in JURKAT cells cultured in NSP+DNP (media +10 μM rU), NSP only (media +10 μM rU +1 μM NITD-982), or DNP only (media alone) for 72 hr as determined by Cell Titer Glo (mean±SD; n=4).

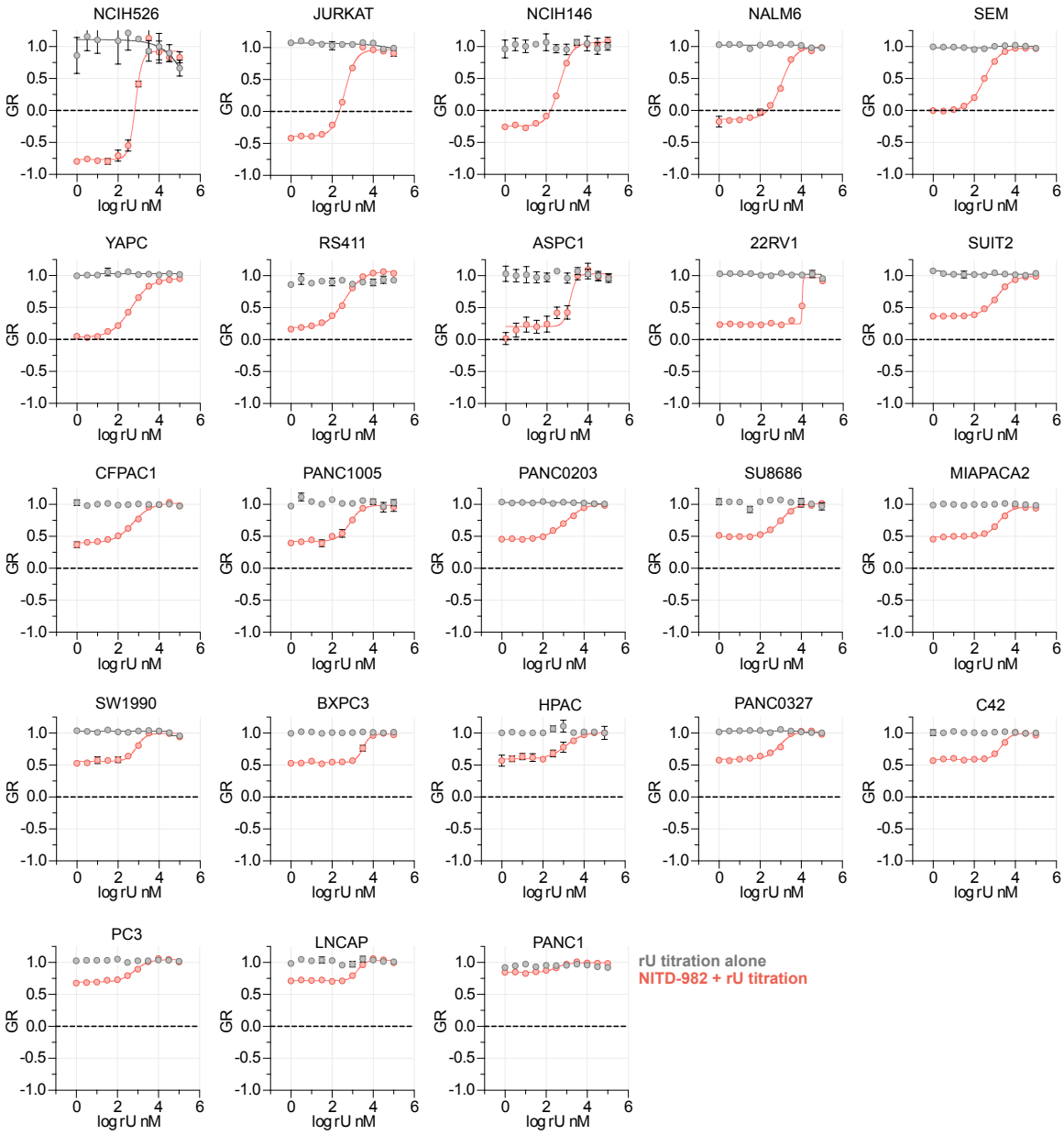

Figure S2.2 | UMP-DNP and NSP are interchangeable in sustaining proliferation across a panel of cancer cell lines. Related to Figure 2.1. Uridine titration in cancer cell lines cultured ±1 μM NITD-982 (mean±SD; n=4). Relative proliferation rate (GR) was calculated by normalizing % proliferation values at 72 hr to cell line proliferation rate. Proliferation rates were calculated utilizing CTG measurements at the time of treatment and vehicle-treated controls at 72 hr.

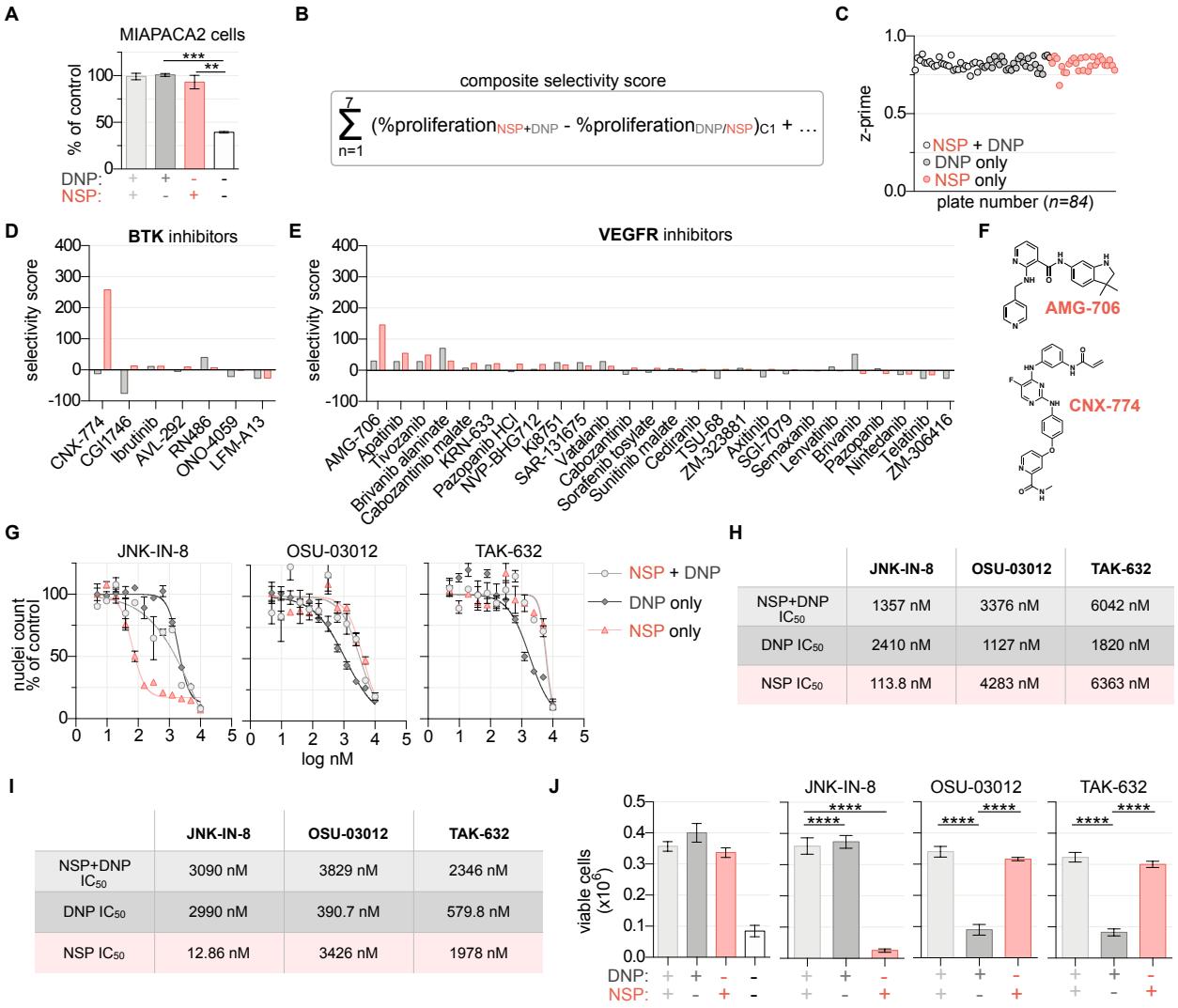

	JNK-IN-8	OSU-03012	TAK-632
NSP+DNP IC_{50}	1357 nM	3376 nM	6042 nM
DNP IC_{50}	2410 nM	1127 nM	1820 nM
NSP IC_{50}	113.8 nM	4283 nM	6363 nM

	JNK-IN-8	OSU-03012	TAK-632
NSP+DNP IC_{50}	3090 nM	3829 nM	2346 nM
DNP IC_{50}	2990 nM	390.7 nM	579.8 nM
NSP IC_{50}	12.86 nM	3426 nM	1978 nM

Figure S2.3 | Evaluation of UMP-NSP and -DNP inhibitor potency and selectivity. Related to Figure 2.1. (**A**) Cell Titer Glo analysis of MIAPACA2 cells cultured in NSP+DNP (media +10 μM rU), DNP (media alone), NSP (media +10 μM rU +1 μM NITD-982) or starvation conditions (media + 1 μM NITD-982) for 72 hr (mean±SD; n=4; one-way ANOVA corrected for multiple comparisons by Bonferroni adjustment, ** $P < 0.01$; *** $P < 0.001$). (**B**) Methodology applied to determine UMP-DNP and -NSP selectivity scores (screen performed at n=2). (**C**) Z'-scores calculated for individual assay plates from experiment in **Figure 2.1**. (**D**) Selectivity scores for BTK inhibitors included in the screen. (**E**) Selectivity scores for VEGFR inhibitors included in the screen. (**F**) Structures of hit compounds. (**G**) Immuno-fluorescence microscopy

nuclei counts of MIAPACA2 cells stained with Hoechst 33342 cultured in NSP+DNP (media +10 μM rU), DNP only (media alone) or NSP only (media +10 μM rU +1 μM NITD-982) conditions for 72 hr (mean±SD; n=4). (**H**) Calculation of IC_{50} values from experiment in **G**. (**I**) Calculation of JNK-IN-8, OSU-03012 and TAK-632 IC_{50} in JURKAT cells treated for 72 hr determined using Cell Titer Glo. (**J**) JURKAT cell counts using trypan-blue exclusion following treatment ±100 nM JNK-IN-8 ±1 μM OSU-03012 ±1 μM TAK-632 for 72 hr (mean±SD; n=4; one-way ANOVA corrected for multiple comparisons by Bonferroni adjustment,**** $P < 0.0001$).

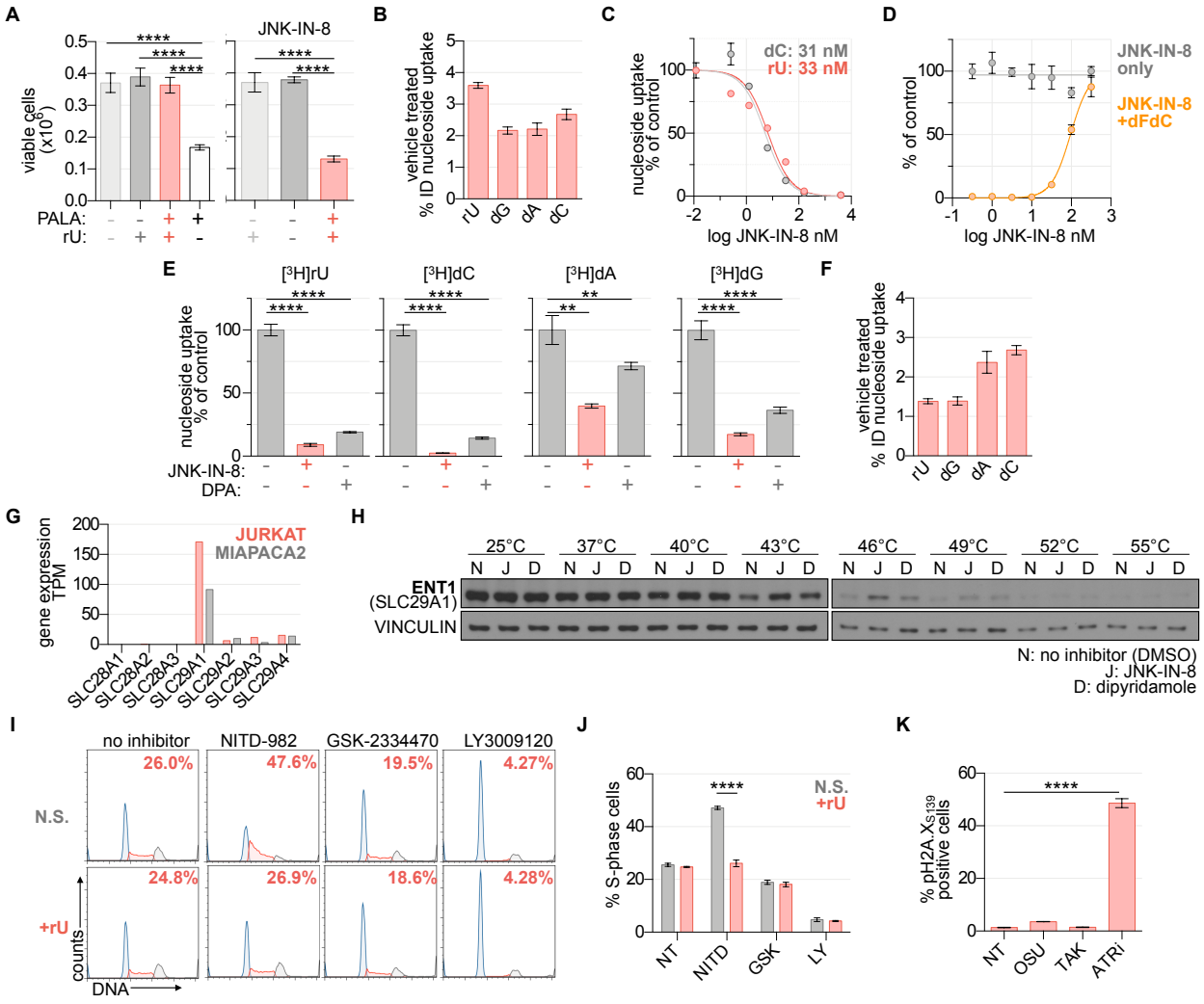

Figure S2.4 | Characterization of JNK-IN-8, OSU-03012 and TAK-632. Related to Figures 2.2 and 2.3. (**A**) JURKAT cell counts using trypan-blue exclusion following treatment ±200 μM PALA ±10 μM rU ±100 nM JNK-IN-8 for 72 hr (mean±SD; n=3; one-way ANOVA corrected for multiple comparisons by Bonferroni adjustment, **** P<0.0001). (**B**) Uptake of [^{3}H]labeled nucleosides in vehicle control condition from experiment in **Figure 2.2B**. Values represent % injected dose (%ID; n=3; 18.5 kBq). (**C**) Uptake of [^{3}H]rU or [^{3}H]dC in CCRF-CEM cells following 2 hr incubation ± JNK-IN-8 (mean±SD; n=2; 18.5 kBq). IC_{50} values are indicated. (**D**) Cell Titer Glo analysis of JURKAT cells treated ±10 nM dFdC ± JNK-IN-8 for 72 hr (mean±SD; n=4). Insert indicates JNK-IN-8 EC_{50} value. (**E**) Uptake of [^{3}H]rU, [^{3}H]dC, [^{3}H]dA (+10 μM

dCF), [^{3}H]dG (+1 μM BCX-1777) in KP4662 cells following 2 hr incubation ±1 μM JNK-IN-8 or 1 μM dipyridamole (DPA; 18.5 kBq; mean±SD; n=3; one-way ANOVA corrected for multiple comparisons by Bonferroni adjustment; ns: not significant; ** P<0.01; *** P<0.001; **** P<0.0001). (**F**) Uptake of [^{3}H]-labeled nucleosides in vehicle control condition from experiment in **E**. Values are expressed as % injected dose (%ID; n=3; 18.5 kBq). (**G**) Summary of nucleoside transporter expression (RNA-seq; data obtained from *oasis-genomics.org*). (**H**) CETSA for ENT1 (SLC29A1) engagement in MIAPACA2 protein lysates. Lysates were incubated +10 μM JNK-IN-8 or +10 μM DPA for 2 h, subsequently heat treated at the indicated temperatures and analyzed by immunoblot analysis. (**I**) Propidium iodide cell cycle analysis of MIAPACA2 PDAC cells treated ±1 μM NITD-982 (NITD) ±5 μM GSK-2334470 (GSK) or ±10 μM LY3009120 (LY) supplemented ±10 μM rU (N.S.: no supplement). Insert indicates % S-phase cells. (**J**) Summary of fold change in S-phase cells from **I** (mean±SD; n=2; one-way ANOVA corrected for multiple comparisons by Bonferroni adjustment, ns: not significant; **** P<0.0001). (**K**) pH2A.X$_{S139}$ flow cytometry analysis of MIAPACA2 cells treated ±5 μM OSU-03012 ±5 μM TAK-632 ±500 nM VE-822 (ATRi) for 48 hr (mean±SD; n=2; one-way ANOVA corrected for multiple comparisons by Bonferroni adjustment, ns: not significant; **** P<0.0001).

Table S2.1 | Crystallographic data collection and refinement statistics. Related to Figure 2.4.

Structure	DHODH + OSU-03012	DHODH + TAK-632
PDB codes	6OC0	6OC1
Data collection statistics		
X-ray source and detector	LS-CAT 21-ID-D Dectris Eiger x 9M	LS-CAT 21-ID-G MARCCD 300
Wavelength (Å)	0.99987	0.97872
Temperature (K)	100	100
Resolution[a] (Å)	1.40 (1.48-1.40)	2.7 (2.85-2.7)
Number of Reflections		
Observed	1,090,019 (113,565)	306,440 (48,502)
Unique	114,363 (17,418)	13,751 (2,169)
Completeness (%)	99.0 (94.2)	99.9 (99.8)
R_{meas} (%)	7.0 (54.5)	17.0 (183.3)
$CC_{1/2}$ (%)	99.9 (87.8)	99.9 (71.1)
Average I/σ(I)	19.2 (2.8)	21.6 (2.1)
Space group	P 3_2 2 1	P 2_1 3
Unit cell: a, b, c (Å)	90.01, 90.01, 123.07	113.67, 113.67, 113.67
Unit cell: α, β, γ (°)	90, 90, 120	90, 90, 90
Wilson B-factors (Å^2)	13.9	66.4
Refinement statistics		
Refinement program	REFMAC5	REFMAC5
R_{work} (%)	15.7	23.4
R_{free} (%)	19.1	29.1
Resolution range (Å)	48.55-1.40	46.45-2.70
Protein molecules per a.u.	1	1
Number of atoms:		
Protein	2845	2769
Water molecules	232	36
ORO + FMN	42	42
Inhibitor	34	39
R.m.s. deviation from ideal:		
Bond length (Å)	0.009	0.0021
Bond angles (°)	1.7114	1.264
Average B-factors (Å^2)		
Protein	23.9	73.0
Water molecules	32.6	44.7
ORO + FMN	12.2	56.6
Inhibitor	29.3	73.0
Ramachandran plot statistics (%)		
Most favored regions	97	86
Additionally allowed regions	3	14
Outlier regions	0	1

[a]High resolution shell in parenthesis; r.m.s., root-mean-square; a.u., asymmetric unit.

2.9 References

1. Xu, S.; Catapang, A.; Doh, H. M.; Bayley, N. A.; Lee, J. T.; Braas, D.; Graeber, T. G.; Herschman, H. R. Hexokinase 2 is targetable for HK1 negative, HK2 positive tumors from a wide variety of tissues of origin. *J. Nucl. Med.* **2019**, *2*, 212–217
2. Le, T. M.; Poddar, S.; Capri, J. R.; Abt, E. R.; Kim, W.; Wei, L.; Uong, N. T.; Cheng, C. M.; Braas, D.; Nikanjam, M.; Rix, P.; Merkurjev, D.; Zaretsky, J.; Kornblum, H. I.; Ribas, A.; Herschman, H. R.; Whitelegge, J.; Faull, K. F.; Donahue, T. R.; Czernin, J.; Radu, C. G. ATR inhibition facilitates targeting of leukemia dependence on convergent nucleotide biosynthetic pathways. *Nat. Commun.* **2017**, *8*, 241.
3. York, A.; Williams, K.; Argus, J.; Zhou, Q.; Brar, G.; Vergnes, L.; Gray, E.; Zhen, A.; Wu, N.; Yamada, D.; Cunningham, C.; Tarling, E.; Wilks, M.; Casero, D.; Gray, D.; Yu, A.; Wang, E.; Brooks, D.; Sun, R.; Kitchen, S.; Wu, T.-T.; Reue, K.; Stetson, D.; Bensinger, S. Limiting Cholesterol Biosynthetic Flux Spontaneously Engages Type I IFN Signaling. *Cell* **2015**, *163*, 1716-1729.
4. Garcia-Bermudez, J.; Baudrier, L.; La, K.; Zhu, X. G.; Fidelin, J.; Sviderskiy, V. O.; Papagiannakopoulos, T.; Molina, H.; Snuderl, M.; Lewis, C. A.; Possemato, R. L.; Birsoy, K. Aspartate is a limiting metabolite for cancer cell proliferation under hypoxia and in tumours. *Nat. Cell. Biol.* **2018**, *20*, 775-781.
5. Okesli, A.; Khosla, C.; Bassik, M. C. Human pyrimidine nucleotide biosynthesis as a target for antiviral chemotherapy. *Curr. Opin. Biotechnol.* **2017**, *48*, 127-134.
6. Van Rompay, A. R.; Ameli Norda, K. L.; Johansson, M.; Karlsson, A. Phosphorylation of Uridine and Cytidine Nucleoside Analogs by Two Human Uridine-Cytidine Kinases. *Mol. Pharmacol.* **2001**, *59*, 1181-1186.

7. Madak, J. T.; Bankhead, A.; Cuthbertson, C. R.; Showalter, H. D.; Neamati, N. Revisiting the role of dihydroorotate dehydrogenase as a therapeutic target for cancer. *Pharmacol. Ther.* **2019**, *195*, 111-131.

8. Sykes, D. B.; Kfoury, Y. S.; Mercier, F. E.; Wawer, M. J.; Law, J. M.; Haynes, M. K.; Lewis, T. A.; Schajnovitz, A.; Jain, E.; Lee, D.; Meyer, H.; Pierce, K. A.; Tolliday, N. J.; Waller, A.; Ferrara, S. J.; Eheim, A. L.; Stoeckigt, D.; Maxcy, K. L.; Cobert, J. M.; Bachand, J.; Szekely, B. A.; Mukherjee, S.; Sklar, L. A.; Kotz, J. D.; Clish, C. B.; Sadreyev, R. I.; Clemons, P. A.; Janzer, A.; Schreiber, S. L.; Scadden, D. T. Inhibition of Dihydroorotate Dehydrogenase Overcomes Differentiation Blockade in Acute Myeloid Leukemia. *Cell* **2016**, *167*, 171-186.

9. Santana-Codina, N.; Roeth, A. A.; Zhang, Y.; Yang, A.; Mashadova, O.; Asara, J. M.; Wang, X.; Bronson, R. T.; Lyssiotis, C. A.; Ying, H.; Kimmelman, A. C. Oncogenic KRAS supports pancreatic cancer through regulation of nucleotide synthesis. *Nat. Commun.* **2018**, *9*, 4945.

10. Lolli, M. L.; Sainas, S.; Pippione, A. C.; Giorgis, M.; Boschi, D.; Dosio, F. Use of human Dihydroorotate Dehydrogenase (hDHODH) Inhibitors in Autoimmune Diseases and New Perspectives in Cancer Therapy. *Recent Pat. Anticancer Drug Discov.* **2018**, *13*, 86-105.

11. Wang, Q. Y.; Bushell, S.; Qing, M.; Xu, H. Y.; Bonavia, A.; Nunes, S.; Zhou, J.; Poh, M. K.; Florez de Sessions, P.; Niyomrattanakit, P.; Dong, H.; Hoffmaster, K.; Goh, A.; Nilar, S.; Schul, W.; Jones, S.; Kramer, L.; Compton, T.; Shi, P. Y. Inhibition of dengue virus through suppression of host pyrimidine biosynthesis. *J. Virol.* **2011**, *85*, 6548-6556.

12. Evans, D. R.; Guy, H. I. Mammalian pyrimidine biosynthesis: fresh insights into an ancient pathway. *J. Biol. Chem.* **2004**, *279*, 33035-33038.

13. Hafner, M.; Niepel, M.; Chung, M.; Sorger, P. K. Growth rate inhibition metrics correct for confounders in measuring sensitivity to cancer drugs. *Nat. Methods* **2016**, *13*, 521-527.

14. Damaraju, V. L.; Weber, D.; Kuzma, M.; Cass, C. E.; Sawyer, M. B. Selective Inhibition of Human Equilibrative and Concentrative Nucleoside Transporters by BCR-ABL Kinase Inhibitors: Identification of Key hENT1 Amino Acid Residues for Interaction with BCR-ABL Kinase Inhibitors *J. Biol. Chem.* **2016**, *291*, 18809-18817.

15. Huang, M.; Wang, Y.; Collins, M.; Gu, J. J.; Mitchell, B. S.; Graves, L. M. Inhibition of Nucleoside Transport by p38 MAPK Inhibitors. *J. Biol. Chem.* **2002**, *277*, 28364-28367.

16. Zhang, J; Chung, T. D.; Oldenburg, K. R. A Simple Statistical Parameter for Use in Evaluation and Validation of High Throughput Screening Assays. *J. Biomol. Screen.* **1999**, *4*, 67-73.

17. Zhu, J.; Huang, J. W.; Tseng, P. H.; Yang, Y. T.; Fowble, J.; Shiau, C. W.; Shaw, Y. J.; Kulp, S. K.; Chen, C. S. From the cyclooxygenase-2 inhibitor celecoxib to a novel class of 3-phosphoinositide-dependent protein kinase-1 inhibitors. *Cancer Res.* **2004**, *64*, 4309-4318.

18. Okaniwa, M.; Hirose, M.; Arita, T.; Yabuki, M.; Nakamura, A.; Takagi, T.; Kawamoto, T.; Uchiyama, N.; Sumita, A.; Tsutsumi, S.; Tottori, T.; Inui, Y.; Sang, B. C.; Yano, J.; Aertgeerts, K.; Yoshida, S.; Ishikawa, T. Discovery of a selective kinase inhibitor (TAK-632) targeting pan-RAF inhibition: design, synthesis, and biological evaluation of C-7-substituted 1,3-benzothiazole derivatives. *J. Med. Chem.* **2013**, *56*, 6478-6494.

19. Fang, J.; Uchiumi, T.; Yagi, M.; Matsumoto, S.; Amamoto, R.; Takazaki, S.; Yamaza, H.; Nonaka, K.; Kang, D. Dihydro-orotate dehydrogenase is physically associated with the

respiratory complex and its loss leads to mitochondrial dysfunction. *Biosci. Rep.* **2013**, *33*, e00021.

20. Collins, K. D.; Stark, G. R. Aspartate Transcarbamylase: Interaction with the Transition State Analogue N-(phosphonoacetyl)-L-Aspartate. *J. Biol. Chem.* 6599 (1971).
21. Peters, G. J. Antipyrimidine effects of five different pyrimidine de novo synthesis inhibitors in three head and neck cancer cell lines. *Nucleos. Nucleot. Nucl.* **2018**, *6*, 329-339.
22. Mackey, J. R.; Mani, R. S.; Selner, M.; Mowles, D.; Young, J. D.; Belt, J. A.; Crawford, C. R.; Cass, C. E. Functional nucleoside transporters are required for gemcitabine influx and manifestation of toxicity in cancer cell lines. *Cancer Res.* **1998**, *58*, 4349-4357.
23. Byrne, K. T.; Leisenring, N. H.; Bajor, D. L.; Vonderheide, R. H. CSF-1R–Dependent Lethal Hepatotoxicity When Agonistic CD40 Antibody Is Given before but Not after Chemotherapy. *J.I.* **2016**, *197*, 179-187.
24. Young, J. D.; Yao, S. Y.; Baldwin, J. M.; Cass, C. E.; Baldwin, S. A. The human concentrative and equilibrative nucleoside transporter families, SLC28 and SLC29. *Mol. Aspects Med.* **2013**, *34*, 529-547.
25. Fernandez-Banet, J.; Esposito, A.; Coffin, S.; Horvath, I. S.; Estrella, H.; Schefzick, S.; Deng, S.; Wang, K.; AChing, K.; Ding, Y.; Roberts, P.; Rejto, P. A.; Kan, Z. OASIS: web-based platform for exploring cancer multi-omics data. *Nat. Methods* **2016**, *13*, 8-9.
26. Martinez Molina, D.; Nordlund, P. The Cellular Thermal Shift Assay: A Novel Biophysical Assay for In Situ Drug Target Engagement and Mechanistic Biomarker Studies. *Annu. Rev. Pharmacol. Toxicol.* **2016**, *56*, 141-161.

27. Bonomo, S.; Tosco, P.; Giorgis, M.; Lolli, M.; Fruttero, R. The role of fluorine in stabilizing the bioactive conformation of dihydroorotate dehydrogenase inhibitors. *J. Mol. Model.* **2013**, *19*, 1099-1107.

28. Baumgartner, R.; Walloschek, M.; Kralik, M.; Gotschlich, A.; Tasler, S.; Mies, J.; Leban, J. Dual binding mode of a novel series of DHODH inhibitors. *J. Med. Chem.* **2006**, *49*, 1239-1247.

29. Yuan, T. L.; Amzallag, A.; Bagni, R.; Yi, M.; Afghani, S.; Burgan, W.; Fer, N.; Strathern, L. A.; Powell, K.; Smith, B.; Waters, A. M.; Drubin, D.; Thomson, T.; Liao, R.; Greninger, P.; Stein, G. T.; Murchie, E.; Cortez, E.; Egan, R. K.; Procter, L.; Bess, M.; Cheng, K. T.; Lee, C.-S.; Lee, L. C.; Fellmann, C.; Stephens, R.; Luo, J.; Lowe, S. W.; Benes, C. H.; McCormick, F. Differential Effector Engagement by Oncogenic KRAS. *Cell Rep.* **2018**, *22*, 1889-1902.

30. Peng, S. B.; Henry, J. R.; Kaufman, M. D.; Lu, W. P.; Smith, B. D.; Vogeti, S.; Rutkoski, T. J.; Wise, S.; Chun, L.; Zhang, Y.; Van Horn, R. D.; Yin, T.; Zhang, X.; Yadav, V.; Chen, S. H.; Gong, X.; Ma, X.; Webster, Y.; Buchanan, S.; Mochalkin, I.; Huber, L.; Kays, L.; Donoho, G. P.; Walgren, J.; McCann, D.; Patel, P.; Conti, I.; Plowman, G. D.; Starling, J. J.; Flynn, D. L. Inhibition of RAF Isoforms and Active Dimers by LY3009120 Leads to Anti-tumor Activities in RAS or BRAF Mutant Cancers. *Cancer Cell* **2015**, *28*, 384-398.

31. Zeman, M. K.; Cimprich, K. A. Causes and consequences of replication stress. *Nat. Cell. Biol.* **2014**, *16*, 2-9.

32. Arroyo, J. D.; Jourdain, A. A.; Calvo, S. E.; Ballarano, C. A.; Doench, J. G.; Root, D. E.; Mootha, V. K. A Genome-wide CRISPR Death Screen Identifies Genes Essential for Oxidative Phosphorylation. *Cell Metab.* **2016**, *24*, 875-885..

33. Gohil, V. M.; Sheth, S. A.; Nilsson, R.; Wojtovich, A. P.; Lee, J. H.; Perocchi, F.; Chen, W.; Clish, C. B.; Ayata, C.; Brookes, P. S.; Mootha, V. K. Nutrient-sensitized screening for drugs that shift energy metabolism from mitochondrial respiration to glycolysis. *Nat. Biotechnol.* **2010**, *28*, 249-255.

34. a) Zhang, T.; Inesta-Vaquera, F.; Niepel, M.; Zhang, J.; Ficarro, S. B.; Machleidt, T.; Xie, T.; Marto, J. A.; Kim, N.; Sim, T.; Laughlin, J. D.; Park, H.; LoGrasso, P. V.; Patricelli, M.; Nomanbhoy, T. K.; Sorger, P. K.; Alessi, D. R.; Gray, N. S. Discovery of potent and selective covalent inhibitors of JNK. *Chem. Biol.* **2012**, *19*, 140-154.; b) Vardhana, S.A., Wolchok, J.D. The many faces of the anti-COVID immune response. *J. Exp. Med.* **2020**, *6*, e20200678.

35. Young, J. D.; Yao, S. Y.; Sun, L.; Cass, C. E.; Baldwin, S. A. Human equilibrative nucleoside transporter (ENT) family of nucleoside and nucleobase transporter proteins. *Xenobiotica* **2008**, *38*, 995-1021.

36. Wright, N. J.; Lee, S. Y. Structures of human ENT1 in complex with adenosine reuptake inhibitors. *Nat. Struct. Mol. Biol.* **2019**, *26*, 599-606.

37. Yao, S. Y. M.; Ng, A. M. L.; Cass, C. E.; Young, J. D. Role of cysteine 416 in N-ethylmaleimide sensitivity of human equilibrative nucleoside transporter 1 (hENT1). *Biochem. J.* **2018**, *475*, 3293-3309.

38. Radu, C. G.; Shu, C. J.; Nair-Gill, E.; Shelly, S. M.; Barrio, J. R.; Satyamurthy, N.; Phelps, M. E.; Witte, O. N. Molecular imaging of lymphoid organs and immune activation by positron emission tomography with a new [18F]-labeled 2'-deoxycytidine analog. *Nat. Med.* **2008**, *14*, 783-788.

39. Shields, A. F.; Grierson, J. R.; Dohmen, B. M.; Machulla, H. J.; Stayanoff, J. C.; Lawhorn-Crews, J. M.; Obradovich, J. E.; Muzik, O.; Mangner, T. J. Imaging proliferation in vivo with [F-18]FLT and positron emission tomography. *Nat. Med.* **1998**, *4*, 1334-1336.

40. Kim, W.; Le, T. M.; Wei, L.; Poddar, S.; Bazzy, J.; Wang, X.; Uong, N. T.; Abt, E. R.; Capri, J. R.; Austin, W. R.; Van Valkenburgh, J. S.; Steele, D.; Gipson, R. M.; Slavik, R.; Cabebe, A. E.; Taechariyakul, T.; Yaghoubi, S. S.; Lee, J. T.; Sadeghi, S.; Lavie, A.; Faull, K. F.; Witte, O. N.; Donahue, T. R.; Phelps, M. E.; Herschman, H. R.; Herrmann, K.; Czernin, J.; Radu, C. G. [18F]CFA as a clinically translatable probe for PET imaging of deoxycytidine kinase activity. *Proc. Natl. Acad. Sci. USA* **2016**, *113*, 4027-4032.

41. Paproski, R. J.; Wuest, M.; Jans, H. S.; Graham, K.; Gati, W. P.; McQuarrie, S.; McEwan, A.; Mercer, J.; Young, J. D.; Cass, C. E. Biodistribution and uptake of 3'-deoxy-3'-fluorothymidine in ENT1-knockout mice and in an ENT1-knockdown tumor model. *J. Nucl. Med.* **2010**, *51*, 1447-1455.

42. Yang, C. F.; Gopula, B.; Liang, J. J.; Li, J. K.; Chen, S. Y.; Lee, Y. L.; Chen, C. S.; Lin, Y. L. Novel AR-12 derivatives, P12-23 and P12-34, inhibit flavivirus replication by blocking host de novo pyrimidine biosynthesis. *Emerg. Microbes Infect.* **2018**, *7*, 187.

43. Bonavia, A., Franti, M., Pusateri Keaney, E., Kuhen, K., Seepersaud, M., Radetich, B., Shao, J., Honda, A., Dewhurst, J., Balabanis, K., Monroe, J., Wolff, K., Osborne, C., Lanieri, L., Hoffmaster, K., Amin, J., Markovits, J., Broome, M., Skuba, E., Cornella-Taracido, I., Joberty, G., Bouwmeester, T., Hamann, L., Tallarico, J. A., Tommasi, R., Compton, T., Bushell, S. M. Identification of broad-spectrum antiviral compounds and assessment of the druggability of their target for efficacy against respiratory syncytial virus (RSV). *Proc. Natl. Acad. Sci. USA* **2011**, *108*, 6739-6744.

44. Morris, A.; Cordi, A. A New, Efficient Two-Step Procedure for the Preparation of the Antineoplastic Agent Sparfosic Acid. *Syn. Comm.* **1997**, *27*, 1259-1266.

45. Nathanson, D. A.; Armijo, A. L.; Tom, M.; Li, Z.; Dimitrova, E.; Austin, W. R.; Nomme, J.; Campbell, D. O.; Ta, L.; Le, T. M.; Lee, J. T.; Darvish, R.; Gordin, A.; Wei, L.; Liao, H. I.; Wilks, M.; Martin, C.; Sadeghi, S.; Murphy, J. M.; Boulos, N.; Phelps, M. E.; Faull, K. F.; Herschman, H. R.; Jung, M. E.; Czernin, J.; Lavie, A.; Radu, C. G. Co-targeting of convergent nucleotide biosynthetic pathways for leukemia eradication. *J. Exp. Med.* **2014**, *211*, 473-486.

46. Campbell, D. O.; Yaghoubi, S. S.; Su, Y.; Lee, J. T.; Auerbach, M. S.; Herschman, H.; Satyamurthy, N.; Czernin, J.; Lavie, A.; Radu, C. G. Structure-guided Engineering of Human Thymidine Kinase 2 as a Positron Emission Tomography Reporter Gene for Enhanced Phosphorylation of Non-natural Thymidine Analog Reporter Probe. *J. Biol. Chem.* **2011**, *287*, 446-454.

47. Lewis, T. A.; Sykes, D. B.; Law, J. M.; Muñoz, B.; Rustiguel, J. K.; Nonato, M. C.; Scadden, D. T.; Schreiber, S. L. Development of ML390: A Human DHODH Inhibitor That Induces Differentiation in Acute Myeloid Leukemia. *ACS Med. Chem. Lett.* **2016**, *7*, 1112-1117.

48. Das, P.; Deng, X.; Zhang, L.; Roth, M. G.; Fontoura, B. M.; Phillips, M. A.; De Brabander, J. K. SAR Based Optimization of a 4-Quinoline Carboxylic Acid Analog with Potent Anti-Viral Activity. *ACS Med. Chem. Lett.* **2013**, *4*, 517-521.

49. Davies, M.; Heikkilä, T.; McConkey, G. A.; Fishwick, C. W.; Parsons, M. R.; Johnson, A. P. Structure-based design, synthesis, and characterization of inhibitors of human and

Plasmodium falciparum dihydroorotate dehydrogenases. *J. Med. Chem.* **2009**, *52*, 2683-2693.

50. Erra, M.; Moreno, I.; Sanahuja, J.; Andrés, M.; Reinoso, R. F.; Lozoya, E.; Pizcueta, P.; Godessart, N.; Castro-Palomino, J. C. Biaryl analogues of teriflunomide as potent DHODH inhibitors. *Bioorg. Med. Chem. Lett.* **2011**, *21*, 7268-7272.

51. Hurt, D. E.; Sutton, A. E.; Clardy, J. Brequinar derivatives and species-specific drug design for dihydroorotate dehydrogenase. *Bioorg. Med. Chem. Lett.* **2006**, *16*, 1610-1615.

52. Ladds, M. J. G. W.; van Leeuwen, I. M. M.; Drummond, C. J.; Chu, S.; Healy, A. R.; Popova, G.; Pastor Fernández, A.; Mollick, T.; Darekar, S.; Sedimbi, S. K.; Nekulova, M.; Sachweh, M. C. C.; Campbell, J.; Higgins, M.; Tuck, C.; Popa, M.; Safont, M. M.; Gelebart, P.; Fandalyuk, Z.; Thompson, A. M.; Svensson, R.; Gustavsson, A. L.; Johansson, L.; Färnegårdh, K.; Yngve, U.; Saleh, A.; Haraldsson, M.; D'Hollander, A. C. A.; Franco, M.; Zhao, Y.; Håkansson, M.; Walse, B.; Larsson, K.; Peat, E. M.; Pelechano, V.; Lunec, J.; Vojtesek, B.; Carmena, M.; Earnshaw, W. C.; McCarthy, A. R.; Westwood, N. J.; Arsenian-Henriksson, M.; Lane, D. P.; Bhatia, R.; McCormack, E.; Laín, S. A DHODH inhibitor increases p53 synthesis and enhances tumor cell killing by p53 degradation blockage. *Nat. Comm.* **2018**, *9*, 1107.

53. Liu, S.; Neidhardt, E. A.; Grossman, T. H.; Ocain, T.; Clardy, J. Structures of human dihydroorotate dehydrogenase in complex with antiproliferative agents. *Structure* **2000**, *8*, 25-33.

54. McLean, L. R.; Zhang, Y.; Degnen, W.; Peppard, J.; Cabel, D.; Zou, C.; Tsay, J. T.; Subramaniam, A.; Vaz, R. J.; Li, Y. Discovery of novel inhibitors for DHODH via virtual

screening and X-ray crystallographic structures. *Bioorg. Med. Chem. Lett.* **2010**, *20*, 1981-1984.

55. Sainas, S.; Pippione, A. C.; Lupino, E.; Giorgis, M.; Circosta, P.; Gaidano, V.; Goyal, P.; Bonanni, D.; Rolando, B.; Cignetti, A.; Ducime, A.; Andersson, M.; Järvå, M.; Friemann, R.; Piccinini, M.; Ramondetti, C.; Buccinnà, B.; Al-Karadaghi, S.; Boschi, D.; Saglio, G.; Lolli, M. L. Targeting Myeloid Differentiation Using Potent 2-Hydroxypyrazolo[1,5-a]pyridine Scaffold-Based Human Dihydroorotate Dehydrogenase Inhibitors. *J. Med. Chem.* **2018**, *61*, 6034-6055.

60. Walse, B.; Dufe, V. T.; Svensson, B.; Fritzson, I.; Dahlberg, L.; Khairoullina, A.; Wellmar, U.; Al-Karadaghi, S. The structures of human dihydroorotate dehydrogenase with and without inhibitor reveal conformational flexibility in the inhibitor and substrate binding sites. *Biochemistry* **2008**, *47*, 8929-8936.

61. Deng, X.; Kokkonda, S.; El Mazouni, F.; White, J.; Burrows, J. N.; Kaminsky, W.; Charman, S. A.; Matthews, D.; Rathod, P. K.; Phillips, M. A. Fluorine modulates species selectivity in the triazolopyrimidine class of Plasmodium falciparum dihydroorotate dehydrogenase inhibitors. *J. Med. Chem.* **2014**, *57*, 5381-5394.

62. Laskowski, R. A.; Swindells, M. B. LigPlot+: multiple ligand-protein interaction diagrams for drug discovery. *J. Chem. Inf. Model.* **2011**, *51*, 2778-2786.

63. Wallace, A. C.; Laskowski, R. A.; Thornton, J. M. LIGPLOT: a program to generate schematic diagrams of protein-ligand interactions. *Protein Eng.* **1995**, *8*, 127-134.